Saffer, D., McNeill, L., Byrne, T., Araki, E., Toczko, S., Eguchi, N., Takahashi, K., and the Expedition 319 Scientists
Proceedings of the Integrated Ocean Drilling Program, Volume 319

Site C0010[1]

Expedition 319 Scientists[2]

Chapter contents

Background and objectives

Integrated Ocean Drilling Program (IODP) Expedition 319 Site C0010 (proposed Site NT2-01J) is a riserless drilling site located 3.5 km along strike of previously drilled and cored IODP Site C0004 (Figs. **F1, F2**) and was planned to penetrate the megasplay fault at ~410 meters below seafloor (mbsf) and ~150 m into the footwall. A summary of Nankai Trough Seismogenic Zone Experiment (NanTroSEIZE) drilling around Site C0010 is shown in Figure **F1.** The operational and scientific objectives at this site were to

- Collect logging-while-drilling (LWD) and measurement-while-drilling (MWD) data to 560 mbsf to complement LWD and core data collected during IODP Expeditions 314 and 316 at Site C0004 (Kinoshita et al., 2008; Kimura et al., 2008) in order to
  - Characterize the lithology, physical properties, and structural geology of the shallow slope apron, thrust wedge, megasplay fault, and overridden slope apron and
  - Correlate observations between Sites C0004 and C0010 to assess along-strike variations in physical properties and fault zone architecture;
- Install casing to ~550 mbsf with screened joints (~20 m of screened interval) spanning the megasplay fault as defined from logging data in order to provide hydraulic communication between instruments inside casing and the fault zone in preparation for planned observatory installation in 2010, 2011, or beyond;
- Conduct a "dummy run" of the instrument package (including a strainmeter and broadband seismometer) to evaluate shock and acceleration caused by hole reentry and instrument emplacement, for future installation of a strainmeter and seismometer package at this site as part of a permanent observatory; and
- Suspend the hole with a temporary monitoring system (a "smart plug") affixed to a retrievable casing packer (bridge plug), in order to record pore pressure and temperature within the screened interval of the formation.

The temporary instrument package will provide continuous monitoring during the time between drilling of the site (this expedition) and permanent observatory installation. This planned per-

---

[1] Expedition 319 Scientists, 2010. Site C0010. *In* Saffer, D., McNeill, L., Byrne, T., Araki, E., Toczko, S., Eguchi, N., Takahashi, K., and the Expedition 319 Scientists, *Proc. IODP,* 319: Tokyo (Integrated Ocean Drilling Program Management International, Inc.). doi:10.2204/iodp.proc.319.104.2010

[2] **Expedition 319 Scientists' addresses.**

manent observatory will monitor seismicity, volumetric strain, tilt, pore pressure, and temperature (Fig. F3). Together with a second planned long-term observatory installation at Site C0009, it will constitute the initial phase of a distributed observatory network spanning the region above the aseismic–seismic transition on the plate boundary at depth.

Based on interpretation of three-dimensional (3-D) seismic reflection data and the results of drilling at Site C0004 during Expeditions 314 and 316 (Kinoshita et al., 2008; Kimura et al., 2008), the anticipated geology from the top of the section to the planned total depth (TD) was an ~200 m thick sequence of slope apron deposits composed of silty mudstone with some thin sand and ash layers overlying an ~210 m thick zone of fractured mudstone comprising a thrust wedge in the hanging wall of the megasplay fault (e.g., Moore et al., 2009). The fault juxtaposes the thrust wedge above with overridden slope apron sediments below, which consist of silty mudstone with numerous sand beds and some ash (Kimura et al., 2008; Moore et al., 2009). The character of the megasplay fault zone in seismic reflection images differs markedly between Sites C0004 and C0010. At Site C0004, there are two distinct reflectors at the base of the thrust wedge, and both coring and LWD data document the presence of two main fault zones separated by an ~50 m thick "fault-bounded package" (e.g., Kimura et al., 2008). In contrast, at Site C0010, the megasplay is imaged as a single sharp reflector in the seismic data, suggesting that the fault zone would be thinner and perhaps have a simpler architecture than at Site C0004.

Operations

Transit to Site C0010

After operations were completed at IODP Site C0009, the D/V *Chikyu* moved to Site C0010. While in transit, the drill pipe was set up and racked in preparation for running into the hole. The location was reached at 0100 h on 4 August 2009, and the remotely operated vehicle (ROV) engaged in a seabed survey.

Hole C0010A

The *Chikyu* moved to the new location after completing operations in Hole C0009A, and Schlumberger engineers and technicians prepared the Schlumberger LWD and MWD tools for assembly prior to drilling Hole C0010A (target depth = 560 mbsf, water depth = 2523.7 m) (Table T1). The bottom-hole assembly (BHA) included a 12¼ inch bit, RAB-8, TeleScope, stabilizer, crossover subs, 11 drilling collars, and a mechanical jar (Table T2). The mud cart and jet-in tools were prepared and hung below the *Chikyu* in the low-current area prior to drifting to the site. The ROV was again deployed for the jet-in, which occurred at 0745 h on 5 August. Jetting-in included placing a Mudmat and 20 inch casing to 41 m drilling depth below seafloor (DSF).

The BHA was made up of a 12¼ inch bit, with an 8¼ inch LWD geoVISION tool measuring natural gamma ray (NGR) and resistivity, and the MWD-PowerPulse measuring direction and inclination, torque, and weight on bit. After LWD and MWD drilling to 402 m DSF (Run 1), operations were suspended on 9 August to move the *Chikyu* to safety, out of the path of Typhoon "Etau," and wait on weather (WOW). Although the winds and wave predictions were not very severe (21–31 m/s winds and 5.9–9.5 m swells), the heave prediction was of greater concern. Heave had a detrimental influence on the LWD data quality, and the Co-Chief Scientists and Operations Superintendent (OSI) decided to ream and relog the hole from 2900 to 2970 m drilling depth below rig floor (DRF), in order to improve the data quality around the fault zone target and to better define locations for screened casing joint placement. After the storm passed, the *Chikyu* returned to Site C0010 to resume drilling operations to TD (Run 2), arriving at 0200 h on 12 August. Reaming operations began at 0300 h and included relogging the 2900–2970 m DRF section. TD (3107 m DRF, 555.00 m DSF) was reached at 1715 h on 12 August, when circulation and high-viscosity (Hi-Vis) mud was pumped into the hole. Operations continued with a wiper trip to the 20 inch casing shoe at 41 m DSF, and then running back to the bottom of the hole. Because the wiper trip exhibited tightness in one section of the hole below 2995 m DRF even after reaming, reaming continued from 2995 to 3107 m DRF. After spotting with kill mud, pulling out of the hole to 2584 m DRF and then washing to 2543 m DRF to clean the wellhead, pulling out of the hole continued to surface while recovering the ROV in preparation for moving the *Chikyu* to a low-current area. At 1700 h, the BHA was back on the drill floor.

The *Chikyu* moved upcurrent, and then 13 nmi northwest of Site C0010 to a low-current area to run the casing pipe, finishing preparations on 13 August. After examining the LWD data from logging Runs 1 and 2, the bottom depth of the screen casing joints was set at 2959 m DRF (407.59 m DSF) (Fig. F4). Casing was run into the water column, and the *Chikyu* started drifting to Hole C0010A on 14 August. At 1120 h on 15 August, the casing was run into Hole C0010A and reached 500 m DSF at ~1443 h. At 2130 h, pulling out of the hole began, and at 2230 h, the stinger was out of the hole. There was no signal from the cement dart to show that it had landed/seated properly, so a scraper run was planned. There was a break while the ROV umbilical was under repair, during which the 8½ inch drill collar was made up for a scraper run. The scraper run was cancelled after the cement dart was found when the BHA was disassembled. Instead, the hole was reentered for a sweep at 1210 h on 17 August, finishing at 1400 h, with the BHA reaching deck at 1621 h. After the sweep was completed, the dummy observatory run began. On 19 August, ocean-bottom seismometers used in conjunction with vertical seismic profile operations at Site C0009 were acoustically released and recovered by the supply ship, *Kaiko,* at 2020 h on 20 August.

Dummy run

The dummy run (see **"Observatory"**) began in a low-current area at 0830 h on 18 August. This included a shipboard test to ensure the instrument carrier could be run through the 9⅝ inch casing after it was discovered that the sensor carrier was warped. After confirming that it could pass though the casing unimpeded at 0900 h on 18 August, the entire array was made up beginning at 1215 h and run into the hole at 1500 h. During these operations, the smart plug (see **"Observatory"**) was tested in preparation for installation in Hole C0010A. There was considerable vortex-induced vibration (VIV) from the strong current (4.5 kt) during drifting in to location, and the carrier was held at 1650 meters below sea level (mbsl) for ROV inspection. At 1750 h on 19 August, the ROV was deployed, and at 2045 h, it reached the carrier. Visual inspection revealed that the strainmeter and tubing below were lost, as well as one of the two seismometers. The remaining seismometer and accelerometer remained attached, and at 2130 h, after meeting with the OSI, the Co-Chief Scientists decided to recover the carrier to the surface for further inspection. As the *Chikyu* moved north 9 nmi to a low-current area, the carrier was pulled up, reaching deck at 0400 h on 20 August. The carrier showed signs of polishing and cracking and required ~4 h for the ship's welder to repair. The second dummy run carrier included only the accelerometer and a dummy strainmeter with two tubing joints below the seismometer, and it was decided to stab the reentry cone 2–3 times with no attempt to pass the carrier into the hole. The carrier was returned to the water at 1500 h on 20 August and lowered below the Kuroshio Current as the *Chikyu* drifted back to Hole C0010A. At 0915 h on 21 August, the *Chikyu* returned to the site and jumped the ROV in preparation for stabbing the wellhead. At 0955 h, the carrier was ready for reentry into Hole C0010A, which began at 1010 h and was completed by 1025 h. Pulling out of the hole began at 1040 h, and the carrier reached the drill floor at 1630 h.

Smart plug

The smart plug was made up and welded to the crossover sub at 0525 h on 22 August and then run into the hole. Drifting to Site C0010 began, and at 1350 h (4 nmi from the site), the ROV was deployed. At 1709 h, the *Chikyu* was still 9.2 nmi from Hole C0010A, arriving at 0110 h on 23 August. There was another delay as the ROV umbilical needed work to fix a broken strand. The smart plug and packer were run into Hole C0010A at 0404 h, and the packer was set at 0850 h. The drill string was removed at 0930 h while the *Chikyu* moved again to a low-current area 3 nmi from Site C0010. Upon recovery, it was discovered that the bridge plug running tool had sheared off of the drill pipe in the water column at a 3½ inch tubing connection after the packer had been set. The corrosion cap was attached to the ROV carrier, in preparation for setting in at the wellhead. At 1800 h, the ROV was launched but experienced problems with the umbilical again at 2030 h. After troubleshooting was completed, the corrosion cap was finally set at 1015 h on 24 August. The ROV began recovery of the transponders, but again had trouble and was recovered on deck. It was decided to recover the remaining three transponders with the *Kaiko*, after acoustically releasing them from the seafloor. By 1200 h on 25 August, with all transponders recovered, the *Chikyu* began moving toward Site C0011 (proposed Site NT1-07).

Logging and data quality

Logging results

Logging data collected during MWD and with the LWD geoVISION resistivity tool (GVR) are presented in Figure **F5.** Logging data included gamma radiation and resistivity, as well as drilling parameters (rate of penetration [ROP], stick-slip, etc.). Two sets of data were collected corresponding to two data sets of drilling operations (See **"Operations"**): Run 1 for the interval between 2590 and 3033 m LWD depth below rig floor (LRF) and Run 2 for the interval between 3034 and 3107 m LRF, with a repeat log interval between 2900 and 2972 m LRF. Detailed discussion and interpretation of individual logs are incorporated into the subsequent disciplinary sections (i.e., lithology, structural geology, and physical properties).

Depth correction of LWD/MWD data

Depth references are shown graphically in Figure F6. The height of the rig floor (rotary table) is 28.3 m above sea level (presuming minimal variation in this parameter during drilling operations), and the water depth is reported as 2523.7 m. LWD/MWD log depths are tied to the drillers depth at the rig floor, such that LWD/MWD depth is equal to drilling depth (LRF = DRF, LWD depth below seafloor [LSF] = DSF).

Operations

The Hole C0010A borehole assembly included TeleScope MWD and GVR, which measure resistivity, gamma ray, resistivity image, and drilling parameters. After making up the MWD-GVR assembly at 1230 h on 6 August 2009, a shallow tool string hole test was conducted at 1345 h before running into the water while the *Chikyu* drifted to a low-current area. At 1230 h on 7 August, the drilling assembly reentered Hole C0010A through the 20 inch conductor pipe to 41 m DSF, and drilling began at 1315 h at a controlled ROP of 20 m/h (16.6 m/h average). The section between 2846 and 2858 m LRF was relogged during this run (Run 1) because of poor data quality. Stick-slip increased with depth (Fig. F5), so sweeps of Hi-Vis mud were conducted at pipe connections, and a wiper trip was conducted at 1615 h to 2573 m LRF (inside the conductor pipe). A repeat section was logged again between 2921 and 2928 m LRF, and the hole was reamed at several other depths to improve data quality and reduce stick-slip. Drilling stopped at 1245 h on 9 August to move the *Chikyu* away from a typhoon's path. At 0300 h on 12 August, the *Chikyu* returned to the drillsite. After reentry at 0600 h, the bit was run to 2900 m LRF to relog the critical interval in the vicinity of the megasplay fault between 2900 and 2970 m LRF. At 1145 h, drilling resumed from 3034 m LRF at a controlled ROP of 30 m/h. Stick-slip decreased in this interval, and drilling finished at 1715 h after reaching a target depth of 3107 m LRF.

Log data quality

Available data

Hole C0010A was jetted down for the 20 inch conductor pipe and then drilled from 2593 m DRF to 3107 m DRF (TD) with a 12¼ inch MWD-GVR drilling assembly (see Fig. F3 in the "Methods" chapter). Real-time data from both MWD and GVR and memory data from GVR were environmental and inversion corrected. Available data from the MWD-GVR are listed in Table T2 in the "Methods" chapter.

Repeatability

To improve data quality, we conducted a repeat log between 2900 and 2972 m LRF in Run 2 (after hole reentry on 7 August). Comparison between the first logs (Run 1) and the repeat section (Run 2) indicate significant differences in both the gamma ray and resistivity data and in the bit resistivity images. It is not clear whether these differences are related to seawater invasion during ~2 days of WOW or to borehole rugosity changes because of reaming and relogging.

Data quality

In comparison to the data from Hole C0004B, which is 3.5 km east along strike, Run 1 for the top section of the Hole C0010A exhibited continuous high stick-slip. In addition, high heave (1.2–2.5 m) because of a passing strong typhoon from the west and another coming from the south may have affected data quality. The image data from Site C0010 showed conspicuous horizontal banding with sharp contacts between zones of differing resistivity. The bands were typically ~20 cm thick in data collected during Run 1. In the repeated log of the interval between 2900 and 2972 m LRF during Run 2, the horizontal bands are less conspicuous. Nevertheless, these artifacts of the logging process obscured shallowly dipping structures and biased our interpretation toward features with steep dips. Logs from the repeated log section (Run 2) showed enlarged breakouts relative to Run 1. Overall, we would rate the quality of the data of both runs as fair; however, data from Run 1 are of higher quality because of reduced effects from reaming the hole. Primary conditions that may have affected log quality include the relatively high heave and significant stick-slip in tool rotation during imaging (Fig. F5). Unlike resistivity, gamma radiation exhibits less variability and changes gradually across the boundaries.

Lithology

We defined three logging units at Site C0010 on the basis of LWD/MWD measurements (gamma ray and bit resistivity) and guided by previous logging and coring results at nearby Site C0004 (Expedition 314 Scientists, 2009b; Expedition 316 Scientists, 2009). We interpret logging Unit I (0–182.8 m LSF) as slope sediments deposited on top of an underlying thrust wedge. This unit generally correlates with Site C0004 lithologic Unit I. It is subdivided into Subunit IA (0–

161.5 m LSF), composed of hemipelagic mud and minor turbidite interbeds, and Subunit IB (161.5–182.8 m LSF) composed of mass transport deposits probably reworked from the thrust wedge. Logging Unit II (182.8–407.0 m LSF) represents accreted sediments that are part of a thrust wedge and correlate with Site C0004 lithologic Units II and III. However, the log character of sediments in the thrust wedge at Site C0010 differs from that at Site C0004, most notably in that sediments appear to be more clay rich at Site C0010. Our interpretation of logging Unit III (407.0–555.1 m LSF) corroborates the idea of slope deposits being overridden by the megasplay fault, suggested at Site C0004, which are lithologically similar to the slope sediments of Subunit IA above and correlate to Site C0004 lithologic Unit IV.

Log characterization and lithologic interpretation

Three logging units are defined at Site C0010 (Figs. F7, F8). Seismic reflection profiles indicate that similar lithologic sequences may occur at Sites C0004 and C0010 (Moore et al., 2009). Although in detail the sites are not identical in seismic reflection data, observations from Site C0004 (Expedition 314 Scientists, 2009b; Expedition 316 Scientists, 2009) provide valuable constraints on lithologic variations at Site C0010. Data acquired during Expeditions 314 and 316 at Site C0004 show that lithologic changes are best defined based on gamma ray measurements, whereas changes in resistivity values may vary independently from lithology and show some variations related to porosity (Fig. F8).

Unit I (0–182.8 m LSF)

Logging Unit I is divided into Subunits IA and IB. Subunit IA (0–161.5 m LSF) is characterized by a gradual increase in gamma ray (from 50 to 85 gAPI [American Petroleum Institute]) with depth (Fig. F7). Bit resistivity values increase from 0.6 to 0.8 Ωm within the same depth interval. We define the Subunit IA/IB boundary based on a sharp decrease of gamma ray values at ~161.5 m LSF. Subunit IB (161.5–182.8 m LSF) is characterized by lower gamma ray values (<65 gAPI) than those found in the base of logging Subunit IA (>80 gAPI) (Fig. F7). Bit resistivity values decrease slightly at this depth from 0.7 to 0.65 Ωm. The base of logging Subunit IB is defined by a sharp increase in bit resistivity. Gamma ray values in Subunit IB are dissimilar to those in Subunit IA above but similar to those in Unit II below.

Unit II (182.8–407.0 m LSF)

Logging Unit II is characterized by large-amplitude variations in gamma ray values (65–120 gAPI), with an overall increasing trend and higher values than units above and below. Six ~7–15 m thick intervals of low gamma ray (<70 gAPI) are observed within this unit (Fig. F7). Bit resistivity values are also more variable (0.9–1.7 Ωm) than those in logging Unit I (0.6–0.8 Ωm) and indicate six conductive intervals that correspond to the intervals of low gamma ray values. It is also noteworthy that the magnitude of variations in both gamma ray and bit resistivity (e.g., 373–386 m LSF) seen in logging Run 1 are reduced during relogging of the hole (Run 2) (Fig. F7). The Unit II/III boundary is based on the sharp decrease in both gamma ray and bit resistivity values. This boundary also coincides with the lower boundary of the thrust wedge (See **"Log-Seismic integration"** and **"Structural geology"**).

Unit III (407.0–555.1 m LSF)

Logging Unit III is characterized by constant gamma ray values (70–75 gAPI) (Fig. F7). Bit resistivity also remains relatively constant in Unit III, ranging from 0.8 to 0.9 Ωm. The low gamma ray readings (<40 gAPI) between 513–515 and 522–530 m LSF correlate well with the depths of low bit resistivity readings (<0.7 Ωm) (Fig. F7).

Lithologic interpretation

Interpretations of seismic reflection data (Moore et al., 2009) and results from Site C0004 (Expedition 314 Scientists, 2009b; Expedition 316 Scientists, 2009) combined with log data from Site C0010 suggest that three distinct lithologic packages occur at Site C0010, comprising from top to bottom: slope deposits, thrust wedge, and overridden slope deposits. Below, we provide a lithologic interpretation of Site C0010 logging units based on these combined data sets (Fig. F8).

Site C0010 logging Subunit IA displays gamma ray and bit resistivity patterns similar to Site C0004 Unit I (Fig. F8). We interpret this unit as slope sediments deposited on top of logging Unit II (thrust wedge). Based on gamma ray values, slope sediments in the 70–158 m LSF depth interval are characterized by higher clay mineral content than similar sediments at Site C0004 and likely represent hemipelagic mud with minor thin, fine-grained turbidite interbeds. We interpret Site C0010 Subunit IB as mass transport deposits composed of material reworked from upslope Unit II equivalent material, based on (1) similar gamma ray and bit resistivity measurements at Sites C0004 (~78–96.2 m LSF) and C0010 (161.5–182.8 m LSF), (2) comparison with the cored interval at Site C0004 that includes brecciated material probably reworked from the thrust wedge, and (3) seismic data that suggest Site C0010 Subunit IB includes deformed slope sediments overlying the thrust wedge (Moore et al., 2009) (Fig. F8).

We interpret logging Unit II as a thrust wedge that is part of the accretionary prism, correlating with Site C0004 lithologic Units II and III (Fig. F8). The thrust wedge at Site C0010 differs from that at Site C0004 in that it has higher gamma ray values. This may indicate that Unit II is mostly composed of pelagic mud or poorly lithified pelagic mudstone with a higher clay mineral content, distinct from the hemipelagic mud observed at Site C0004 (Expedition 316 Scientists, 2009). Higher resistivity in Site C0010 logging Unit II relative to logging Units I and III and Site C0004 lithologic Units II and III (equivalent to Unit II at Site C0010) may indicate increased compaction, or alternatively, increased tortuosity associated with higher clay content (see **"Physical properties"**). Local decreases in gamma ray and bit resistivity values may reflect (1) interbeds of hemipelagic silty mud within the overall compacted pelagic mud, (2) breakouts or fracture zones (see **"Structural geology"**), or (3) artifacts related to acquisition of the data as indicated by differences in gamma ray values between Runs 1 and 2 (Fig. F8).

Logging Unit III is composed of slope sediments overridden by the thrust wedge and correlates with Site C0004 lithologic Unit IV (Fig. F8). On the basis of the LWD data and coring results from Site C0004, we interpret Unit III as hemipelagic mud with minor turbidite interbeds and rare volcanic ash layers. Coarser grained turbidite beds may occur at 513–515 and 522–530 m LSF where gamma ray values decrease markedly.

Structural geology

We measured the attitudes of faults and bedding and borehole breakout orientations in Hole C0010A from LWD resistivity image data. We logged the borehole to 3034 m LRF (482 m LSF) in Run 1. After assessing data from Run 1 during a weather-related suspension of operations, we relogged between 2900 and 2970 m LRF (347–418 m LSF) to attempt to improve data quality and then continued logging while drilling from 3034 m LRF to TD at 3107 m LRF (482–555 m LSF). Data from both logging runs are presented here. The discussion below includes structural data, a discussion of data bias, borehole breakout analysis, and description of fault resistivity.

Structural data

The resistivity image data are horizontally "striped," reflecting artifacts related to tool heave because of ship motion. This artifact hindered, but did not preclude, our ability to interpret structural and sedimentary features. We used several criteria for interpreting bedding, including: (1) being able to fit a sine curve to the flattened image of the cylindrical borehole wall, (2) having resistivity values extending across the entire image, and (3) having consistent resistivity values above and below a feature (Fig. F9). Our criteria for interpreting faults are the same as those for bedding except that we interpreted faults only where inconsistent resistivity values were apparent above and below the fault (Fig. F10).

Most of the bedding dips eastward with significant scatter in dip values and orientation (Fig. F11; see C0010_T1.XLS in STRUCGEOL in **"Supplementary material"**). Bedding in slope deposits above the thrust wedge dips moderately to the east, at the top of the thrust wedge it dips moderately to the west, and bedding below the thrust wedge dips both east and west (Fig. F12; see C0010_T1.XLS and C0010_T2.XLS in STRUCGEOL in **"Supplementary material"**). Easterly dipping bedding below the thrust is not consistent with dips observed in the seismic reflection data.

Most of the faults occur within the base of the thrust wedge and exhibit a wide range of dips to the west and south (Fig. F13). The two logging runs through this section (2900–2970 m LRF yield different interpretations. Logging Run 1 data (during drilling) indicate more shallowly west-dipping faults. Run 2 data, recorded after reaming the open hole, indicate many more steeply dipping faults; the shallowly dipping faults from Run 1 data are not observed in Run 2. Figure F12 shows data from Run 1 between ~50 and 482 m LSF, except between 347 and 418 m LSF where Run 2 data are shown, plus data acquired while deepening the borehole from 482 m LSF (TD of Run 1) to TD at 555 m LSF.

We also documented whether the faults were resistive or conductive, an interpretation made difficult because of the generally poor imaging data quality. However, of the 27 faults observed, 4 were resistive, 8 conductive, and 15 undetermined (see C0010_T2.XLS in STRUCGEOL in **"Supplementary material"**).

Discussion

There is little repeatability between the two logging efforts. Only three faults were interpreted with similar dips and dip directions in both runs (Fig. F14; see C0010_T2.XLS and C0010_T3.XLS in STRUCGEOL in **"Supplementary material"**). Logging Run 1 exhibits more shallowly dipping faults. The vertical resolution is probably worse than in Run 2 because of significant tool heave. A total of 18 new faults were observed in Run 2 after reaming the open hole; however, 9 faults from Run 1 were missed by Run 2 (Fig. **F14**). This could be partly due to errors in interpretation, but there are biases in both data sets: Run 1 shows more shallowly dipping faults but missed many others, whereas Run 2 shows more steeply dipping faults but missed the shallowly dipping faults.

Borehole breakouts

At Site C0010, LWD resistivity images show bands of low resistivity on opposite sides of the borehole. We interpret these as borehole breakouts; the enlarged borehole produces a low-resistivity signal because of the increased conductive water between the LWD resistivity tool and the borehole wall (Zoback, 2007). Criteria for mapping breakouts include observing low-resistivity areas on opposite sides of the borehole (180° apart) or a single area of low resistivity that directly extends as a vertical continuation from one member of an opposed pair. We mapped borehole breakouts from both logging Runs 1 and 2. In general, breakouts were most clearly imaged in Run 1 data and in Run 2 data where the borehole was deepened from 482 to 555 m LSF beyond Run 1. The borehole changed between the two logging runs (see also **"Physical properties"**) where the logging runs overlap in the relogged section (348–418 m LSF); breakouts enlarged in size in the 3 days between the two runs (Fig. **F15**).

Breakouts are rare in the slope deposits, common in the thrust wedge, and abundant in the overridden slope deposits below the thrust wedge (Fig. **F16**; see C0010_T4.XLS in STRUCGEOL in **"Supplementary material"**). The poor image quality, especially in the slope deposits and thrust wedge, made picking the breakouts more difficult than in the overridden slope deposits. The mean azimuth of all breakouts is 55°–235° (Fig. **F17**). The orientations are consistent, with minimal scatter, in the overridden slope deposits below the thrust wedge (Fig. **F16**). Moving uphole, the orientations shift sharply to higher values (more east–west) in the thrust wedge (above 407 m LSF) and then gradually rotate within the thrust wedge and overlying slope deposits to a more northeast–southwest orientation upsection.

We interpret breakout orientations at 55°–235° as S_{hmin}, with S_{Hmax} 90° to this direction at 145°–325° (Zoback, 2007). This S_{Hmax} direction is parallel or subparallel to all other S_{Hmax} directions from the Kumano transect, except at IODP Site C0002 (Fig. **F18**) (Tobin et al., 2009a). The base of the thrust wedge at Site C0010 is marked by a transition in breakout orientation (407 m LSF). This sharp transition contrasts with the uniform trend of breakout orientation with depth at Site C0004, which extends from the overlying slope deposits down through the thrust wedge and into the overridden slope deposits (Expedition 314 Scientists, 2009b).

Summary

Mapped faults are concentrated mostly near the base of the thrust wedge and immediately below in the uppermost overridden slope deposits. These faults mostly dip to the south and west and are steep relative to reflectors in the thrust wedge on the seismic reflection data (Fig. **F19**). However, neither the faults nor the bedding orientations show clear trends, in contrast to Site C0004 where data quality was better and measurements were more numerous (Expedition 314 Scientists, 2009b). The breakouts show that S_{Hmax} trends to the northwest, similar to other sites on the outer slope along the NanTroSEIZE transect (IODP Sites C0001, C0004, and C0006) (Fig. **F18**). The sharp discontinuity in stress orientation across the base of the thrust wedge (Fig. **F16**) is consistent with a fault discontinuity at this depth (Barton and Zoback, 1994) but contrasts with the more uniform but constantly changing trend of breakouts across the base of the thrust wedge at Site C0004 (Expedition 314 Scientists, 2009b). The enlargement of breakouts during the interval between logging runs indicates that breakout width grows with time in this environment, in contrast to observations from more lithified rocks (Zoback, 2007).

Physical properties

Logging

Physical property analysis at Site C0010 utilized NGR and five sets of resistivity data from the GVR (see **"Logging"** in the "Methods" chapter). In addition, porosity is estimated from resistivity (for details, see **"Physical properties"** in the "Methods" chapter). This porosity is based on the total water content of the formation, which includes both pore water and water bound in hydrous minerals (e.g., clay minerals and biogenic opal). At Site C0010, however, this approach was hampered by the absence of core material, cuttings, or density log data to calibrate the transform from resistivity to porosity.

Resistivity logs

We acquired resistivity measurements at a spatial resolution of 0.1–0.15 m. These include bit resistivity, ring resistivity, and shallow-, medium-, and deep-button resistivity (Fig. F20; also see Table T3 in the "Methods" chapter). The buttons are longitudinally spaced along the LWD tool. Their spacing provides depths of investigation of ~1, 3, and 5 inches, respectively, and can be used to quantify invasion of drilling fluid. Depths of investigation of bit and ring resistivity are 7 and 12 inches, respectively.

Ring resistivity ranges between 0.7 and 0.9 Ωm in the uppermost portion of the logged succession within the slope sediments of logging Unit I (0–182.5 m LSF) (Fig. F20). Resistivity within the overridden slope apron deposits of Unit III (407–554 m LSF) ranges from 0.8 to 1.2 Ωm and exhibits a very gradual increase with depth (Fig. F20). In between, the resistivity of the thrust wedge (Unit II) is significantly higher. In its upper portion (~182.5–260 m LSF), below a ~10 m interval where resistivity values remain constant, resistivity increases linearly to values of ~1.6 Ωm. Below this, between 260 and 407 m LSF, resistivity is variable. Focussing on ring resistivity, values range from peak values of 2.5 Ωm to minimum values of ~1.5 Ωm over distances of ~10–20 m (Fig. F20). The two zones where resistivity varies significantly are delineated in gray on Figure F20.

The hole was abandoned at ~460 m LSF because of an incoming storm (see **"Operations"** and **"Logging and data quality"**). Then, when the hole was reentered, a section of the hole was relogged (red lines, Fig. F20). The resistivities acquired during the second logging run (Run 2) from 348 to 418 m LSF are different than those collected in Run 1 (see Fig. F20, compare black and red curves). In Run 2, focussing again on ring resistivity, between 348 and 370 m LSF, values scatter around 1.7–1.8 Ωm, whereas the zone from ~370 to 407 m LSF exhibits values around 1.2–1.3 Ωm (Fig. F20). Below ~407 m LSF, values drop back to ~1.0 Ωm, a value similar to those from Run 1 (Fig. F20). The data quality over the relogged interval is questionable (see below and **"Logging and data quality"**).

Comparison of the different resistivity logs and qualitative estimation of invasion

The five resistivity measurements show the same overall trend with depth (Fig. F20). In general, the deep, medium, and shallow buttons integrate a smaller volume of rock than ring or bit resistivity. Hence, data from these buttons exhibit larger fluctuations than bit and ring measurements. Between 260 and 407 m LSF, the medium-button data appear very noisy and exhibit higher values than the deep-button data, which is the opposite of that expected; as a result, we believe the medium-button data are not reliable (Figs. F20, F21). Anomalous peaks in resistivity (>5 Ωm) are also observed in the deep-button curve from 350 to 390 m LSF. These excursions are not observed in the relogged data set (cf. Figs. F20, F21) and may be the consequence of bad hole conditions (e.g., cuttings caught between the sensors and the formation), consistent with high stick-slip during the first pass through that zone (Fig. F20). Overall, we observe that data from the entire 260–407 m LSF interval are significantly different for the shallow and deep buttons. Using the difference between the deep and shallow buttons as a proxy for invasion of seawater, and thus the permeability of the formation, we infer three zones of enhanced permeability: from 182.5 to 260 m LSF in Unit II, from 350 to 407 m LSF in Unit II, and from 522 to 530 m LSF in Unit III (Fig. F21). These intervals coincide with zones of lower overall resistivity, especially at the bottom of Unit II (Fig. F21).

In the relogged interval (348–418 m LSF in Run 2), where the deep–shallow difference is most pronounced, resistivity curves flatten as the depth of investigation decreases (namely from ring to shallow-button resistivity measurements; see Figs. F20, F21). We interpret this as the effect of deep invasion of cold seawater into the formation, which may have occurred during the ~2 days between Runs 1 and 2.

Estimation of porosity from resistivity

Estimation of bottom-hole temperature

We estimated a temperature profile in the formation using a surface heat flow of 53.6 mW/m^2 and thermal conductivity measurements from nearby Expedition 316 Holes C0004C and C0004D (Kimura et al., 2008). We assume a 2°C bottom water temperature and a steady-state conductive temperature profile. The estimated temperature at the bottom of the hole is 23.4°C.

Estimation of porosity

We calculated seawater electrical resistivity using the temperature profile estimated above and used it to evaluate the formation factor from the ring resistivity (see **"Physical properties"** in the "Methods" chapter). Formation factors were then converted to estimated porosity values using Archie's law (Archie, 1942). Because no other porosity measurements were available to constrain the Archie's law parameters, we used the same parameters obtained for Site C0004 ($a = 1$, $m = 2.3$) (Conin et al., 2008; Kinoshita, Tobin, Ashi, Kimura, Lallemant, Screaton, Curewitz, Masago, Moe, and the Expedition 314/315/316 Scientists, 2009), where the sediments were drilled with LWD during Expedition 314 (Kinoshita et al., 2008) and cored during Expedition 316 (Kimura et al., 2008) (Fig. F22). It is important to recognize that the

Archie's law parameters were defined at Site C0004, so porosity values estimated from resistivity in the thrust wedge at Site C0010, where resistivity and gamma ray values differ from those at Site C0010 (and thus lithology may be different), should be viewed with caution. However, even considering a large range of Archie's law parameters (m ranging from 2.1 to 2.6), the estimated porosities do not change dramatically (Fig. **F23**).

We used the ring resistivity measurement here because it has a penetration depth sufficiently large to exclude effects of seawater invasion. Estimated porosity decreases gradually from 74% to 63% in the uppermost part of the logged section (42–182.5 m LSF). The same gradual decrease continues below the Unit II/III boundary where computed porosity from Runs 1 and 2 range from 52% at the boundary to 48% at the bottom of the hole. If we assume that porosity decreases exponentially with depth because of vertical compaction (e.g., Athy, 1930), Units I and III can both be fit with the same compaction trend:

$$\phi = 0.7 \times \exp(-z/1500),$$

where

z = depth below seafloor (meters), and
ϕ = fractional porosity.

Unit II clearly departs from this compaction trend, and based on the estimated porosities, most of the sediment in this section appears more consolidated than the slope sediments above and below. At the top of Unit II, computed porosity values drop sharply to 57% and gradually decrease to reach 38% at 340 m LSF (Fig. **F22**). In the central portion of Unit II (~260 to ~340 m LSF), estimated porosity fluctuates and exhibits two intervals with lower values (porosity of ~38% from ~265 to ~270 m LSF and ~289 to ~305 m LSF). These fluctuations are consistent with excursions in the gamma ray log (see **"Lithology"**). These apparent fluctuations may reflect differences in composition that reduce resistivity; alternatively, they may reflect true porosity differences related to variations in stress history, local changes in lithology, and/or the presence of fractures or faults.

From 348 to 407 m LSF, estimated porosity differs considerably between Runs 1 and 2 because the resistivity differs markedly. For data from Run 1, computed porosity increases gradually from 38% at 348 m LSF to 41% at 407 m LSF and includes two zones with higher values, the first between 373 and 385 m LSF (~46%) and the second between 390 and 395 m LSF (~42%). At the Unit II/III boundary, values increase sharply to 52%. The computed porosity profile for Run 2 approximately mirrors the trend of Run 1 but is shifted to higher values except for one interval where the two runs are in good agreement (402–417 m LSF, Fig. **F22**). This shift may result from deep invasion of the formation by seawater in the ~2 days between the two logging runs (see **"Operations"**).

When comparing resistivity-derived porosities at Site C0010 (obtained assuming three different Archie's law parameters: $m = 2.1$, $m = 2.3$, and $m = 2.6$) (Fig. **F23**) to those at Site C0004, the estimated porosity of Unit II (thrust wedge) at Site C0010 is lower than that of the thrust wedge at Site C0004 (see Conin et al., 2008; Kinoshita, Tobin, Ashi, Kimura, Lallemant, Screaton, Curewitz, Masago, Moe, and the Expedition 314/315/316 Scientists, 2009; Expedition 316 Scientists, 2009). This difference is driven by considerably higher resistivity in the thrust wedge at Site C0010 relative to Site C0004. In contrast, the compaction trend of the slope apron and overridden sediments at Site C0010 is similar to the one estimated for Site C0004. The lower computed porosity in the thrust wedge at Site C0010 bears some uncertainty because we used the same Archie's parameters as Site C0004, yet the lithologies likely differ between the two sites (see also **"Lithology"**). However, based on the fact that estimated porosity does not change substantially even when considering a wide range of values for the Archie parameter (cf. Fig. **F23**), we suggest that the higher resistivity at Site C0010 is likely to result, at least in part, from a difference in compaction state related to modern stress state or burial history.

Log-Seismic integration

Seismic velocity structure and well tie

No check shot data were acquired, and there were no sonic logs run at Site C0010. We examined the correlation between borehole data and seismic data at IODP Sites C0003 and C0004 (Tables **T3, T4**), where check shots were taken to correlate the seismic data to the borehole logs. These sites are located near Site C0010 and penetrated similar formations (Tobin et al., 2009b) (Figs. **F24**). We then used check shot data from Site C0004 to correlate borehole data with seismic data at Site C0010 (Table **T3**).

The one-way traveltime of the check shot data for a given depth below seafloor is greater, and consequently the interval velocity is lower, at Site C0004 than at Site C0003 (Figs. **F25, F26**). Site C0003 is located northwest of Site C0004 and penetrates the thrust sheet in a more landward location (Fig. **F24**). Higher velocity at Site C0003 may reflect greater compaction in this region. Sites C0004 and C0003 have relatively thin sediment carapaces (~80 m thick) above the thrust wedge (Figs. F19, F27), whereas at Site C0010, ~180 m of sediment overlies the thrust wedge (Fig. F28).

At Site C0004, we map the top of the thrust wedge as a positive polarity seismic reflection (blue) that overlies the relatively transparent thrust wedge (Fig. F19); we call this the "top wedge" seismic surface. We also map the base of the thrust wedge as a positive polarity seismic reflection (blue) and call it the "base wedge" seismic surface (Fig. F19). These reflections match the top and base of the thrust wedge mapped on seismic data by Expedition 314 scientists (see figs. F34 and F43 in Expedition 314 Scientists, 2009b). Based on the Site C0004 check shot, we find that the top wedge surface at Site C0004 overlies the top of lithologic Subunit IIA by a few meters (Expedition 316 Scientists, 2009), and it lies at the base of the logging Unit I boundary (Expedition 314 Scientists, 2009b) (Fig. F19). The base wedge seismic surface at Site C0004 lies at the boundary of lithologic Units III and IV and just above the logging Unit II/III boundary (Fig. F19).

At Site C0004, resistivity increases at the top of the thrust wedge but does not change substantially beneath the thrust wedge. Velocity increases with depth at the top of the thrust wedge and increases abruptly just above its base (Fig. F19). A synthetic seismogram produced by Expedition 314 scientists produced many, but not all, of the seismic characteristics at Site C0004 (Expedition 314 Scientists, 2009b).

We also correlated Site C0003 log data with the seismic data (Fig. F27; Table T4). As at Site C0004, a strong positive (blue) reflection is present at the top of the thrust wedge. In this location, Expedition 314 scientists also correlated the top of the thrust wedge to this strong positive reflection (Expedition 314 Scientists, 2009b). They interpreted the top of the thrust wedge (logging Unit II) as a very sandy interval with extreme borehole washout.

We used the Site C0004 check shot to tie the seismic data to the well data (logging and units) at Site C0010 (Fig. F28; Table T3). We mapped a weak positive polarity (blue) reflection at the top of the thrust wedge that we called the top wedge. We mapped a negative polarity (red) reflection at the base of the thrust wedge that we called the base wedge (Fig. F28). The top wedge surface lies ~15 m below the Subunit IB/Unit II boundary (Fig. F28), and the base wedge surface lies ~4 m below the Unit II/III boundary (Fig. F28) (see "Lithology"). We believe that our top wedge surface appears to underlie the Subunit IB/Unit II boundary because the time-depth correlation applied from Site C0004 is not correct. At Site C0010, the thrust wedge is buried by ~100 m more sediment than at Site C0004, and these sediments have lower velocities than those within the thrust wedge (Fig. F19). Therefore, between 100 and 200 mbsf, the velocities applied from Site C0004 are higher than those at Site C0010; the result is that our mapped seismic surface at the top of the thrust wedge appears deeper than reality. We suggest that the velocity difference between Site C0004 and Site C0010 is reduced at the depth of the base of the thrust wedge, and therefore the correlation is improved at this depth.

Comparison of Sites C0010 and C0004

There was considerable discussion on the ship about the quality of the LWD data during Run 1 at Site C0010 (see "Physical properties"). During this initial LWD drilling run, there was significant ship heave and stick-slip, particularly in zones where we observe lower gamma ray and resistivity values (Fig. F5). As a result, a section of the hole was relogged around the fault zone target, and data from both logging runs were compared (see "Logging and data quality"). After extensive discussions between the shipboard party and the Schlumberger engineers, we concluded that the resistivity and gamma ray data acquired in the initial logging run (Run 1) most accurately record in situ properties. We compare these data with those from Site C0004 below.

At Site C0010, gamma ray values in the thrust wedge increase from 65 gAPI at the top, to 120 gAPI in the center of the wedge, and back to 80 gAPI at the base (Fig. F29). Superimposed on this trend are a number of ~7–15 m thick cycles where gamma ray drops to between 60 and 80 gAPI. Resistivity parallels gamma ray throughout the borehole (Fig. F29). At the top of the thrust wedge, there is an abrupt increase in resistivity with depth from 0.75 to 1.25 Ωm. Resistivity increases with depth between the top and center of the thrust wedge to a value of ~2.5 Ωm at ~2860 mbsl (Fig. F29) and then decreases to the wedge base.

At Site C0004, gamma ray and resistivity values vary much less downhole than at Site C0010. Gamma ray values range from 60 gAPI above the thrust wedge, to 70–80 gAPI within it, and back to 60–70 gAPI in the underlying section (Fig. F29). Resistivity ranges from 1.0 Ωm above the wedge to 1.5 Ωm in the wedge. Resistivity declines very slightly to values of ~1.25 Ωm below the wedge.

Data from Sites C0004 and C0010 are overlain in the center of Figure F29, and the difference is striking. Gamma ray values are higher at virtually all depths at Site C0010 relative to Site C0004; gamma ray values differ by 40 gAPI within the thrust wedge between the two sites (Fig. F29). Resistivity within the lower half of the thrust wedge is also higher at Site

C0010 than at Site C0004 by ~1 Ωm. Above and below the thrust wedge, resistivity at Site C0010 is slightly less than at Site C0004.

From the higher gamma ray response at Site C0010, we interpret that the thrust wedge at Site C0010 has a greater clay fraction and is finer grained than the thrust wedge at Site C0004. We suggest that resistivity within the wedge is higher at Site C0010 for two reasons: (1) the rock is finer grained, pore throats are more tortuous, and electrical resistivity is greater; and (2) the rock is more consolidated (see "Physical properties"). The cyclic decreases in resistivity and gamma ray at Site C0010 record the presence of coarser grained material (more silt- or sand-sized quartz) that is less consolidated. These intervals appear similar in composition to the material throughout the thrust wedge at Site C0004 (i.e., gamma ray and resistivity values are similar) (Fig. F29).

The wedge at Site C0010 is characterized by greater seismic reflection amplitudes than at Site C0004 (Fig. F30). We infer that the compositional cycles within the thrust wedge at Site C0010 drive differences in velocity and density (impedance) that generate seismic reflections. These results suggest significant compositional variation in the thrust wedge over a scale of only a few kilometers along the strike of Nankai Trough. A notable feature of seismic profiles across this thrust wedge is that the negative polarity reflector at the base of the wedge is weak at the tip of the thrust wedge and increases in amplitude where it is more deeply buried (Figs. F31, F32). Increasing consolidation in the thrust wedge relative to the underlying material with distance downdip explains this observation.

Observatory

Sensor dummy run test

Instrument preparation

All equipment except the strainmeter was loaded onto the *Chikyu* by supply boat on 3 August 2009; the strainmeter was loaded on 10 August because it needed repairs from shipping damage incurred between 10 and 13 July during transportation to Shingu, Japan. Prior to the dummy run test, sensor running tests for the strainmeter and accelerometer-tiltmeter were conducted to confirm that sensors were working well with no damage during shipment to the *Chikyu* (Figs. F33, F34). The instrument carrier was passed through a 9⅝ inch casing joint before the sensor dummy run test to ensure that there would be sufficient clearance to reenter the hole (Fig. F35). Two seismometers, an accelerometer-tiltmeter, and eight miniature temperature loggers (MTLs) were attached to the instrument carrier on 17 August and a ninth MTL was attached to a pup joint at the bottom of the assembly (Fig. F36). Dummy run test sensor tree configurations are shown in "Observatory" in the "Methods" chapter. Additional brackets were attached to the carrier at the top and bottom of each sensor to prevent loss or damage during drifting through the high-current area and reentry (Fig. F36).

First dummy run test

The sensor dummy run test began on the morning of 18 August. The dummy run assembly was made up and lowered from the rig floor at 1502 h on 18 August. The current speed was ~0.7 kt. The sensor tree was lowered to 1000 m DRF at 1730 h on 18 August when the *Chikyu* started drifting to Site C0010 at 1 kt. The sensor tree was located 4 nmi from Site C0010 at 1700 m DRF at 0915 h on 19 August. The Kuroshio Current was too strong (4.8 kt) to deploy the ROV around this area. Therefore, the *Chikyu* needed to move to a low-current area to deploy the ROV from 1345 to 1930 h on 19 August. The ROV was deployed to visually examine the sensor tree while in the low-current area and documented loss of the strainmeter and one seismometer (CMG3T) from the instrument carrier. Therefore, we decided to retrieve the sensor tree before attempting reentry in Hole C0010A (Fig. F37).

After the sensor tree was retrieved, the seismometer and accelerometer-tiltmeter were removed from the instrument carrier and the condition of the accelerometer-tiltmeter sensor was checked. Data recording had stopped by the time the check was conducted on board the *Chikyu*. Recorded data in the memory were checked and found to cover the time period from 0645 h on 18 August to 0911 h on 19 August. A capacitor on the accelerometer sensor was found to be damaged (connections to the circuit board snapped), probably as a result of strong vibration. After repairing the snapped capacitor, the accelerometer-tiltmeter worked well.

Second dummy run test

The second dummy run reentry test employed only the accelerometer-tiltmeter, to evaluate shock acceleration and vibration during reentry (Fig. F38). Because we lost the strainmeter, we replaced it with a dummy strainmeter for the reentry test. We also needed to strengthen the instrument carrier to prevent losing sensors. Therefore, additional protectors were welded to the instrument carrier to hold the sensors, and we patched the cracked sections of the instrument carrier with welded plates (Fig. F39). The dummy run test assembly was made up and lowered to 1689 m DRF at 1507 h on 20 August. The current speed was ~0.7 kt, and drifting to Site C0010 at a speed of 0.7 kt began at 1815 h on 20 August, arriving at Hole C0010A at 0923 h on 21 August.

The reentry test was conducted in strong currents (4.3 kt) under good sea-surface conditions from 0923 to 1034 h on 21 August. The bottom of the sensor tree was stabbed into the wellhead three times to 5–7 m DSF (Fig. **F40**). During the third reentry, the bottom thread of the 3½ inch VAM top tubing (the bottommost parts of the sensor tree) hit the reentry cone two times. During observation of the sensor tree via the ROV camera, there was no obvious repeated slamming or extreme vibration during the reentry procedure. After reentry testing, the sensor tree was pulled out of the hole.

After the dummy run sensor tree was recovered on deck, the accelerometer-tiltmeter status was checked. Data recording had already stopped when checked on board the *Chikyu.* The recording period in the second dummy run test only covered from 0746 to 2226 h on 20 August. No acceleration and tilt data were recorded during hole reentry. One fuse on the electronic circuit board was discovered to be loose, which may have been caused by strong VIV from the Kuroshio Current during drifting.

Acceleration and tilt data

In the first dummy run test, acceleration and tilt data were collected from 0645 h on 18 August to 0911 h on 19 August. Examples of the time series data are shown in Figure **F41.** Power spectral density (PSD) images of acceleration for each axis were generated from the collected acceleration data (Fig. **F42**). In the first dummy run, three events (A, B, and C) can be identified from the PSD image (Fig. **F42A**). Event A is characterized by the broad high PSD at a frequency of 0.1–10 Hz at ~0542 h on 19 August. The location of Event A (33°18.2067′N, 136°34.2046′E) is indicated in Figure **F43.** Event B shows a clear offset in resonance frequency occurring at 0652 h on 19 August, implying a change in the mass of the sensor tree occurred at this time. Before this event, the resonance frequencies were 0.3–0.5 and 0.9–1.6 Hz for x-axis acceleration, 0.7–1.3 and 1.4–1.6 Hz for y-axis acceleration, and 2.2–2.8 and 3.7 Hz for z-axis acceleration. After this event, the resonance frequencies changed to 1.9 and 6.0 Hz for x-axis acceleration; 1.4–2.2 Hz for y-axis acceleration; and 4.0, 5.0, and 8.3 Hz for z-axis acceleration. This change likely identifies the event when the strainmeter and the assembly below (~900 kg in total) were dropped. The location (33°17.3197′N, 136°35.3139′E) where this occurred is indicated on the map (Fig. **F43**). The peak to peak amplitudes for acceleration data are 19 m/s^2 for x-axis, 21 m/s^2 for y-axis, and 25 m/s^2 for z-axis before Event B (Fig. **F41A**). After the event, the amplitudes are 26 m/s^2 for x-axis, 19 m/s^2 for y-axis, and 34 m/s^2 for z-axis (Fig. **F41B**). Event C is characterized by high PSD at a frequency of 0.1–10 Hz at ~0905 h on 19 August. The map location of Event C (33°15.5078′N, 136°37.5752′E) is also indicated in Figure **F43.** In the second dummy run test, acceleration and tilt data were collected from 0746 to 2226 h on 20 August. The data indicate a problem with the accelerometer-tiltmeter data after 1625 h on 20 August (Fig. **F42B**), with no acceleration and tilt data collected during the reentry.

Tilt data from the first and second dummy run tests are characterized by a lower frequency than the acceleration data (e.g., Fig. **F41**). This may not fully represent the exact tilt of the instrument carrier during testing because of the limited dynamic range of the bubble-type tilt sensor under strong vibration.

Temperature data

One MTL was set inside the pup joints at the bottom part of the sensor tree and eight were attached to the instrument carrier in the first dummy run test (see **"Observatory"** and Table **T21** in the "Methods" chapter). Temperature data were recovered from six sensors (see Table **T21** in the "Methods" chapter). No temperature data from inside the borehole are available, as the first dummy run test was aborted before reentry. Figure **F44** shows water temperature results from the dummy run. High-frequency temperature variations between 2.32° and 2.44°C are observed at 1700 m DRF (Fig. **F44B**). This variation does not directly correspond to the ship's motion.

Further modifications for future installments

Modifications of sensors and equipment are needed to overcome strong VIV for future installations under high sea current conditions. Vibration tests are also needed to evaluate sensor performance before the planned installation of long-term observatories.

Temporary monitoring system

Instrument preparation

A small instrument package designed to monitor pore pressure and temperature attached to the bottom (i.e., downward-looking) end of a mechanically set retrievable packer at Site C0010 represents an assembly hereafter referred to as the smart plug. Two instruments (8A and 82) (see **"Observatory"** in the "Methods" chapter) were shipped for Expedition 319 and were recording data during shipment from 12 April 2009 for test purposes so that during the expedition these data could be downloaded and checked for quality and overall performance of the pressure transducers and loggers. Additional status checks were successfully performed on board the *Chikyu* between 5 and 11 August before the pore pressure data logger memory was cleared and the instrument was "deployed" (i.e., was set to start recording) at 1459:20 h on 11 August. In parallel, the self-contained MTL was not reprogrammed and continued logging from its initial programming on 12 April 2009. Data logging includes pore pressure as well as three separate temperature readings (one in each pressure transducer for compensation and a separate platinum chip thermistor set for 60 s intervals, plus the self-contained MTL for Unit 8A set for 30 min logging intervals; see **"Observatory"** in the "Methods" chapter).

After programming the data loggers, the bottom end cap of each smart plug was greased and carefully closed, and the lower pore pressure tubing designed to monitor formation pressure was mounted and secured (Fig. **F45A**). Instrument 8A was chosen for deployment at Site C0010, and Instrument 82 was kept for backup. Given the experience with the observatory dummy run, in which strong ocean currents imparted dynamic force onto the drill string and the attached instruments (see above), we secured all 16 bolts holding the upper ("packer coupler") and lower ("bullnose") (Fig. **F45A**) end caps of smart plug Instrument 8A using a threadlock compound (Fig. **F45B**). The instrument was then coated with white paint to facilitate recognition during ROV-aided reentry of the borehole.

Installation

The smart plug instruments built for Expedition 319 were designed for deployment immediately beneath a Baker-Hughes A3 Lok-Set retrievable casing packer seal, as illustrated in Figure **F46.** In this configuration, the smart plug terminated the drill string and was first threaded onto the bridge plug. To ensure that the instrument did not detach during running through the Kuroshio Current, it was tack-welded at the crossover connection (Fig. **F47**). The smart plug assembly (Fig. **F48**) was then lowered into the water in a low-current area 10 nmi from Site C0010, where current speed was only 1.5 kt. Once the drill string depth was 1000 m DRF, the *Chikyu* slowly approached Site C0010 by drifting with the current, the ROV was deployed for reentry, and the drill pipe was lowered until the instrument package was near the seafloor. Reentry of the hole with the smart plug was successfully carried out at 0404 h on 23 August, and deployment was completed by setting the packer (with the instrument package below) at 365 m DSF at 0800 h on 23 August. The drill string was then detached from the retrievable packer by counter-clockwise rotation, and the drill string was pulled out of the hole at 0913 h (see **"Operations"**).

The instrument and screen placement were designed for the smart plug to provide a time series of fluid pressure and temperature in an isolated interval of formation including the splay fault (downward-looking pressure tube protruding from bullnose; Fig. **F45A**) and also monitor hydrostatic pressure as a reference (upward-looking pressure tube) (see also Fig. **F46**). Retrieval of the smart bridge plug is anticipated for 2010 or 2011, when a more sophisticated long-term monitoring system will be deployed at Site C0010.

Discussion and conclusions

Architecture and along-strike variation of the megasplay fault

Although we drilled Site C0010 with only a limited suite of LWD/MWD tools, the resistivity and gamma ray data sets provide a useful basis for comparison with nearby Site C0004, located ~3.5 km along strike to the northeast. Based on the two penetrations of the thrust wedge, along with observations from 3-D seismic reflection data, it is clear that the character and physical properties of the megasplay fault system vary considerably along strike.

At Site C0010, both gamma ray and resistivity values are higher in the thrust wedge than in the slope sediment above and below (Figs. **F5**, **F7**, **F28**, **F29**). In contrast, at Site C0004, gamma ray values and resistivity within the thrust wedge are only very slightly higher than in the overlying and underlying units and are considerably lower than in the thrust wedge at Site C0010 (Kinoshita et al., 2008). Both gamma ray and resistivity logs are also characterized by large variations in the thrust wedge at Site C0010 that are not observed at Site C0004. The values for the minima in gamma ray and resistivity at Site C0010 are similar to those for the entire thrust wedge at Site C0004.

The base of the thrust wedge at Site C0010 is marked by a negative polarity seismic reflection (impedance decreases across the boundary). In contrast, the base of the thrust wedge at Site C0004 is marked by a positive polarity reflection consistent with an increase in impedance expected based on observed *P*-wave velocity and bulk density from LWD and core data (Kinoshita et al., 2008; Kimura et al., 2008). The thrust wedge in the vicinity of Site C0004 is seismically transparent in character, whereas at Site C0010 there are several reflectors that likely correlate with the variations in gamma ray and resistivity (Figs.

F30, F31, F32). From both LWD azimuthal resistivity images and seismic data, the base of the thrust wedge is sharper at Site C0010 than at Site C0004, where coring documented a ~50 m thick fault-bounded package. This is consistent with the observation that at Site C0010 the mean borehole breakout orientation changes abruptly by ~20°–30° across the base of the thrust wedge (Fig. F16), whereas at Site C0004 the change is more gradual.

We interpret the higher gamma ray values and resistivity in the thrust wedge at Site C0010 to reflect increased compaction relative to the sediment above and below and relative to the thrust wedge at Site C0004, although it is also possible that these data could reflect a higher clay content. In the latter case, resistivity would be higher because of increased tortuosity associated with fine grain size and surface area. Similarly, the fluctuations in gamma ray and resistivity in the thrust wedge at Site C0004 could reflect variations in porosity or fracture density (with lower values associated with zones of increased fracturing or lower porosity), compositional layering, or a combination of the two.

The negative polarity reflection at the base of the thrust wedge at Site C0010 also suggests that the wedge has a lower porosity than the overridden slope sediments below. At Site C0010, the compaction trend for the slope sediments above and below the thrust wedge (inferred from resistivity data; Conin et al., 2008) suggests that the overridden slope sediments are not underconsolidated, as might be the case for compaction disequilibrium (Hart et al., 1995; Saffer, 2003). Thus, we conclude that the thrust wedge at Site C0010 is overcompacted, meaning that its porosity is anomalously low for its present burial depth (Fig. F22). This could result from increased mean effective stresses in the thrust wedge or uplift of the wedge along the megasplay from greater depth. In contrast, at Site C0004, the thrust wedge exhibits porosity similar to the slope sediments and no evidence for enhanced compaction. Downdip from Site C0004, the seismic reflection polarity at the base of the thrust wedge becomes negative, most likely indicating increased compaction of the thrust wedge relative to the footwall.

Taken together, these observations suggest that in the area of Site C0010 the thrust wedge comprises an overconsolidated package that probably originated at greater depth than the thrust wedge sampled at Site C0004. In contrast, the wedge at Site C0004 may be composed of reworked and deformed slope deposits that have never been deeply buried. This interpretation is also consistent with the location of Site C0010 on the flank of a lateral ramp on the megasplay fault (Fig. F30).

Observatory installations

Dummy run

The dummy run test in Hole C0010A successfully evaluated a subset of planned operations for future permanent borehole observatory installation. The planned permanent observatory consists of three major parts: bottom-hole instruments, tubing to support downhole cables and hydraulic lines, and the circulation obviation retrofit kit (CORK) head, which suspends everything below and seals the hole. In this test, we confirmed procedures to make up the bottom-hole instruments and lower them into the water. There was concern that the weak surface of the strainmeter might hit the guide funnel below the rotary table as the tubing below the strainmeter drifted in the ocean current, but by experimenting and adjusting the length of tubing prior to assembly we were able to find the optimum length to operate safely. We found that the bottom-hole instrument string was subjected to significant vibration from the drill string when the *Chikyu* drifted for reentry into the hole because of the Kuroshio Current. Before the experiment, vibration on the drill string was suggested but not emphasized as a major concern. Structurally, the tubing and instrument string were much weaker than the drill pipes; therefore, vibration was amplified in these weak sections through resonance. The effects were sufficiently severe that the delicate internal workings of the instruments (such as hinges and pivots in the seismometers) would not survive to record data after installation in the hole. Modifications to the design of the instrument carrier are thus required to ensure it maintains integrity during installation. In addition, we have not tested the complete instrument string, which will have the CORK head and 500 m (or more) of tubing attached with soft cables and hydraulic lines. The experience during Expedition 319 also highlights the need for more complete evaluation of overall observatory design and installation. Evaluation and treatment are necessary to address (1) sensor integrity under vibration, (2) resonance effects from drill string vibration, (3) tolerance of the downhole cable and hydraulic lines to stress and vibration, and (4) the ability of other components, such as swellable packers and CORK head, to withstand the vibration. Acceleration data from the dummy run test in this expedition are valuable for such evaluations.

There are also other options for installing long-term observatories. The smart plug installed during this expedition is an encouraging option for intermediate- to long-term borehole observatory emplacement. An extended version of the smart plug that includes a seismic component may also be an option. In such a system, continuous seismic observations for a period of 2 y, in conjunction with pressure and temperature observation, would be possible. We still have to evaluate effects of the vibration on seismometers and pressure gauges because the smart plug is, as with the bottom-hole instrument string for the dummy run test, also deployed by drill pipe, and thus subject to vibration in the current.

As another option, by separately lowering the sensor into the hole after lowering the observatory to the seafloor, it may be possible to reduce effects from the current-induced vibration while lowering the observatory to the seafloor. An observatory package that houses a bottom-hole sensor and downhole cable wound in a winch would be landed on the reentry funnel of the borehole without severe vibration or stress on sensors and cables. The sensors could then be lowered to the bottom of the hole by wireline. Such an observation system was developed for logging (Amitani et al., 2002) but has not been deployed in boreholes. Installation of a cabled borehole sensor into a borehole via a controlled wireline has also been tested (Stephen et al., 2003). In this case, the cable that would be in the borehole is lowered beneath the ship before reentry. In these cases, there are risks of damage to the borehole cable caused by the ship's heave while the cable is being lowered into the borehole.

Temporary monitoring system

After LWD, casing, and the dummy run test at Site C0010, we suspended the hole by installing a smart plug sensor package attached beneath a retrievable casing packer (Figs. **F45, F46, F47, F48**). The smart plug is a robust retrievable stand-alone instrument package designed with a relatively short lead-time, in order to make use of suspended boreholes prior to final observatory installation. Although it is relatively simple, the smart plug at Site C0010 represents the first long-term monitoring in the NanTroSEIZE project and the first observatory element installed by the *Chikyu*. If successful, it will provide another tool for long-term hydrologic and/or thermal monitoring in scientific ocean boreholes.

For installation at Site C0010, the retrievable casing packer was placed above two screened casing joints that provide hydraulic communication with the megasplay fault zone (Fig. **F45**). In this configuration, the smart plug will monitor pore pressure and temperature within the megasplay fault and also record the hydrostatic pressure open to the overlying ocean as a reference (Fig. **F45;** see also Fig. **F28** in the "Methods" chapter). Hole completion relies on cement at the base of the casing shoe and in the annulus (a planned top of cement at ~40 m above the casing shoe) and on the collapse of soft sediment and thrust wedge material against the casing over the ~400 m of annulus above the screens to achieve hydraulic isolation from the sediments above and below, respectively. Upon recovery of the instruments (anticipated for Site C0010 in 2010 or 2011), we will assess the efficacy of hydraulic isolation by comparison of the fault zone and hydrostatic pore pressure time series and the response of the fault zone pore pressure to tidal loading (e.g., Wang and Davis, 1996). We also anticipate conducting a cement-bond log as part of future operations to define the top of cement and evaluate the extent of formation collapse against the casing above the screens.

Despite strong ocean currents (up to 4.5 kt and persisting to a depth of several hundred meters below sea level), the smart plug was successfully run to the wellhead and set inside the casing. However, even for installation of this relatively simple and short sensor package, we encountered problems associated with the Kuroshio Current; upon running the drill pipe to the surface, the running tool sheared off from the drill pipe at a 3½ inch tubing connection, presumably as a result of vibration in the water column. One key difference between the smart plug and many previous hydrologic observatory installations in Ocean Drilling Program (ODP) (e.g., Becker and Davis, 2005) is that data cannot be downloaded from the sensor package until it is retrieved with the packer using a drillship. Thus, we cannot assess whether damage to the electronics or pressure sensors was sustained during running to the wellhead or hole reentry prior to instrument recovery.

References

Amitani, Y., Kyo, M., Hashimoto, K., Shimura, T., and Sawa, T., 2002. Borehole Reentry System "BENKEI." *Proc. Int. Offshore Polar Eng. Conf.,* 12:116–121.

Araki, E., Byrne, T., McNeill, L., Saffer, D., Eguchi, N., Takahashi, K., and Toczko, S., 2009. NanTroSEIZE Stage 2: NanTroSEIZE riser/riserless observatory. *IODP Sci. Prosp.,* 319. **doi:10.2204/iodp.sp.319.2009**

Archie, G.E., 1942. The electrical resistivity log as an aid in determining some reservoir characteristics. *J. Pet. Technol.,* 5:1–8.

Athy, L.F., 1930. Density, porosity, and compaction of sedimentary rocks. *AAPG Bull.,* 14(1):1–24.

Barton, C.E., and Zoback, M.D., 1994. Stress perturbations associated with active faults penetrated by boreholes: possible evidence for near-complete stress drop and a new technique for stress magnitude measurement. *J. Geophys. Res.,* 99(B5):9373–9390. **doi:10.1029/93JB03359**

Becker, K., and Davis, E.E., 2005. A review of CORK designs and operations during the Ocean Drilling Program. *In* Fisher, A.T., Urabe, T., Klaus, A., and the Expedition 301 Scientists, *Proc. IODP,* 301: College Station, TX (Integrated Ocean Drilling Program Management International, Inc.). **doi:10.2204/iodp.proc.301.104.2005**

Conin, M., Bourlange, S., Henry, P., and the IODP Expedition 314/315/316 Scientific Party, 2008. Interpretation of LWD resistivity from Nankai accretionary wedge in the light of clay physico-chemical properties. *Eos, Trans. Am. Geophys. Union,* 89(53)(Suppl.):T31B–1999. (Abstract) **http://www.agu.org/meetings/fm08/waisfm08.html**

Expedition 314 Scientists, 2009a. Expedition 314 Site C0003. *In* Kinoshita, M., Tobin, H., Ashi, J., Kimura, G., Lallemant, S., Screaton, E.J., Curewitz, D., Masago, H., Moe, K.T., and the Expedition 314/315/316 Scientists, *Proc. IODP,* 314/315/316: Washington, DC (Integrated Ocean Drilling Program Management International, Inc.). **doi:10.2204/iodp.proc.314315316.115.2009**

Expedition 314 Scientists, 2009b. Expedition 314 Site C0004. *In* Kinoshita, M., Tobin, H., Ashi, J., Kimura, G., Lallemant, S., Screaton, E.J., Curewitz, D., Masago, H., Moe, K.T., and the Expedition 314/315/316 Scientists, *Proc. IODP,* 314/315/316: Washington, DC (Integrated Ocean Drilling Program Management International, Inc.). **doi:10.2204/iodp.proc.314315316.116.2009**

Expedition 316 Scientists, 2009. Expedition 316 Site C0004. *In* Kinoshita, M., Tobin, H., Ashi, J., Kimura, G., Lallemant, S., Screaton, E.J., Curewitz, D., Masago, H., Moe, K.T., and the Expedition 314/315/316 Scientists, *Proc. IODP,* 314/315/316: Washington, DC (Integrated Ocean Drilling Program Management International, Inc.). **doi:10.2204/iodp.proc.314315316.133.2009**

Hart, B.S., Flemings, P.B., and Deshpande, A., 1995. Porosity and pressure: role of compaction disequilibrium in the development of geopressures in a Gulf Coast Pleistocene basin. *Geology,* 23(1):45–48. **doi:10.1130/0091-7613(1995)023<0045:PAPROC>2.3.CO;2**

Heki, K., 2007. Secular, transient and seasonal crustal movements in Japan from a dense GPS array: implication for plate dynamics in convergent boundaries. *In* Dixon, T., and Moore, C. (Eds.), *The Seismogenic Zone of Subduction Thrust Faults:* New York (Columbia Univ. Press), 512–539.

Kimura, G., Screaton, E.J., Curewitz, D., and the Expedition 316 Scientists, 2008. NanTroSEIZE Stage 1A: NanTroSEIZE shallow megasplay and frontal thrusts. *IODP Prel. Rept.,* 316. **doi:10.2204/iodp.pr.316.2008**

Kinoshita, M., Tobin, H., Ashi, J., Kimura, G., Lallemant, S., Screaton, E.J., Curewitz, D., Masago, H., Moe, K.T., and the Expedition 314/315/316 Scientists, 2009. *Proc. IODP,* 314/315/316: Washington, DC (Integrated Ocean Drilling Program Management International, Inc.). **doi:10.2204/iodp.proc.314315316.2009**

Kinoshita, M., Tobin, H., Moe, K.T., and the Expedition 314 Scientists, 2008. NanTroSEIZE Stage 1A: NanTroSEIZE LWD transect. *IODP Prel. Rept.,* 314. **doi:10.2204/iodp.pr.314.2008**

Miyazaki, S., and Heki, K., 2001. Crustal velocity field of southwest Japan: subduction and arc-arc collision. *J. Geophys. Res.,* 106(B3):4305–4326. **doi:10.1029/2000JB900312**

Moore, G.F., Park, J.-O., Bangs, N.L., Gulick, S.P., Tobin, H.J., Nakamura, Y., Sato, S., Tsuji, T., Yoro, T., Tanaka, H., Uraki, S., Kido, Y., Sanada, Y., Kuramoto, S., and Taira, A., 2009. Structural and seismic stratigraphic framework of the NanTroSEIZE Stage 1 transect. *In* Kinoshita, M., Tobin, H., Ashi, J., Kimura, G., Lallemant, S., Screaton, E.J., Curewitz, D., Masago, H., Moe, K.T., and the Expedition 314/315/316 Scientists, *Proc. IODP,* 314/315/316: Washington, DC (Integrated Ocean Drilling Program Management International, Inc.). **doi:10.2204/iodp.proc.314315316.102.2009**

Saffer, D.M., 2003. Pore pressure development and progressive dewatering in underthrust sediments at the Costa Rican subduction margin: comparison with northern Barbados and Nankai. *J. Geophys. Res.,* 108(B5):2261–2276. **doi:10.1029/2002JB001787**

Seno, T., Stein, S., and Gripp, A.E., 1993. A model for the motion of the Philippine Sea plate consistent with NUVEL-1 and geological data. *J. Geophys. Res.,* 98(B10):17941–17948. **doi:10.1029/93JB00782**

Stephen, R.A., Spiess, F.N., Collins, J.A., Hildebrand, J.A., Orcutt, J.A., Peal, K.R., Vernon, F.L., and Wooding, F.B., 2003. Ocean seismic network pilot experiment. *Geochem., Geophys., Geosyst.,* 4(10):1092. **doi:10.1029/2002GC000485**

Tobin, H., Kinoshita, M., Ashi, J., Lallemant, S., Kimura, G., Screaton, E.J., Moe, K.T., Masago, H., Curewitz, D., and the Expedition 314/315/316 Scientists, 2009a. NanTroSEIZE Stage 1 expeditions: introduction and synthesis of key results. *In* Kinoshita, M., Tobin, H., Ashi, J., Kimura, G., Lallemant, S., Screaton, E.J., Curewitz, D., Masago, H., Moe, K.T., and the Expedition 314/315/316 Scientists, *Proc. IODP,* 314/315/316: Washington, DC (Integrated Ocean Drilling Program Management International, Inc.). **doi:10.2204/iodp.proc.314315316.101.2009**

Tobin, H., Kinoshita, M., Moe, K.T., and the Expedition 314 Scientists, 2009b. Expedition 314 summary. *In* Kinoshita, M., Tobin, H., Ashi, J., Kimura, G., Lallemant, S., Screaton, E.J., Curewitz, D., Masago, H., Moe, K.T., and the Expedition 314/315/316 Scientists, *Proc. IODP,* 314/315/316: Washington, DC (Integrated Ocean Drilling Program Management International, Inc.). **doi:10.2204/iodp.proc.314315316.111.2009**

Wang, K., and Davis, E.E., 1996. Theory for the propagation of tidally induced pore pressure variations in layered subseafloor formations. *J. Geophys. Res.,* 101(B5):11483–11495. **doi:10.1029/96JB00641**

Zoback, M.D., 2007. *Reservoir Geomechanics:* Cambridge (Cambridge Univ. Press).

Publication: 31 August 2010
MS 319-104

Figure F1. Detailed map of Site C0010 and proposed Site NT2-01K. In-line (IL) and cross-line (XL) seismic tracks are indicated. Sites drilled during previous NanTroSEIZE stages are also indicated.

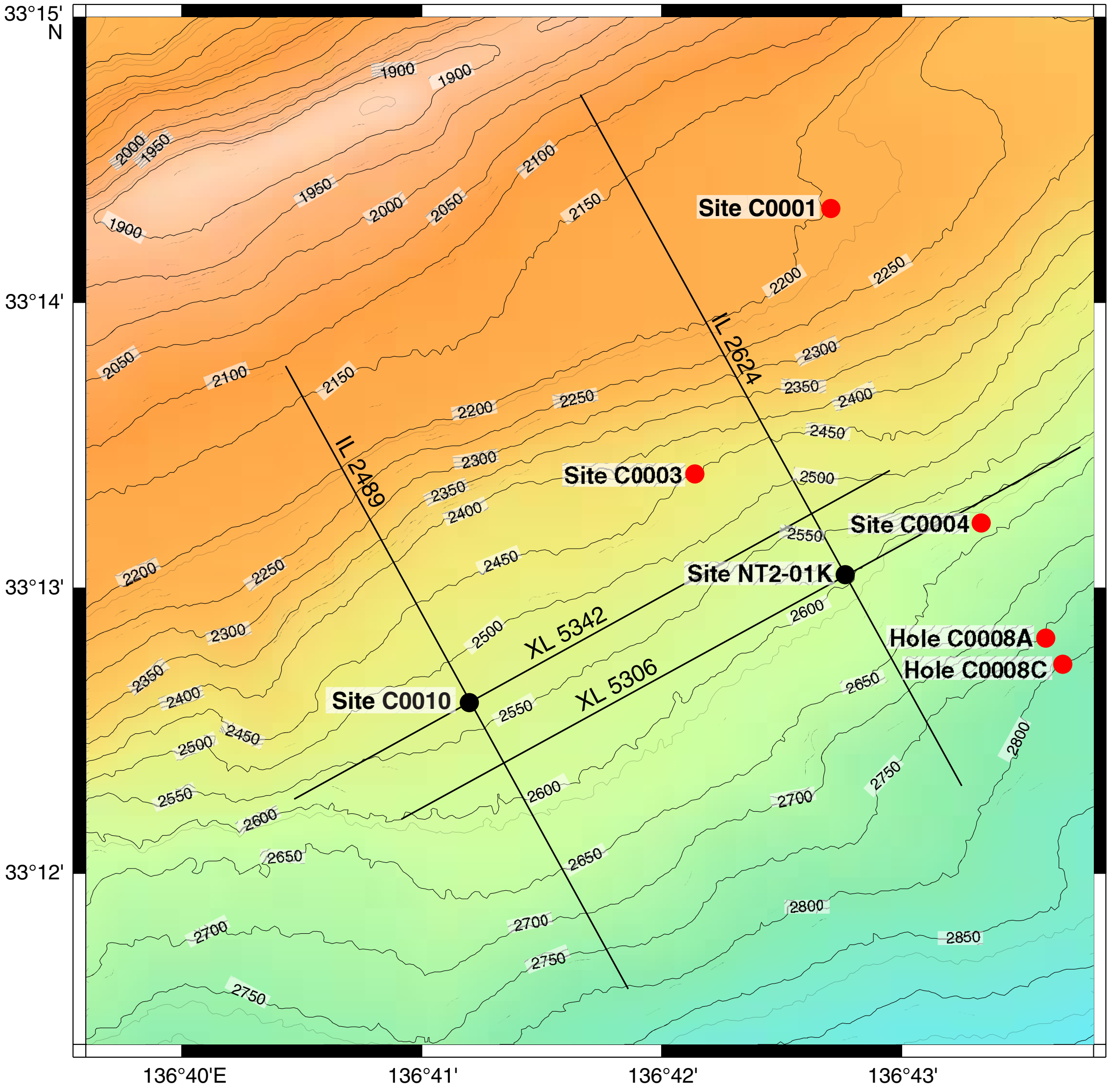

Figure F2. Seismic in-line (IL) and cross-line (XL) profiles of (**A**) Site C0010 and (**B**) proposed Site NT2-01K. VE = vertical exaggeration.

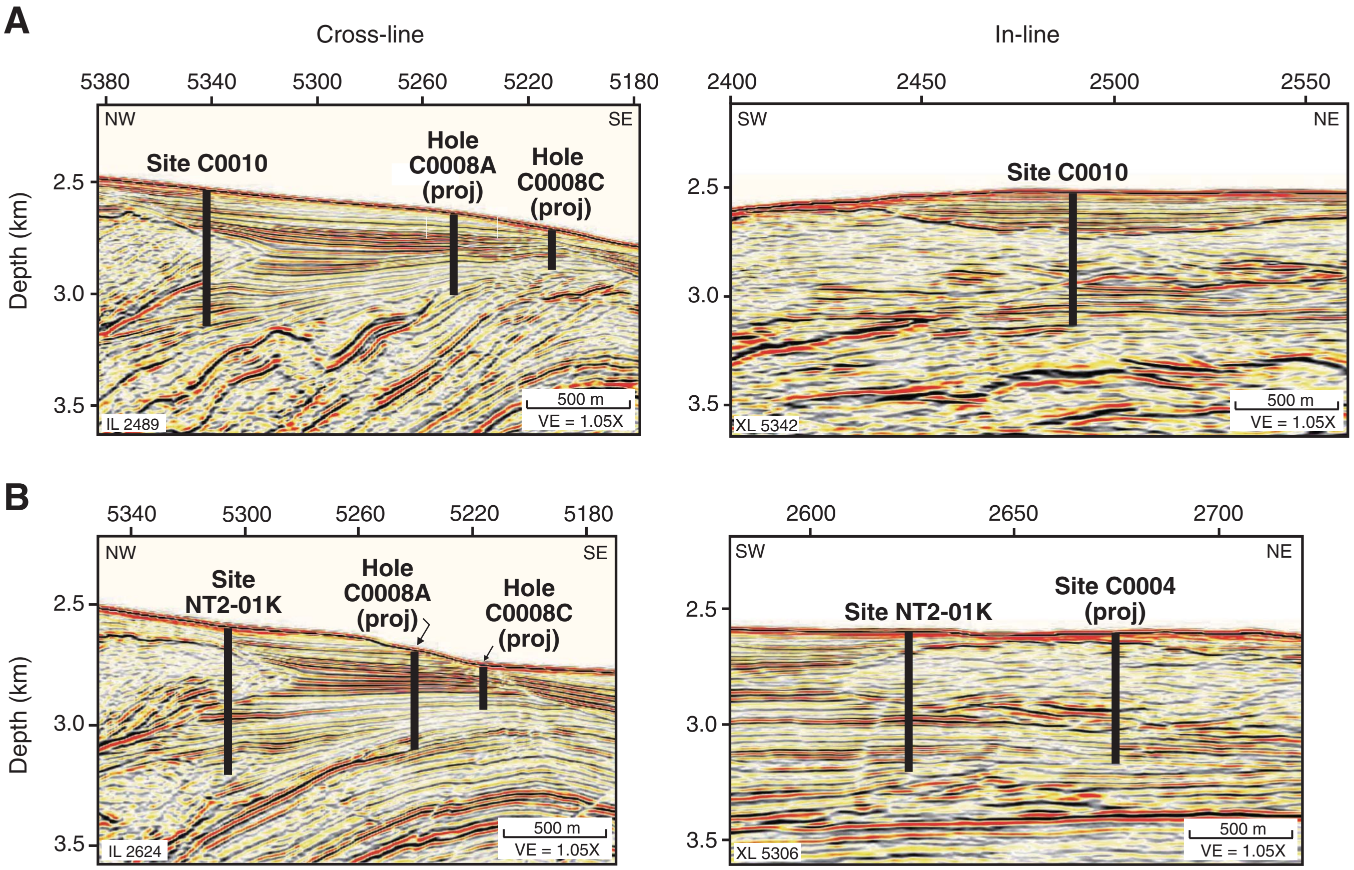

Figure F3. Schematic showing planned long-term observatory configuration. CORK = circulation obviation retrofit kit, ROV = remotely operated vehicle.

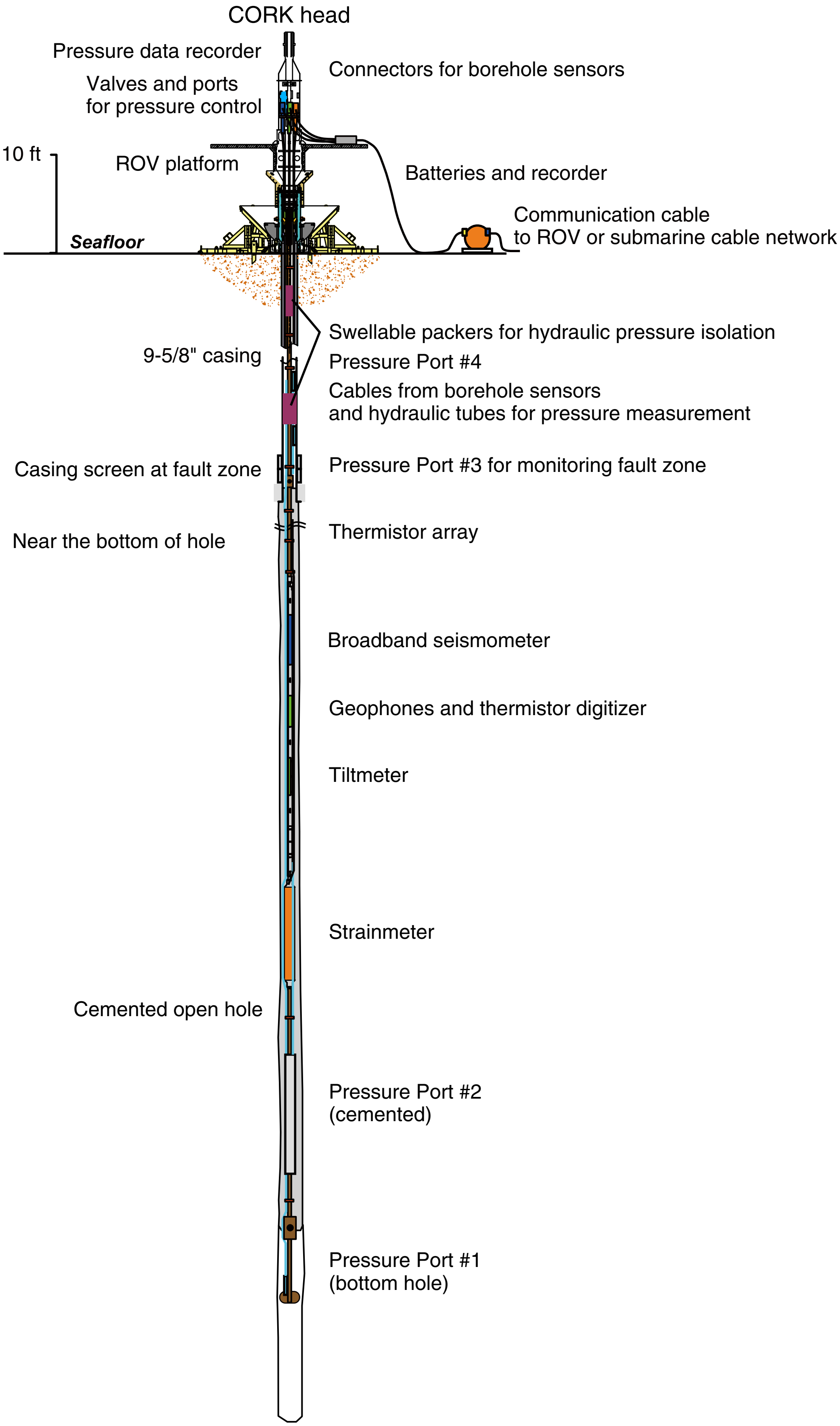

Figure F4. Depths of the bottom of casing, planned cement top, and screen depth.

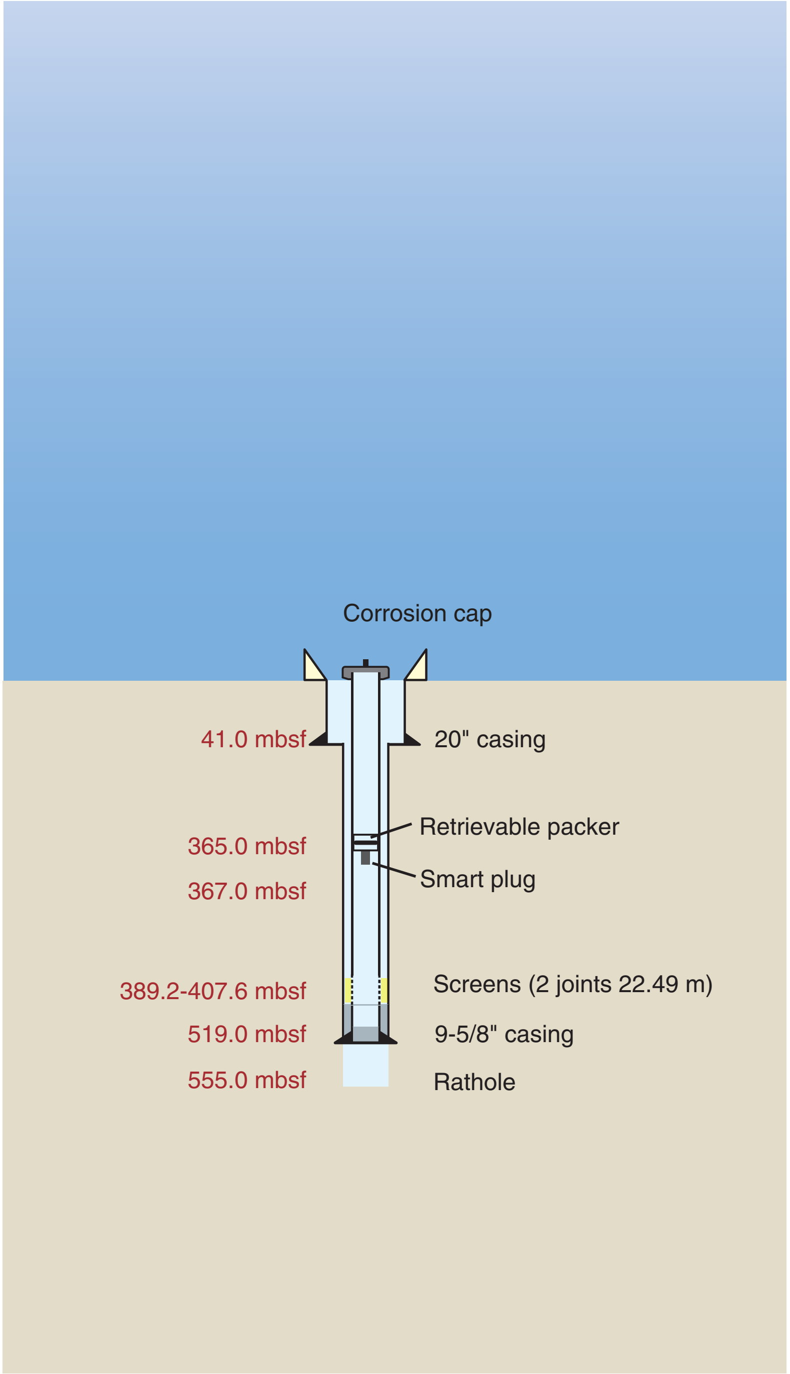

Figure F5. Composite MWD-GVR logs from Hole C0010A with their data quality indicators. From left to right: depths; logging run columns (blue = Run 1, red = Run 2); logging units; gamma ray; bit, ring, shallow, medium, and deep resistivities; rate of penetration (ROP) averaged over last 5 ft; stick-slip; rotation speed and data quality indicator columns for resistivity image and scalar logs. rpm = rotations per minute.

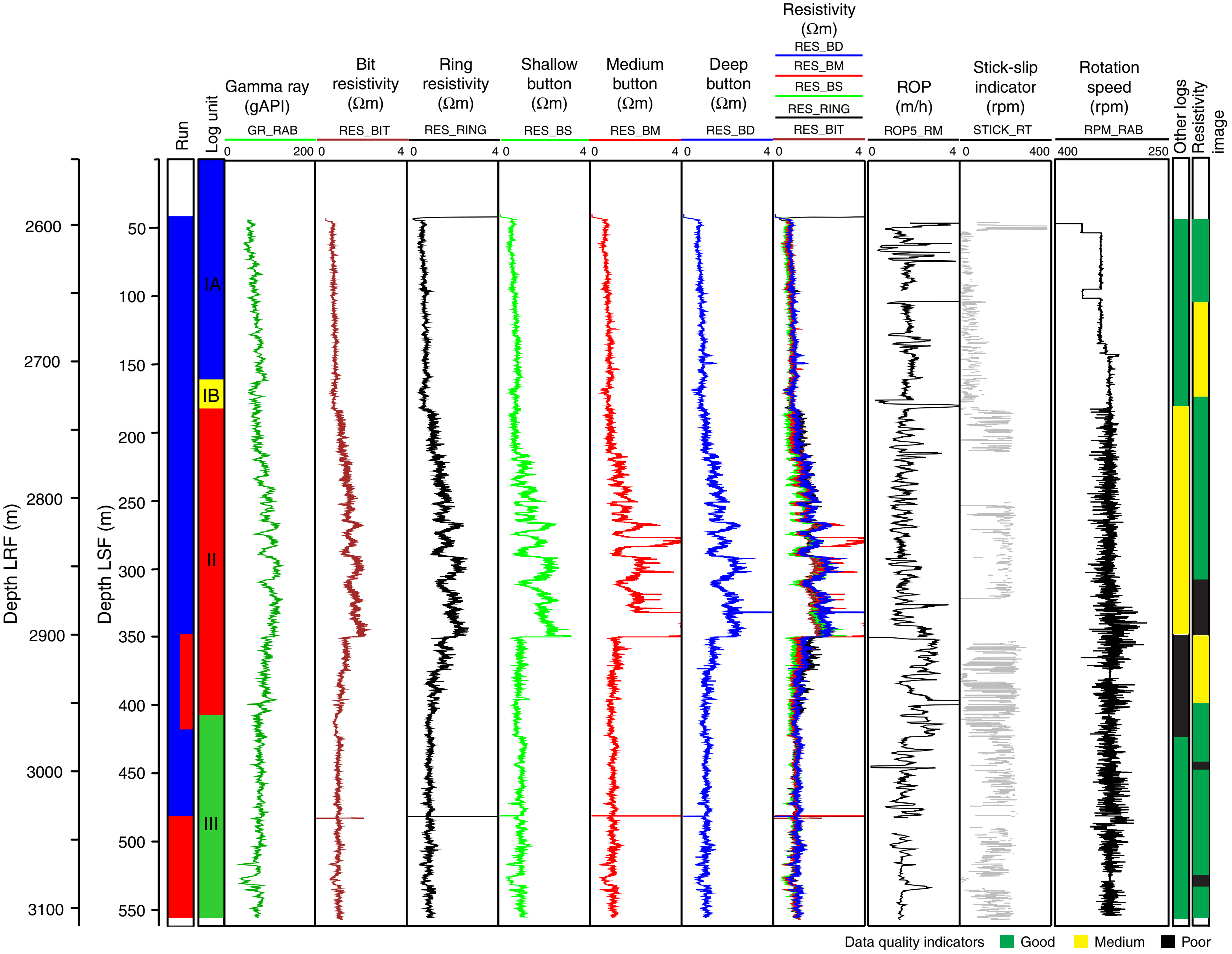

Figure F6. Diagram of reference depths and correlation between depth scales, Site C0010. TD = total depth. See **"Observatory"** for description of screens.

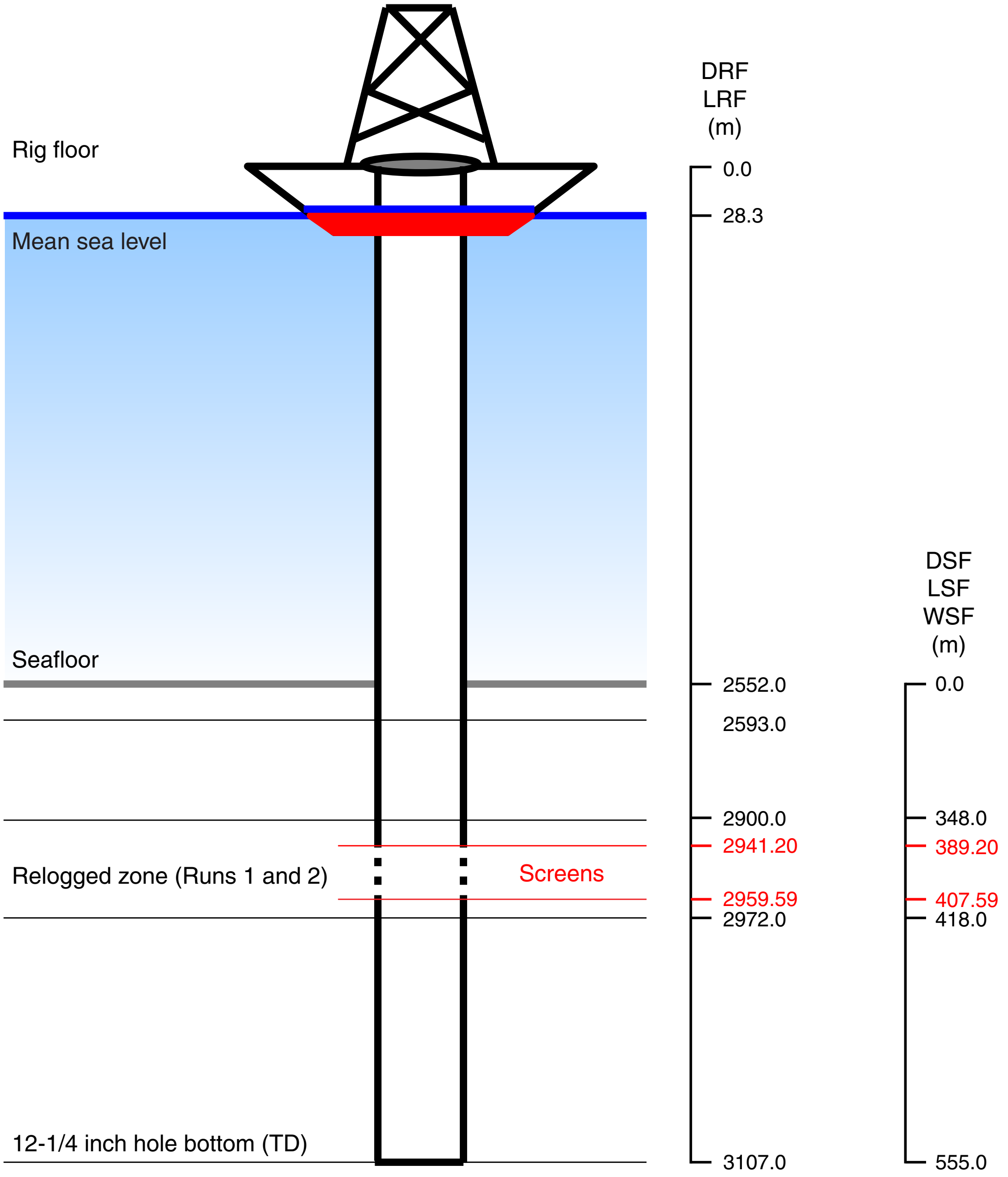

Figure F7. Gamma ray and bit resistivity measurements, Site C0010 (Runs 1 and 2). MWD = measurement while drilling.

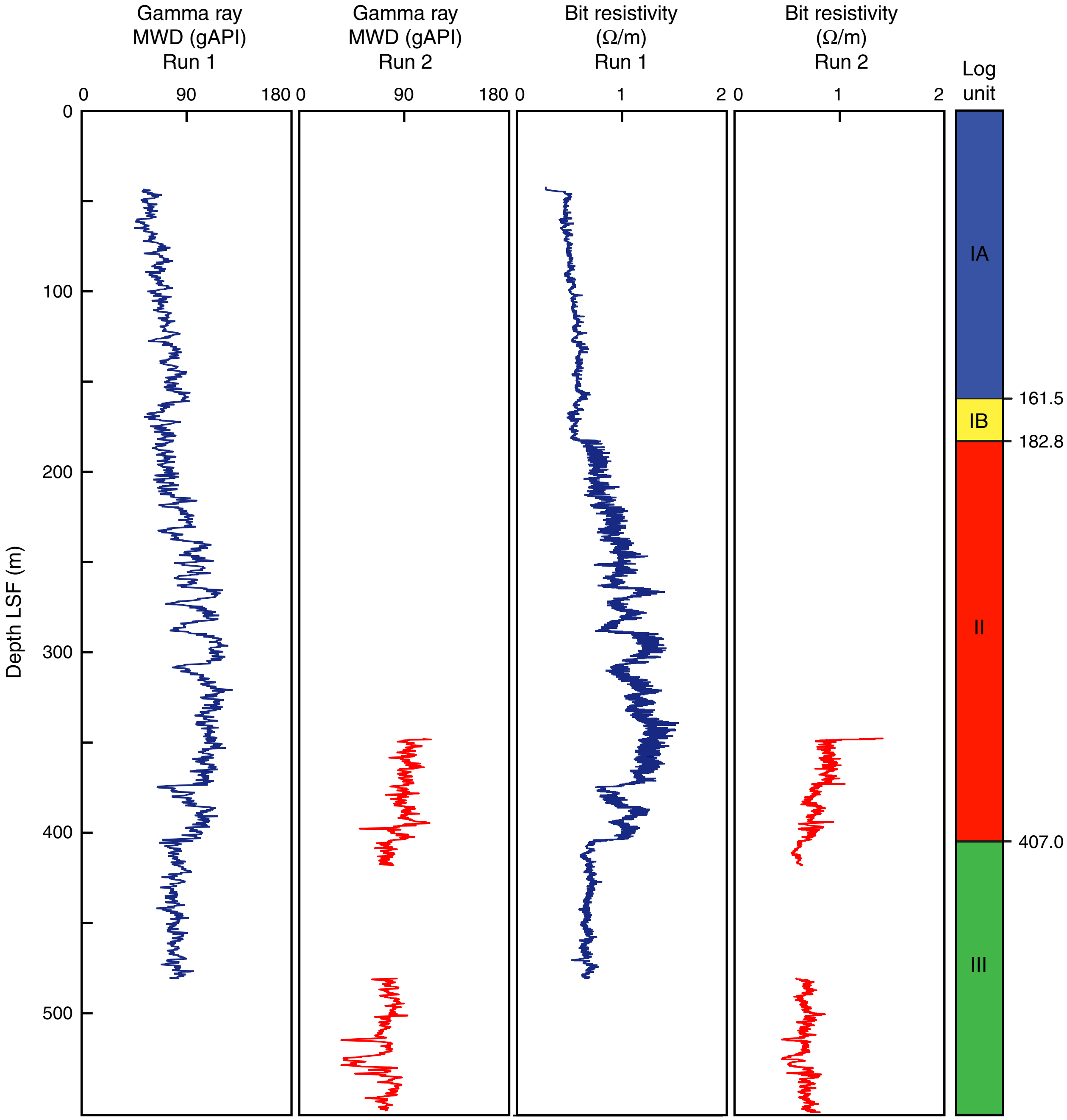

Figure F8. Gamma ray and bit resistivity measurements at Site C0010 (Runs 1 and 2) and correlation with units defined at Site C0004 (Expedition 314 Scientists, 2009b; Expedition 316 Scientists, 2009). Boundaries of lithologic units defined on cores in Expedition 316 Holes C0004C and C0004D were extended to log units from Expedition 314 Hole C0004B based on gamma ray values. Correlations between log units in Hole C0004B and at Site C0010 are also based on gamma ray values. cps = counts per second, MWD = measurement while drilling.

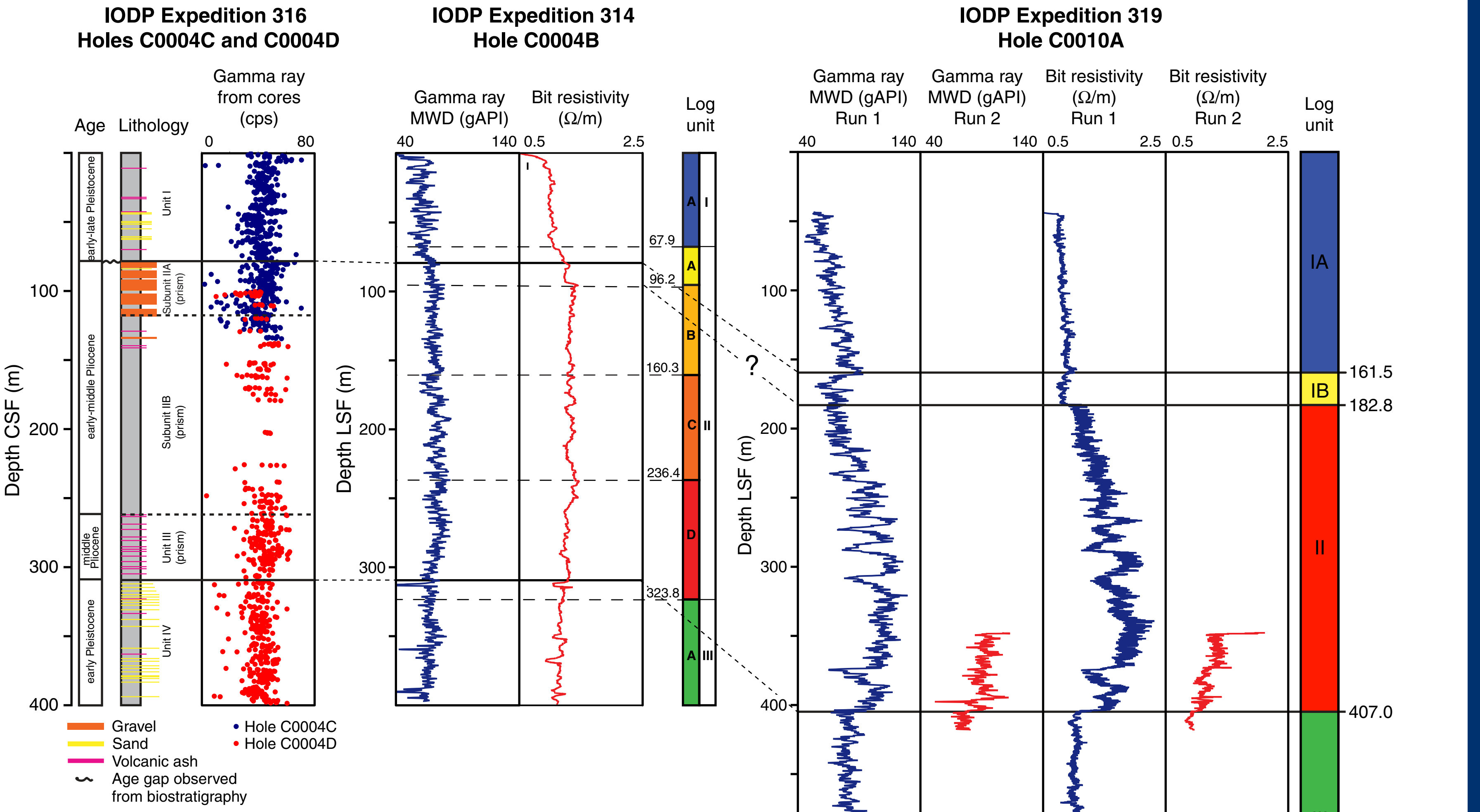

Lithology of units from descriptions of core (Holes C0004C and C0004D)

Unit I: slope sediments-hemipelagic nannofossil-rich mud with rare volcanic ashes and rare thin sands

Subunit IIA: prism-sedimentary breccias, hemipelagic mud (mass-wasting deposits)

Subunit IIB: prism-hemipelagic mud with rare turbidite sands and volcanic ashes

Unit III: fault-bounded package-hemipelagic mud with scattered volcanic ashes

Unit IV: underthrust slope sediments-hemipelagic mud with turbidite sand and rare volcanic ashes

Figure F9. Example of criteria for interpreting bedding from LWD geoVISION resistivity imaging data.

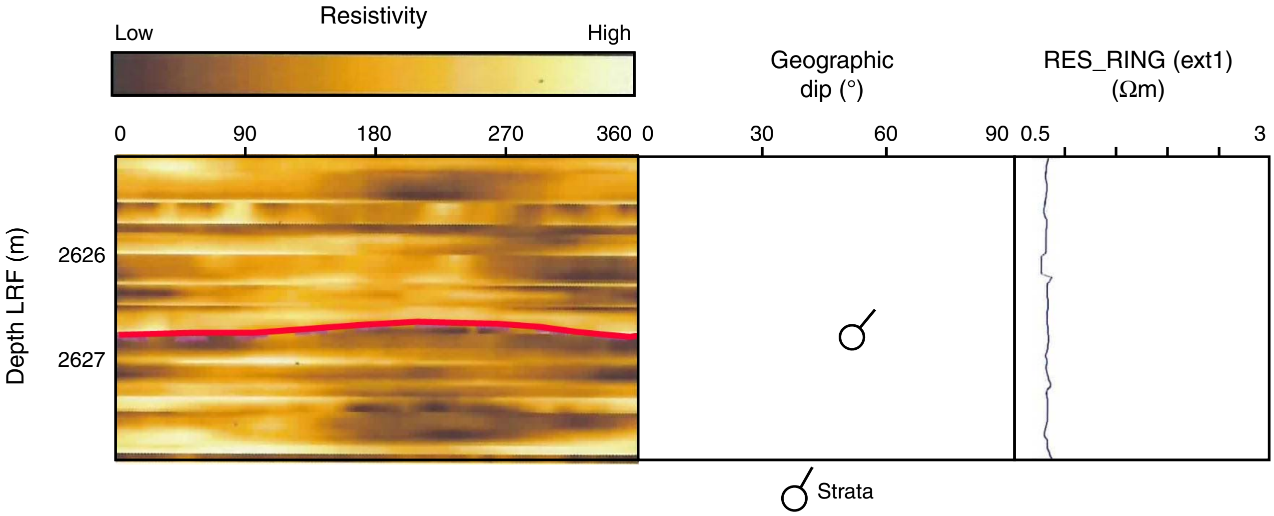

Figure F10. Example of criteria for interpreting faulting from LWD geoVISION resistivity imaging data showing a relatively resistive fault at the sine curve with distinctly different resistivity patterns on opposite sides of sine curve.

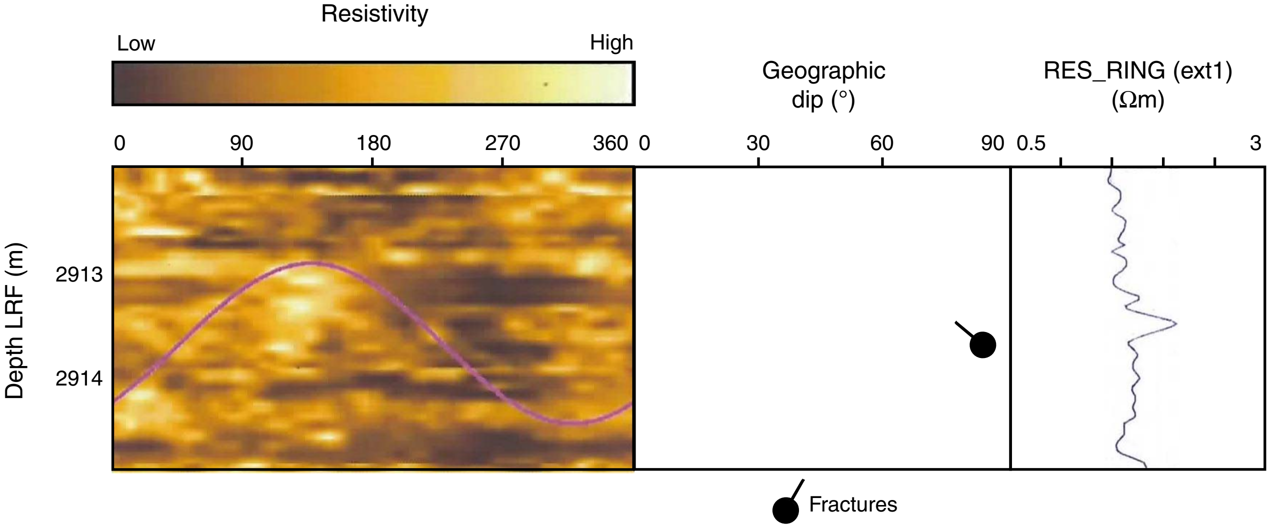

Figure F11. Summary of bedding attitudes. **A.** Contoured plot of poles to bedding for all bedding measurements. Dots = poles, lighter colors = concentrations of poles, white area = no poles. **B.** Rose diagram of dip directions for all bedding.

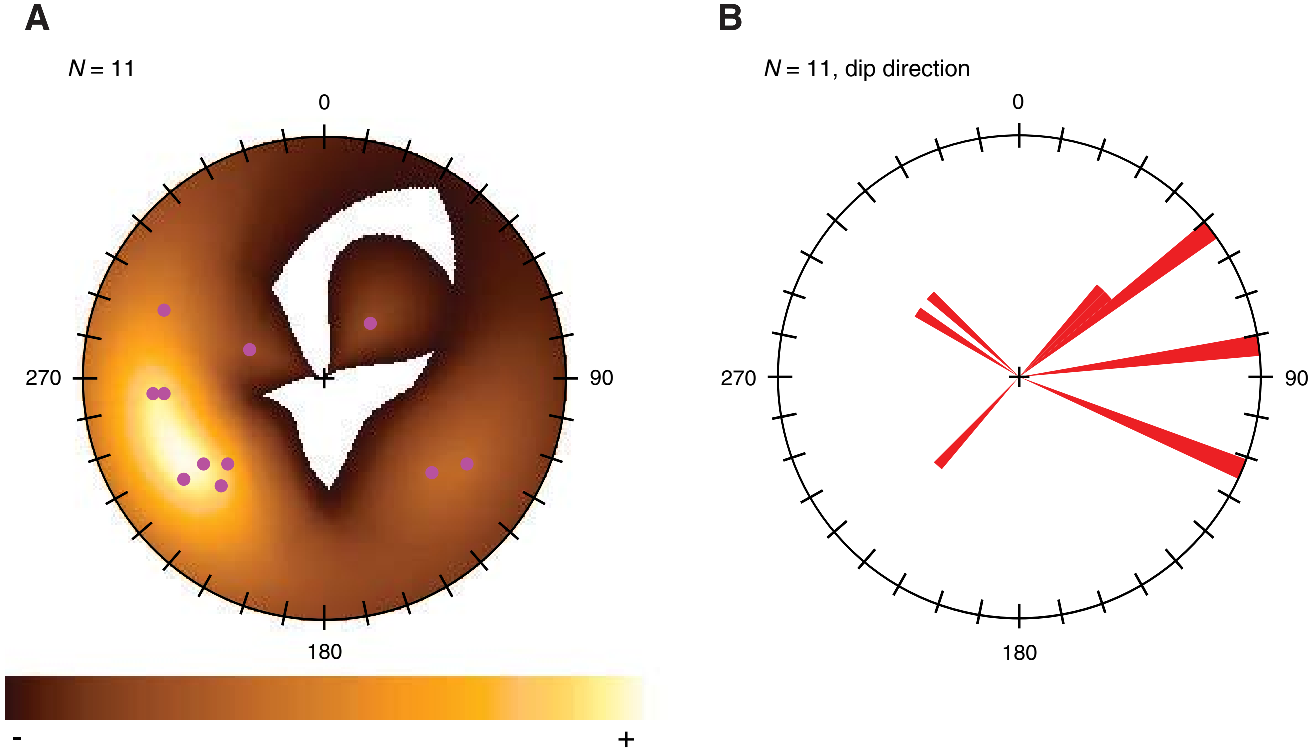

Figure F12. Tadpole plot of bedding and fault orientations versus depth, also showing ring resistivity log. Tadpoles show dip direction. Open circles = bedding, solid circles = faults. See C0010_T1.XLS and C0010_T2.XLS in STRUCGEOL in **"Supplementary material."** Faults from logging Run 1 from 347 to 418 m LSF are not included.

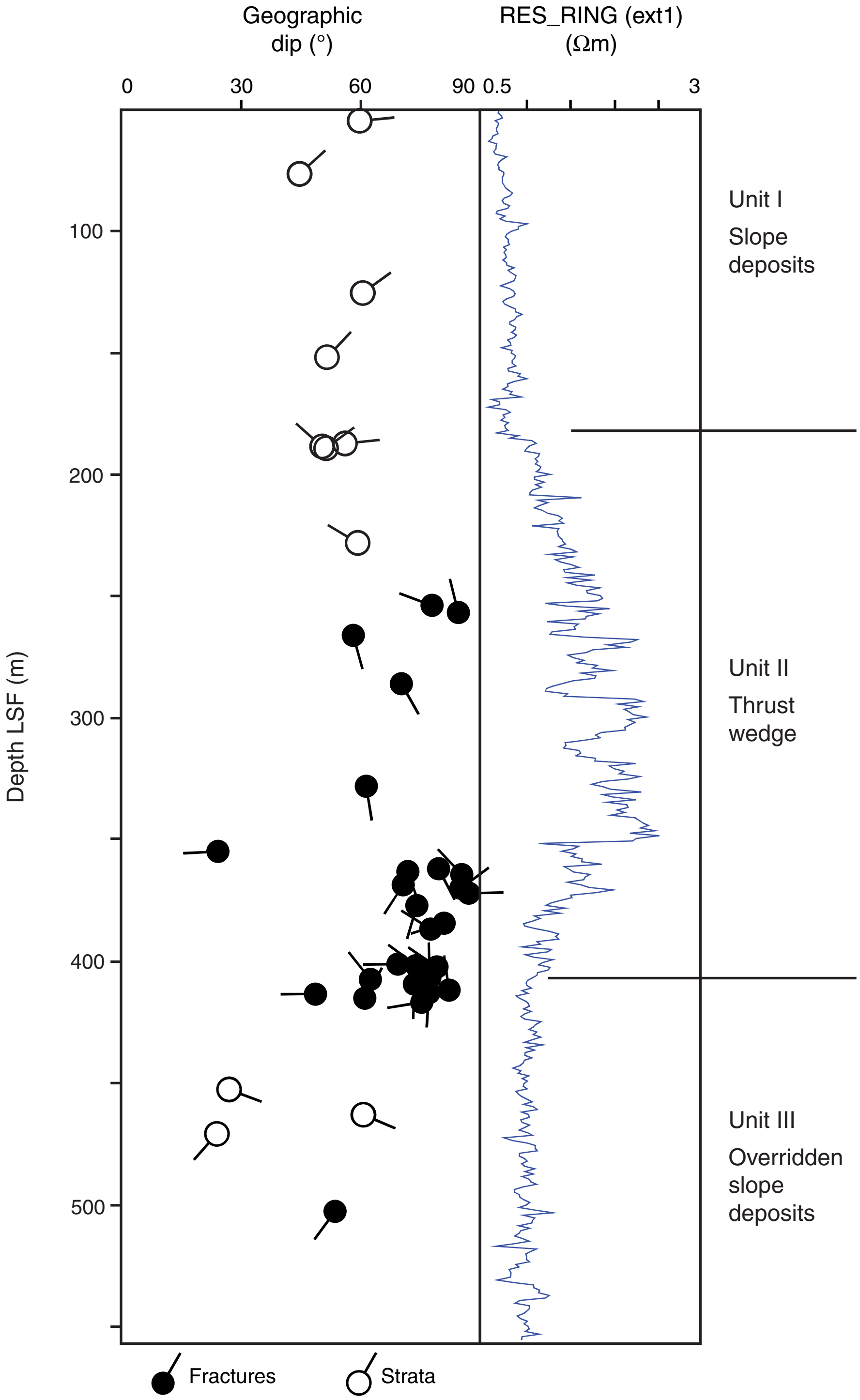

Figure F13. Summary of fault attitudes. **A.** Contoured plot of poles to faults for all fault measurements. Dots = poles, lighter colors = concentrations of poles, white areas = no poles. **B.** Rose diagram of dip directions for all faults. Faults most commonly dip west and south, but dip directions exhibit a wide range.

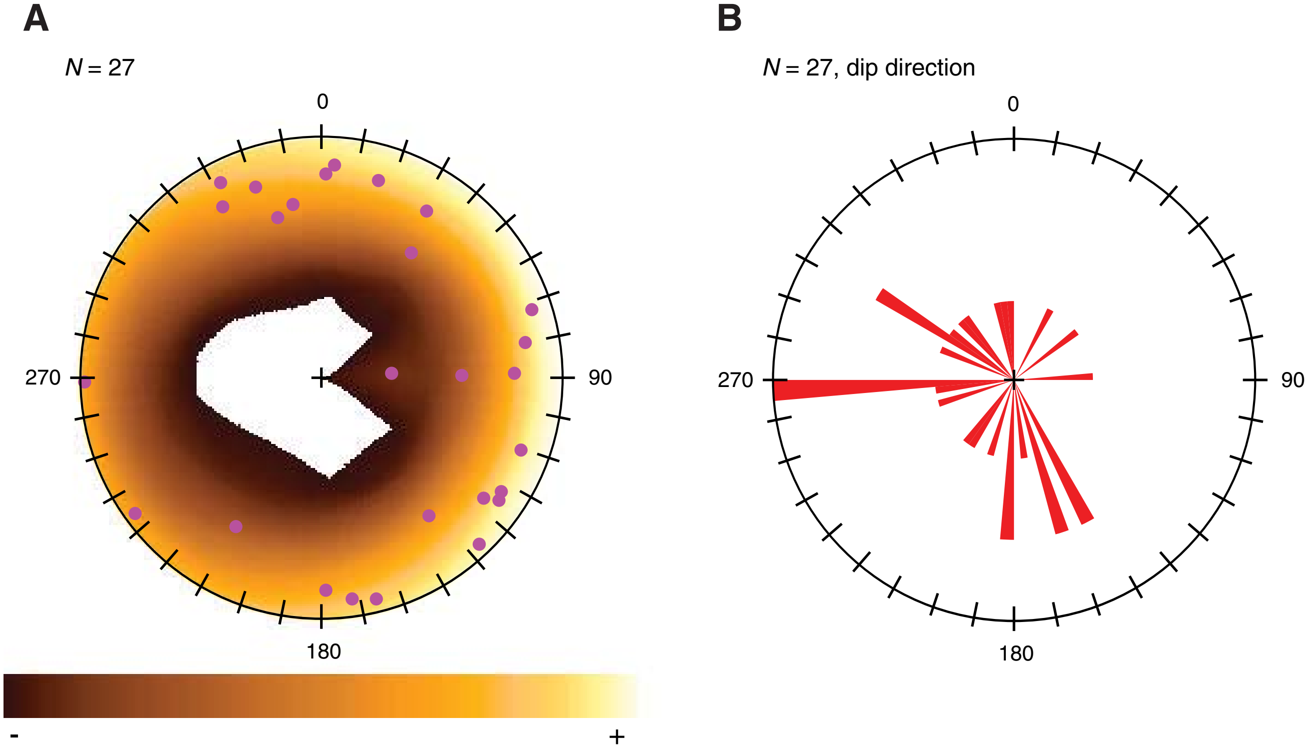

Figure F14. Comparison of resistivity image data interpreted from Runs 1 and 2 (relogging) from 348 to 418 m LSF. Data acquired while drilling (left) have heave-induced horizontal stripes 0.5–1 m thick, obscuring vertical resolution. Data gathered from Run 2 show better resolution. Tadpole plots show faults picked in each run. More faults were picked in Run 2 data, and dips are relatively steep. Fewer faults were picked in Run 1 data, and shallower dips are more common. Only three common faults were picked on both runs (see C0010_T2.XLS and C0010_T3.XLS in STRUCGEOL in **"Supplementary material"**).

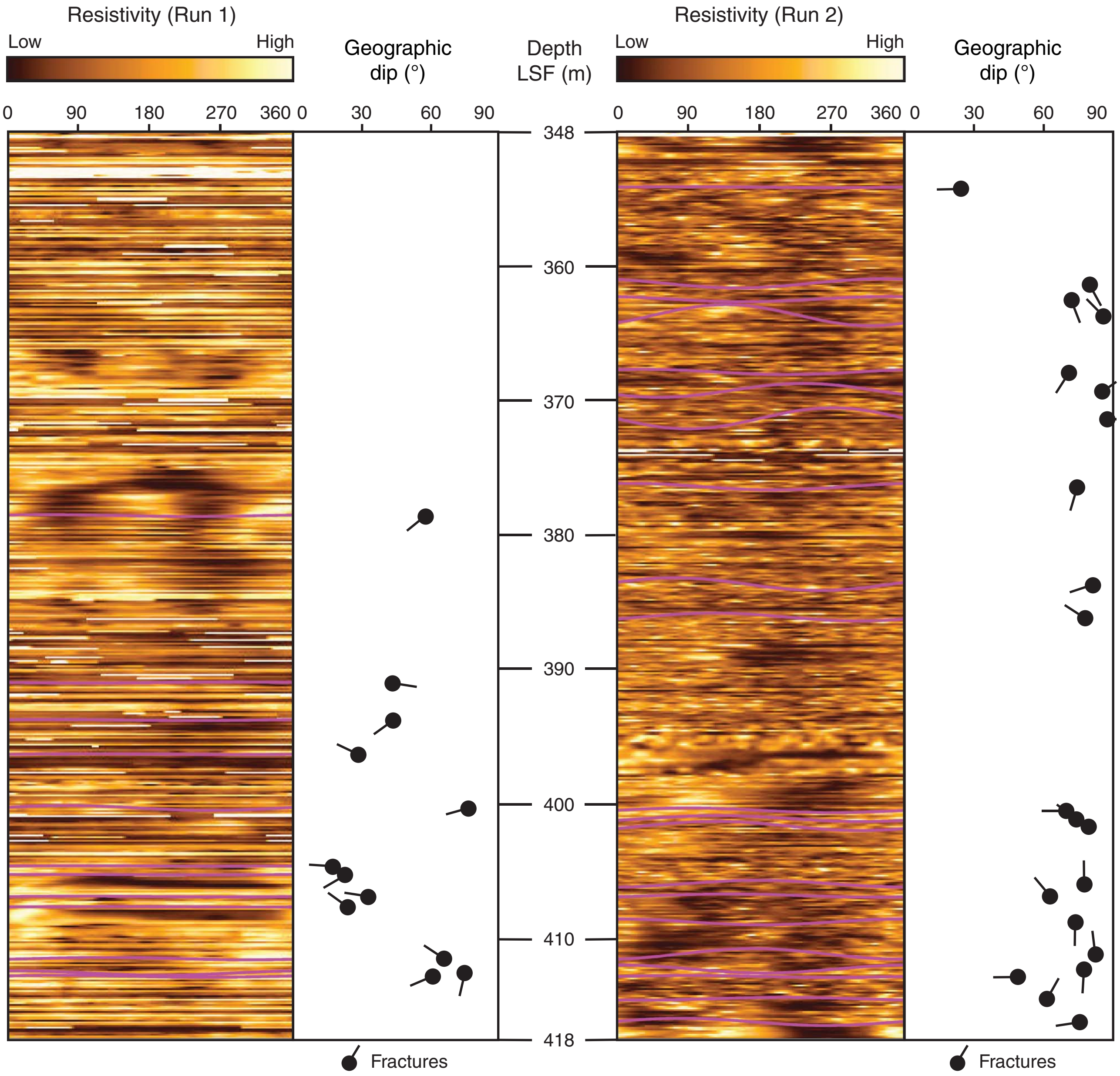

Figure F15. Comparison of resistivity images acquired on Runs 1 and 2 showing breakouts immediately below thrust wedge (lower boundary of thrust wedge at 407 m LSF). Very sharp horizontal contacts shown on Run 1 are artifacts. Artifacts occur throughout section shown at ~20 cm intervals. Breakouts are outlined in magenta. Note widening and increased vertical extent of breakouts in Run 2 in comparison to Run 1. Also note overall consistency of breakout orientation between Runs 1 and 2. Data from Run 2 were used in analysis of breakout geometry in relogged interval. Runs were separated by ~3 days with seawater filling the hole. Note that image data extend to 421 m LSF. LWD = logging while drilling, green vertical line = Pad 1 azimuth (P1AZ).

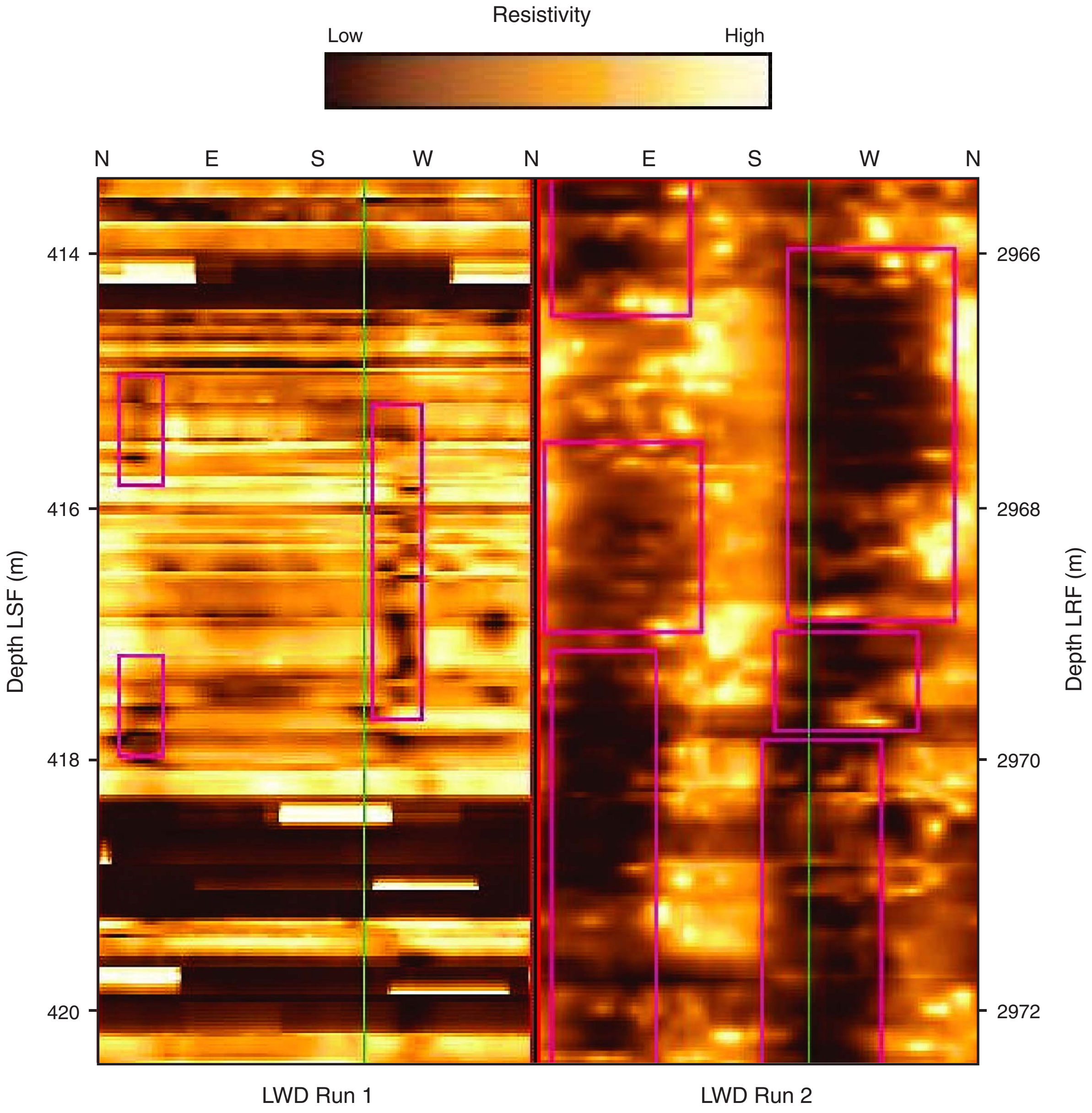

Figure F16. Breakout azimuth versus depth. Note sharp shift in azimuth between overridden slope deposits and thrust wedge.

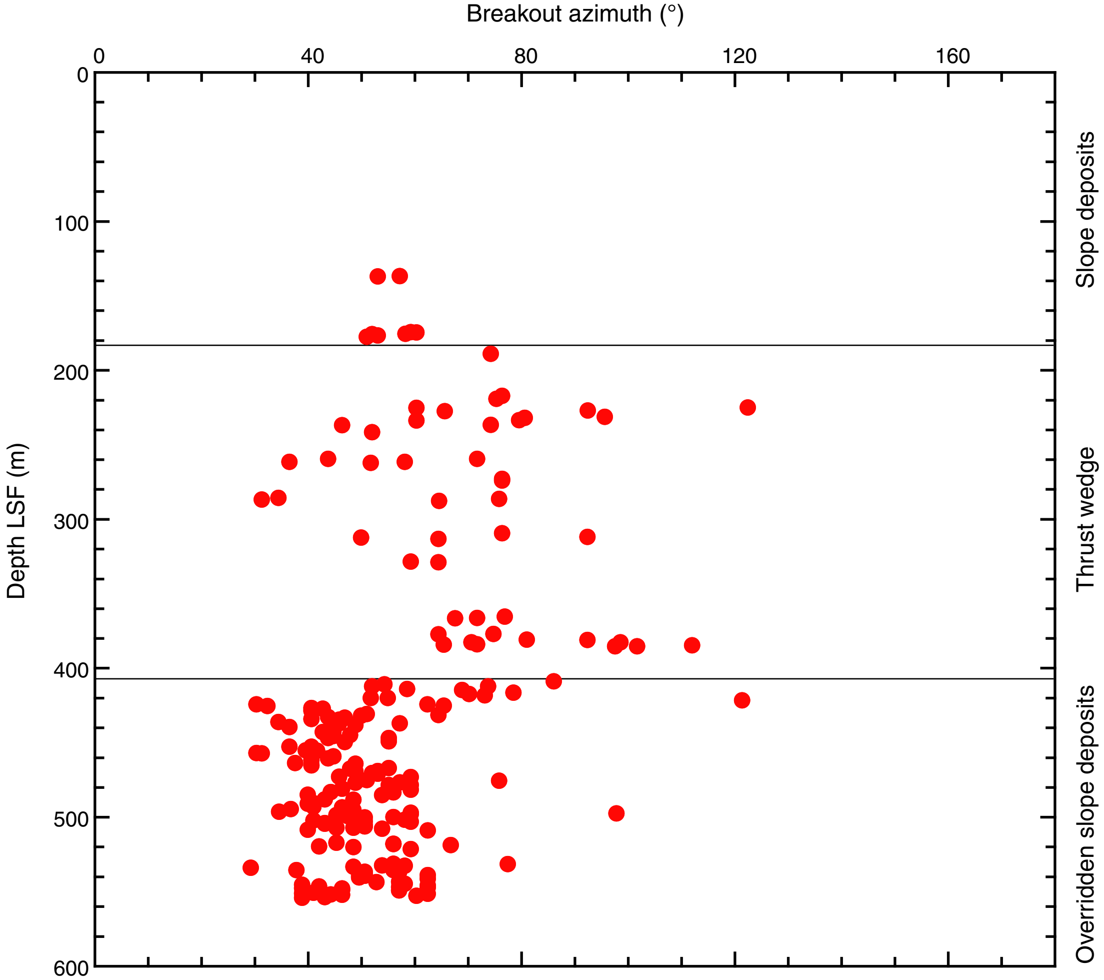

Figure F17. Histogram of breakout orientation. Breakouts with orientations from 0°–360° are all projected onto 0°–180° display. Standard deviation of 15° indicates a quality level of "B" (Zoback, 2007).

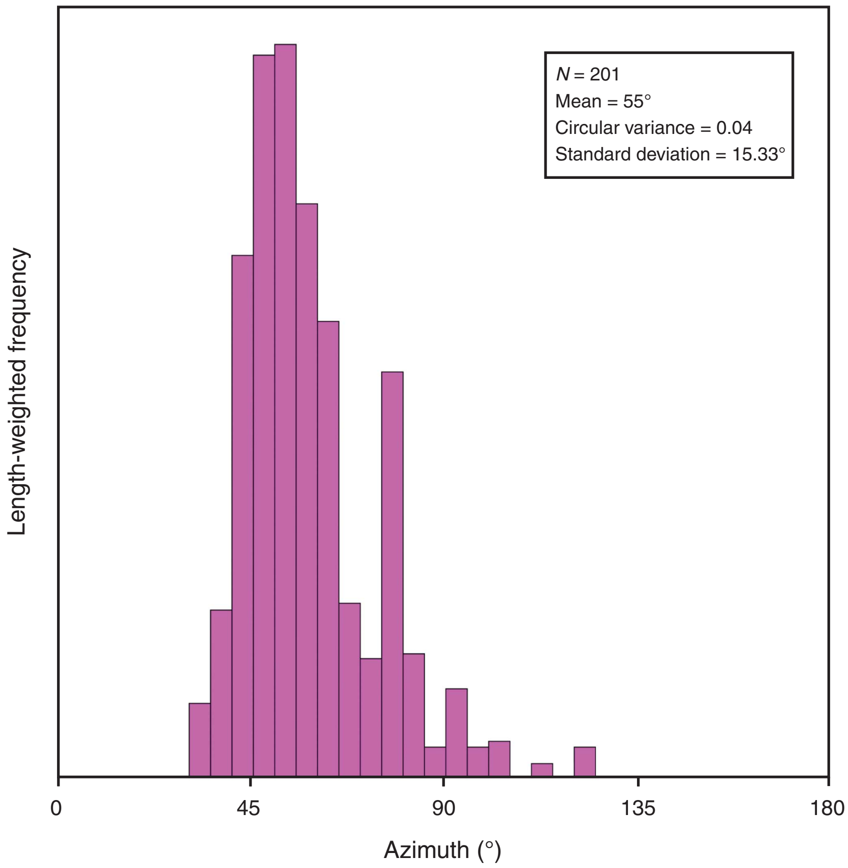

Figure F18. Map showing orientation of S_{Hmax} across NanTroSEIZE transect, including results from Site C0010. Red lines = mean value of S_{Hmax} direction at all sites, except at Site C0002. At Site C0002, red = S_{Hmax} value for upper part of the section, blue = clockwise rotation of S_{Hmax} toward bottom of hole (Tobin et al., 2009a). Yellow arrows = relative plate motions between Philippine Sea plate and southwest Japan as estimated by Seno et al. (1993) (shorter more northerly arrow) and Miyazaki and Heki (2001) (longer more westerly arrow). Kii Global Positioning System (GPS) measurement (black arrow) is motion of Kii Peninsula determined relative to an island in Japan Sea (Kamitsushima Island) (Heki, 2007).

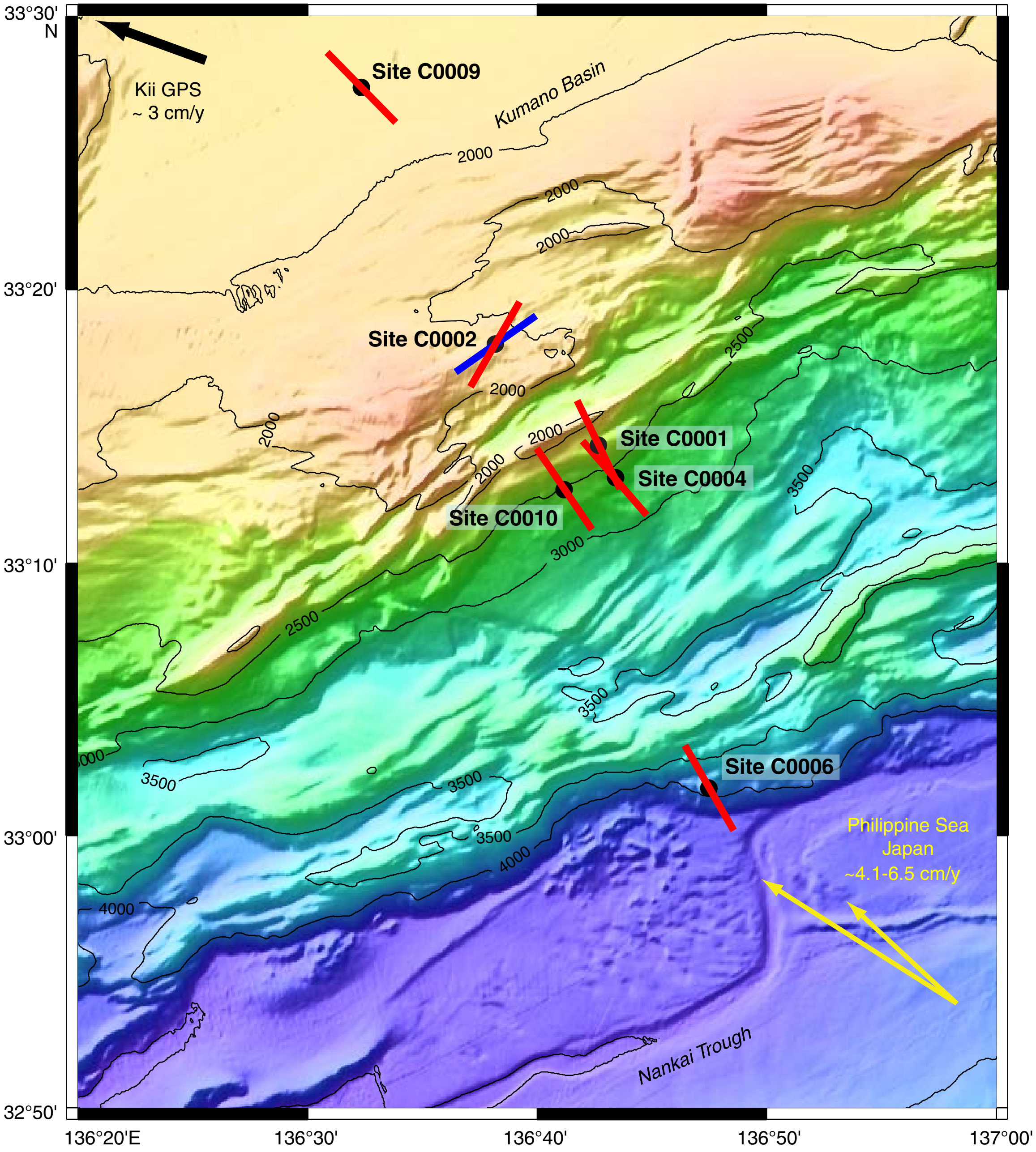

Figure F19. Seismic data correlated to well data, Site C0004. Expedition 314 logging units and Expedition 316 lithologic units from Expedition 314 Scientists (2009b) and Expedition 316 Scientists (2009), respectively are also displayed. Top wedge and base wedge are surfaces mapped on seismic data that represent top and base of thrust wedge. Seismic data displayed are time-based (scale on right).

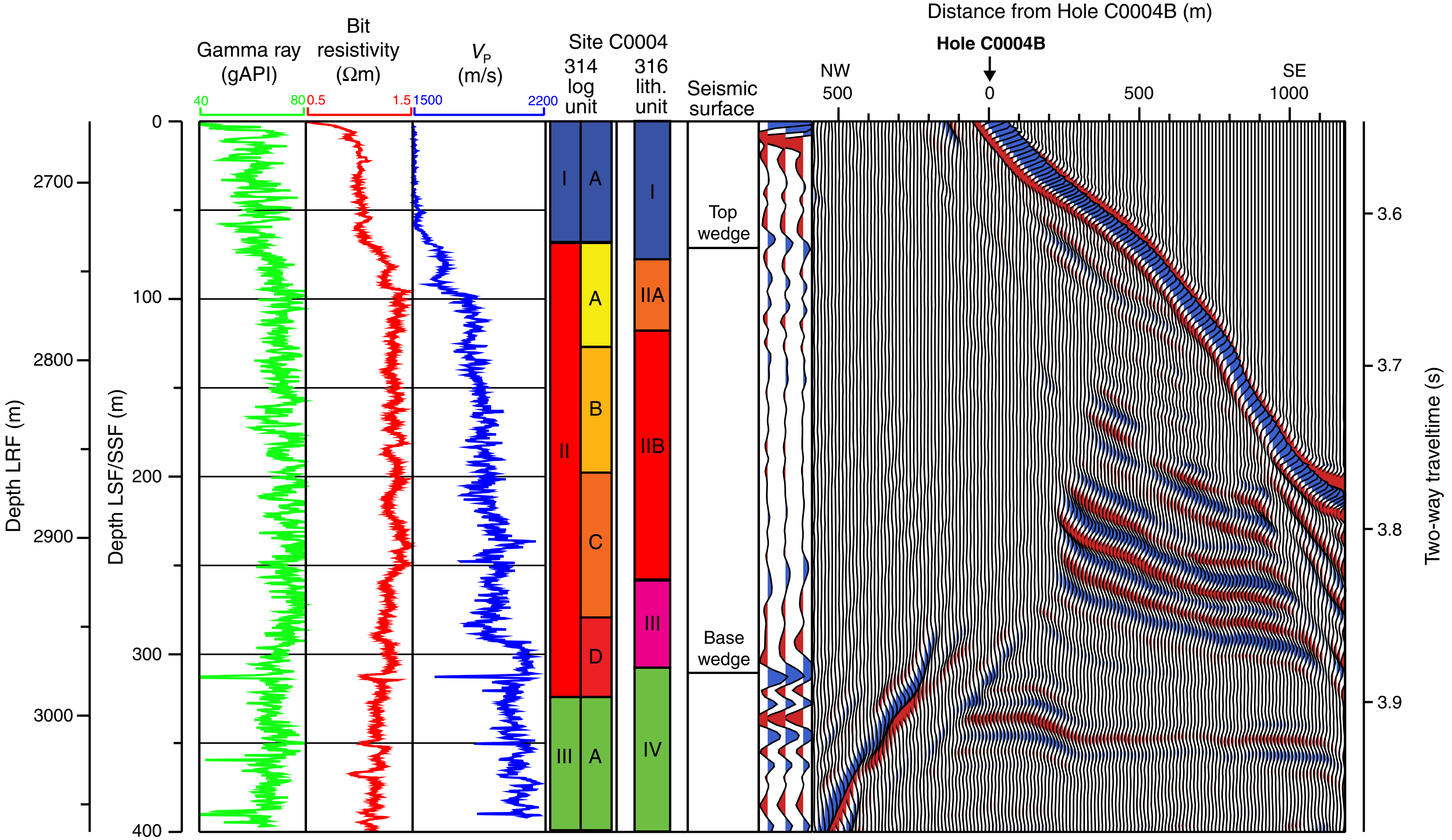

Figure F20. Bit, ring, deep (blue), medium (red), and shallow (green) resistivity versus depth. Black = Run 1, Blue = Run 2, Red = interval relogged in Run 2. Gray shaded areas exhibit considerable variability in resistivity.

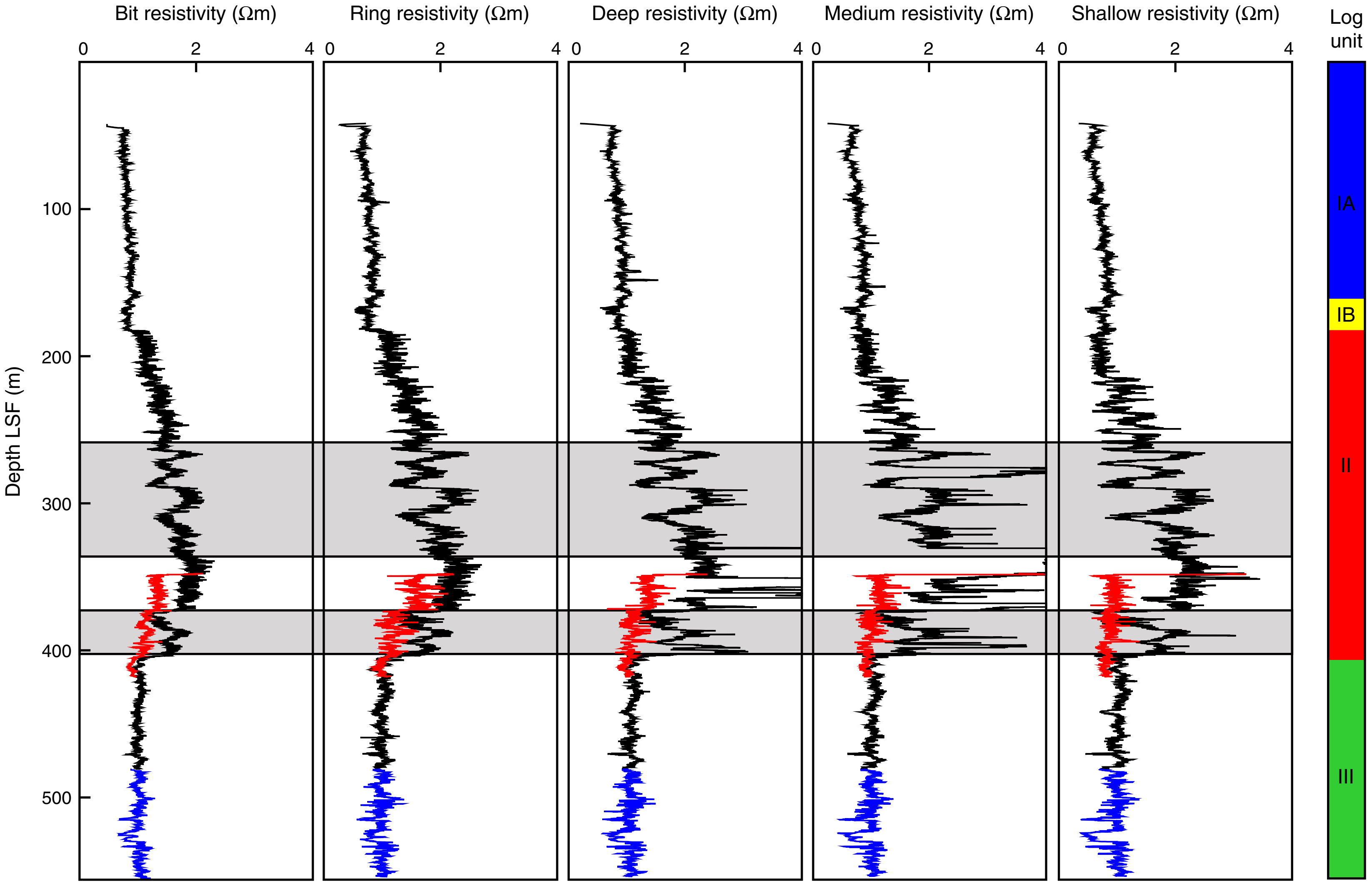

Figure F21. Deep, medium, and shallow resistivity versus depth. Difference between deep- and shallow-button resistivity as a measure for invasion. Green = shallow resistivity, red = medium resistivity, blue = deep resistivity.

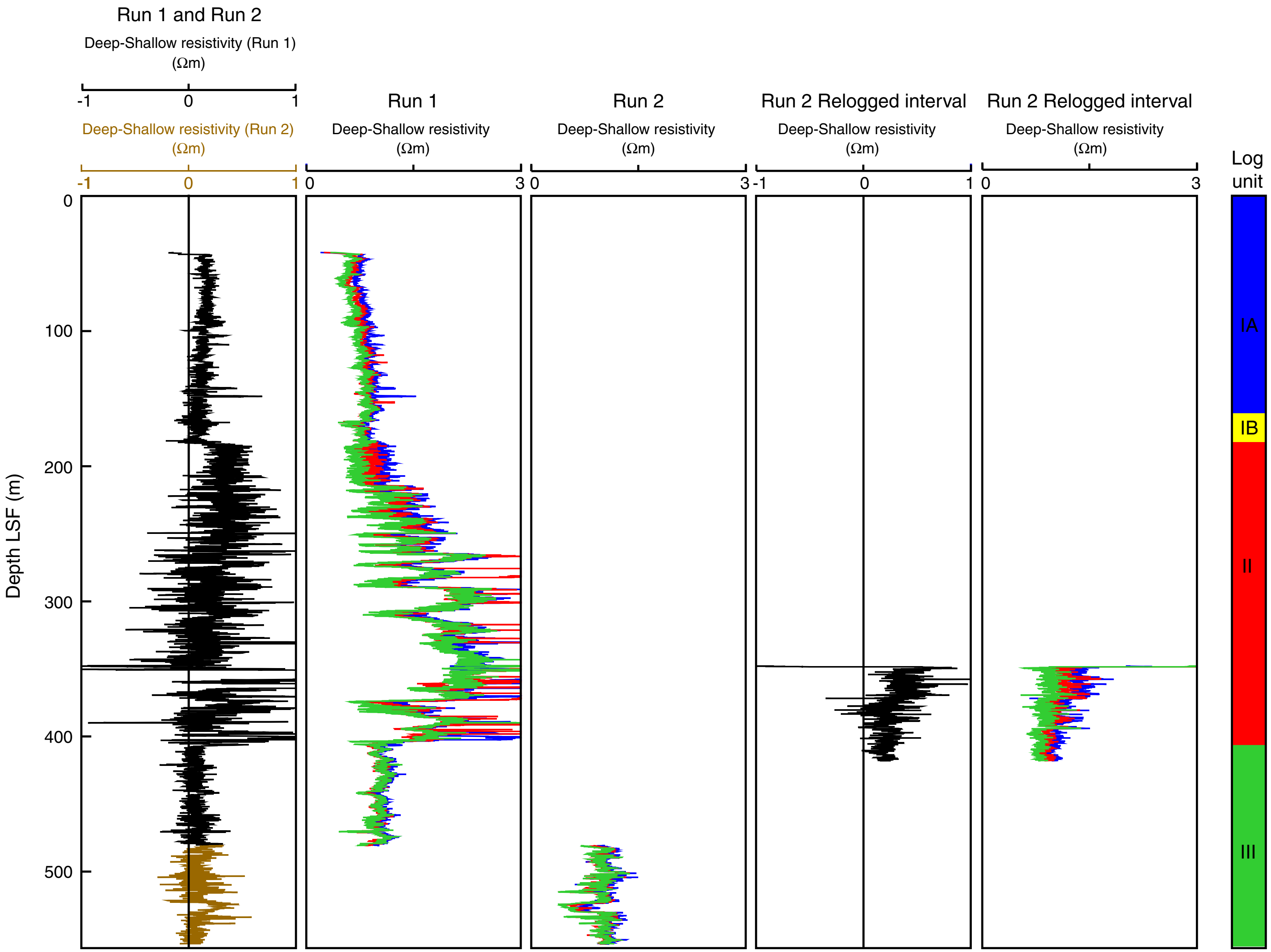

Figure F22. Resistivity-derived porosity (Achie's law parameters: a = 1, m = 2.3) versus depth and calculated compaction trend for slope sediments. Red = relogged interval, black = Run 1, blue = Run 2.

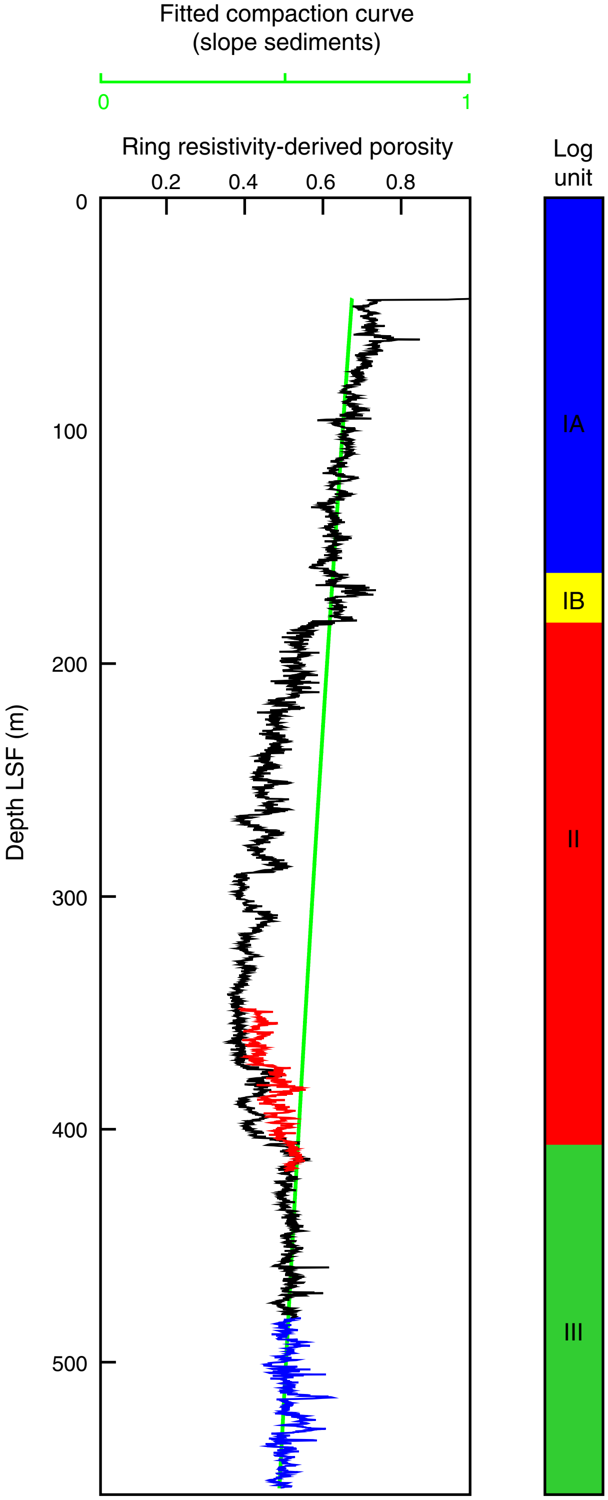

Figure F23. Comparison of resistivity-derived porosity at Site C0010 using three Archie's law parameters and resistivity-derived porosity at Site C0004. Curves at the two sites are registered at top of wedge (Unit II).

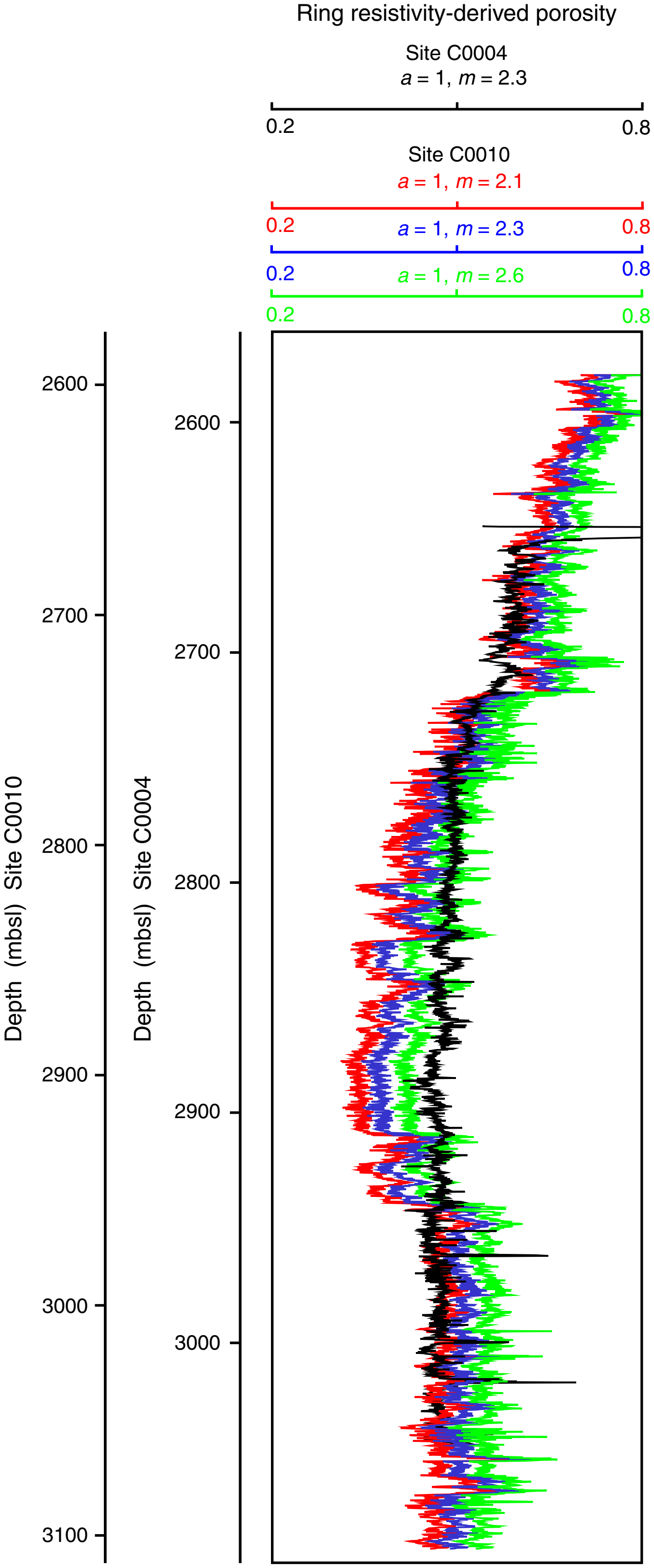

Figure F24. Bathymetry (contours), seismic lines (thick black lines), and IODP sites (red and black dots, red dots: sites discussed in this section). Seismic lines are displayed in Figures F30, F31, and F32. IL = in-line, XL = cross-line of seismic tracks. Modified from Araki et al. (2009).

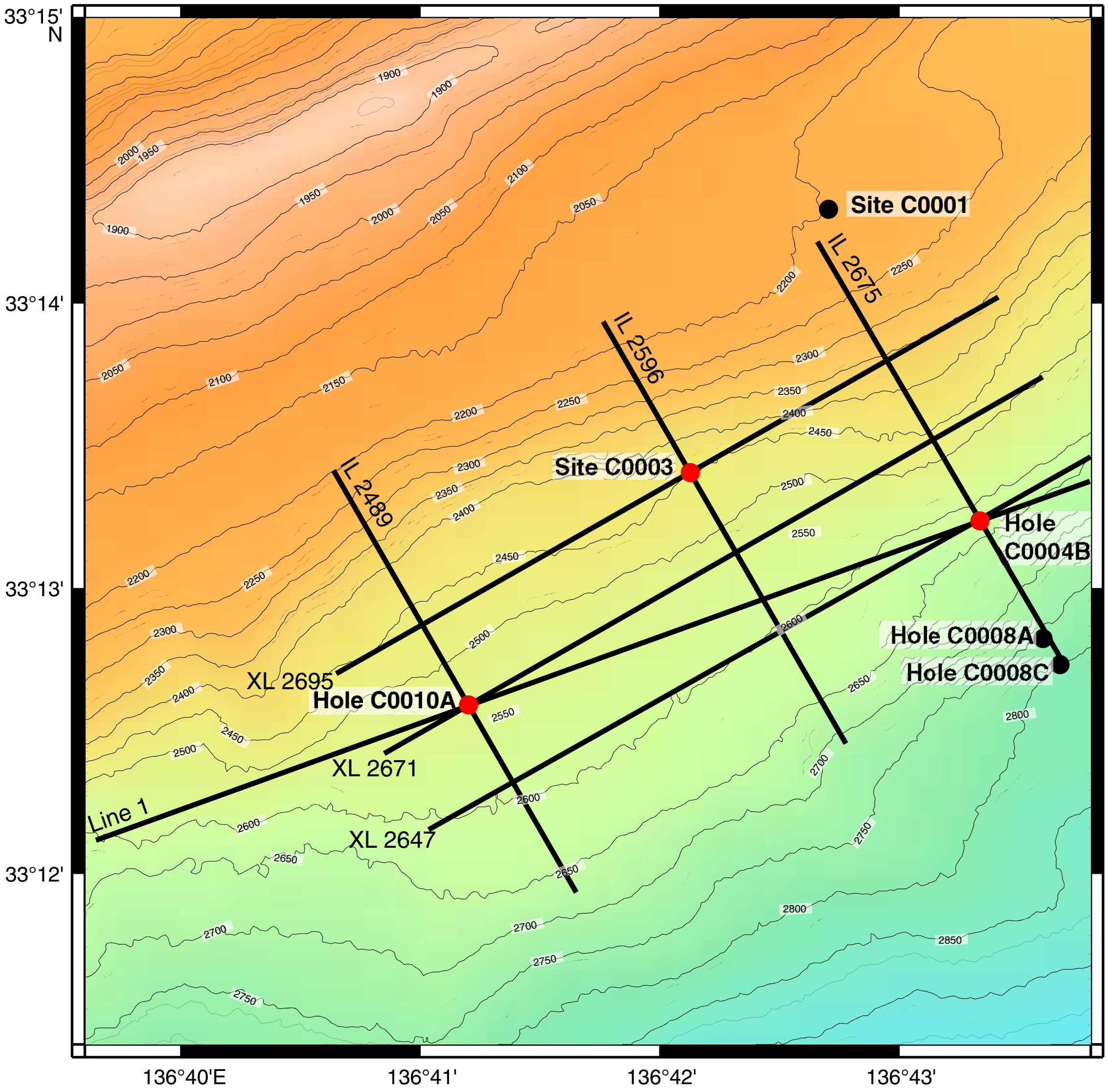

Figure F25. One-way traveltime versus depth based on check shot data, Sites C0003 and C0004 (Expedition 314 Scientists, 2009a, 2009b). Δ*t* = Site C0004 traveltime – Site C0003 traveltime. Unit boundaries are indicated by arrows.

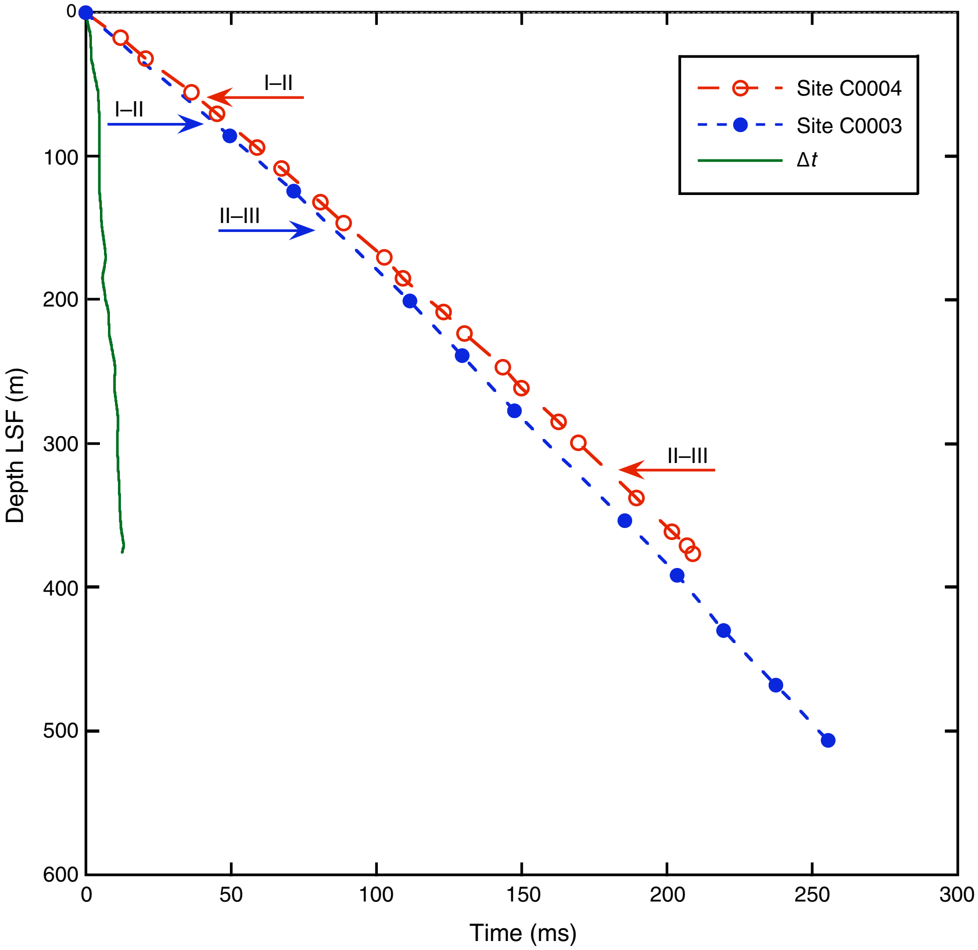

Figure F26. Interval velocity versus depth based on check shot data, Sites C0003 and C0004 (Expedition 314 Scientists, 2009a, 2009b). Unit boundaries are indicated by arrows.

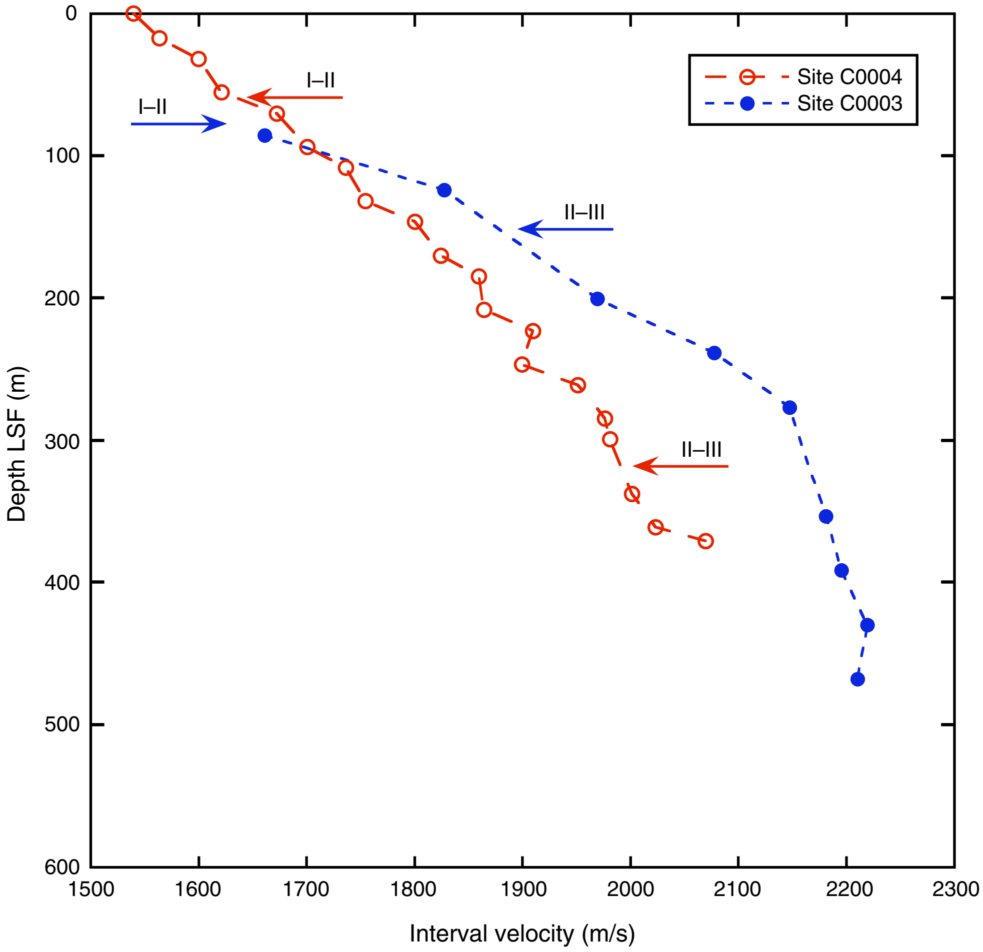

Figure F27. Seismic data correlated to well data, Site C0003. Logging data displayed represent real-time (MWD) data because LWD tool was lost during drilling (see Expedition 314 Scientists, 2009a). Expedition 314 logging units derived from Expedition 314 Scientists (2009b) also displayed. Top wedge is surface mapped on seismic data that represents top of thrust wedge. Seismic data displayed are time-based (scale on right).

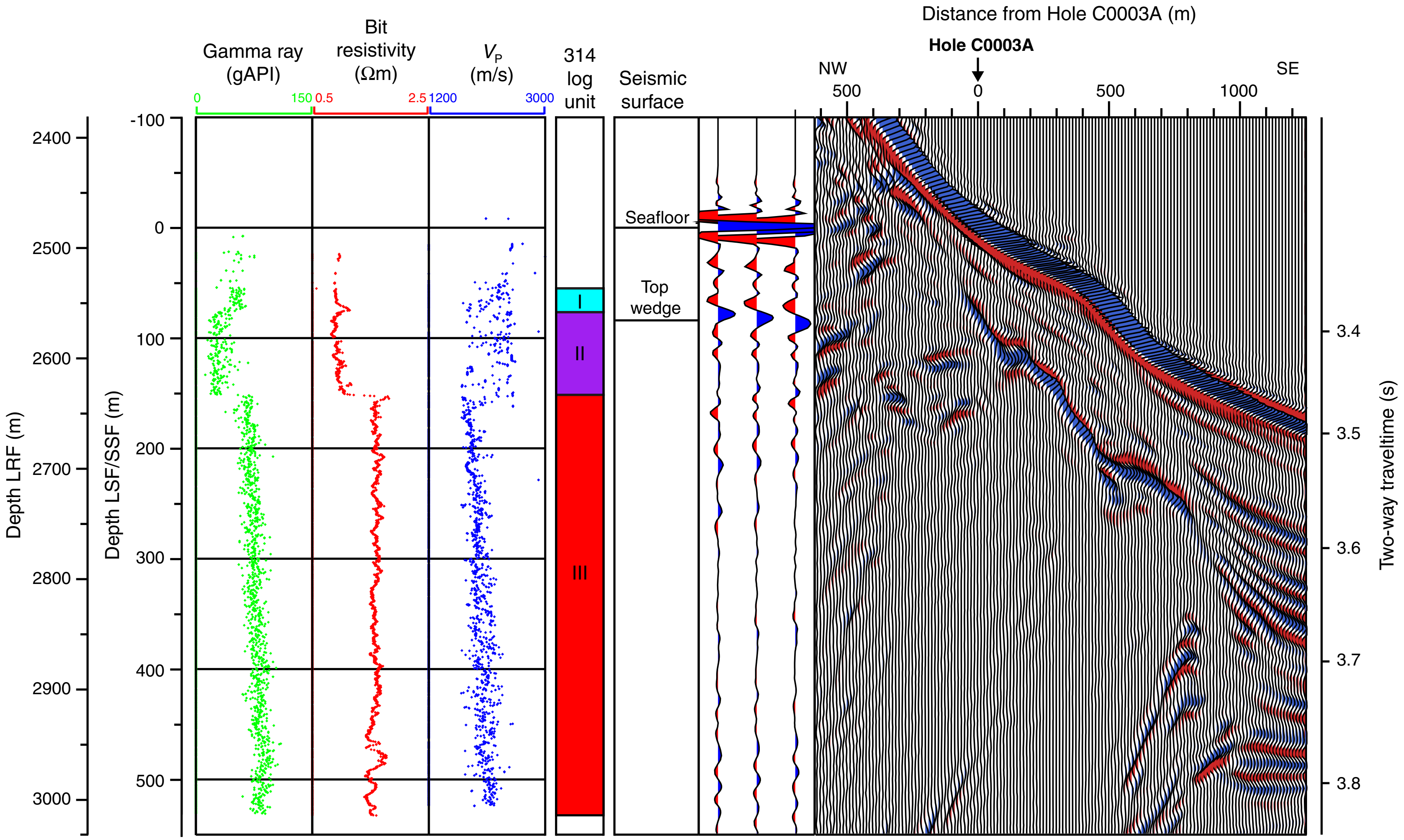

Figure F28. Seismic data correlated to well data, Site C0010. Top wedge and base wedge are surfaces mapped on seismic data that represent top and bottom of thrust wedge. Seismic data displayed are time-based (scale on right).

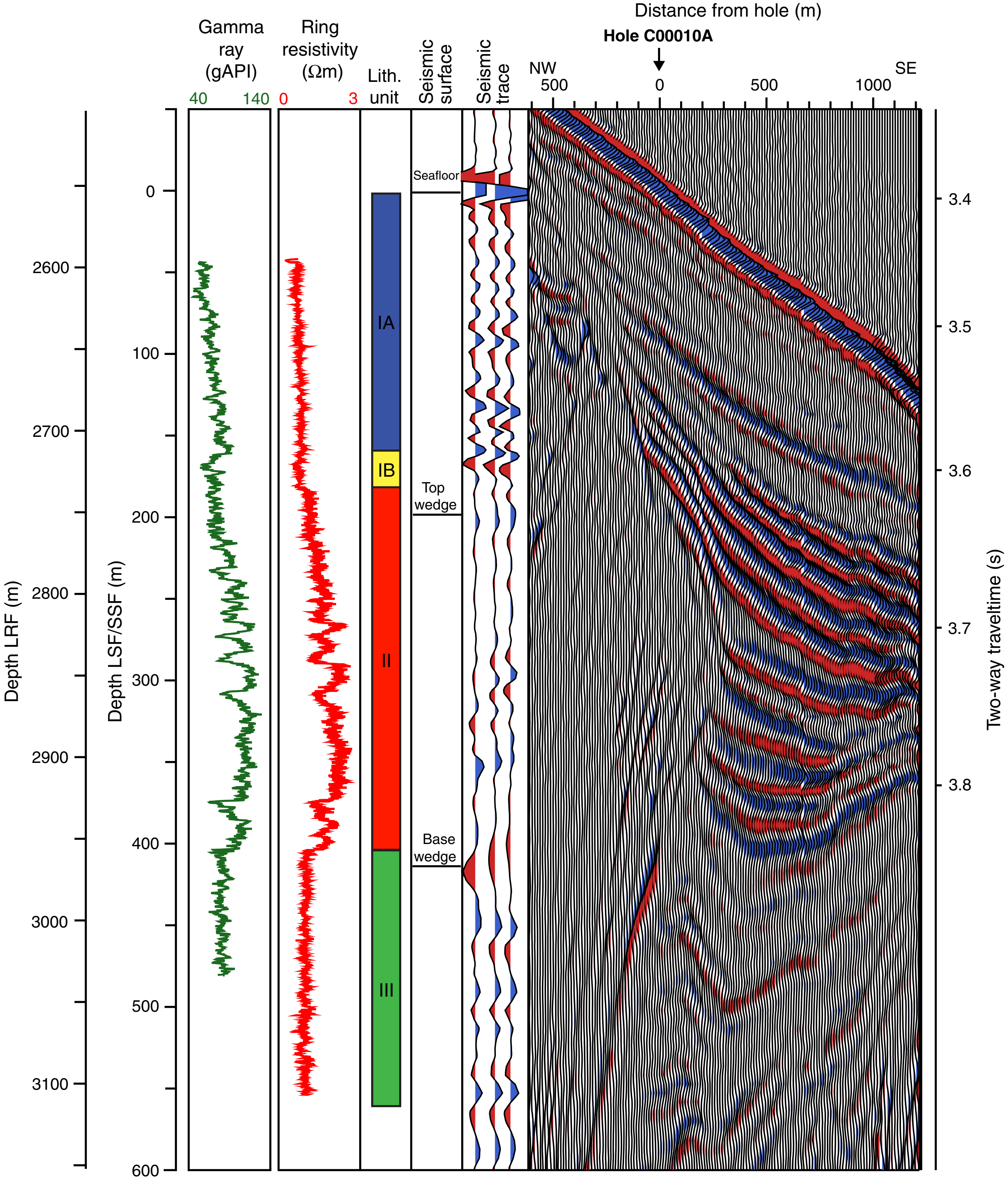

Figure F29. Comparison of Site C0010 and Site C0004 log data. Within thrust wedge, Site C0010 has higher gamma ray and resistivity values than Site C0004. Seafloor depth is different at each location, so depth below seafloor is not used for data display.

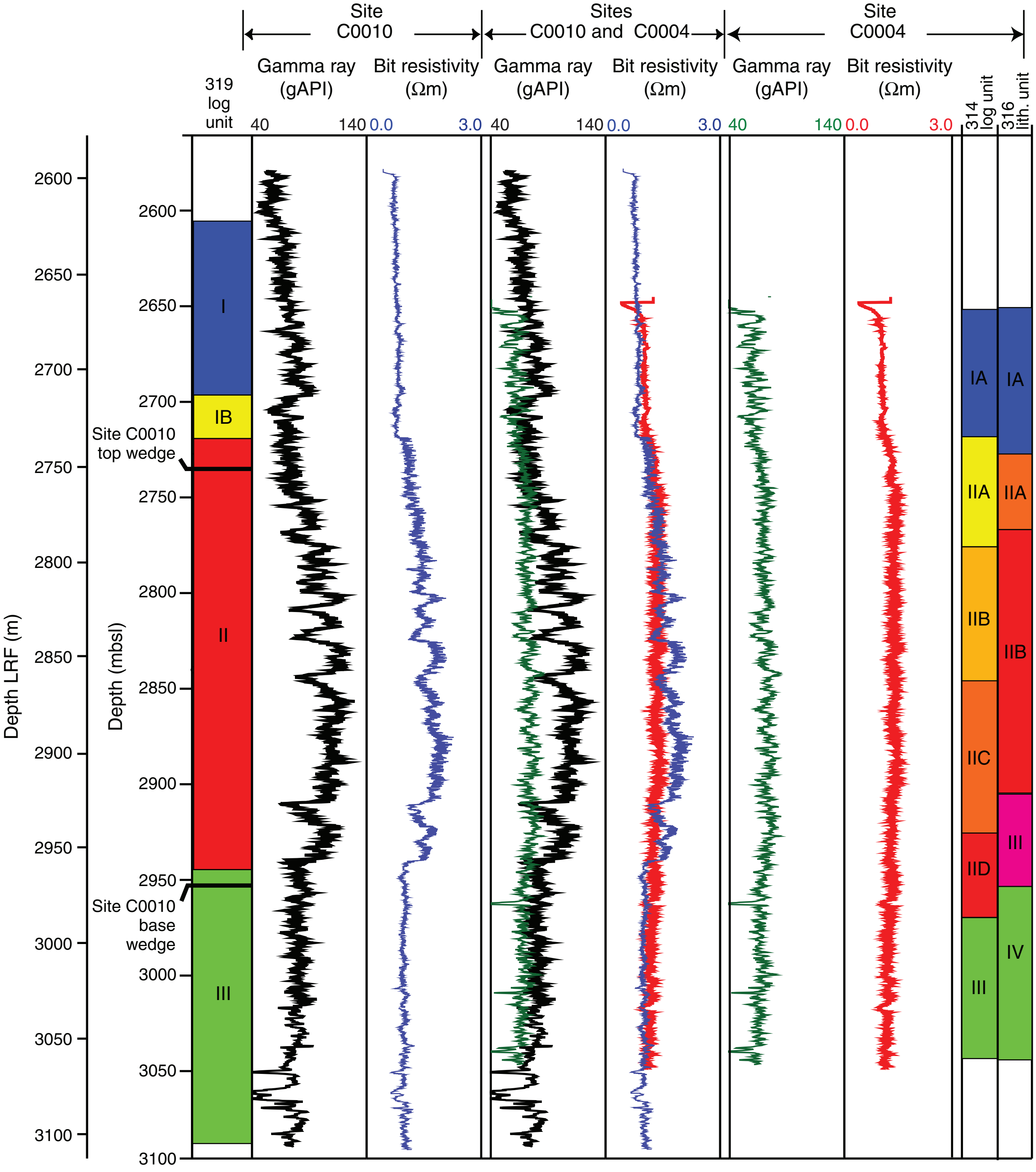

Figure F30. Seismic section between Site C0004 and Site C0010 (Line 1 in Fig. F24). Locations are ~3.5 km apart. Note that there is increased seismic amplitude within thrust wedge at Site C0010 than at Site C0004. XL = cross-line, IL = in-line of seismic tracks, VE = vertical exaggeration.

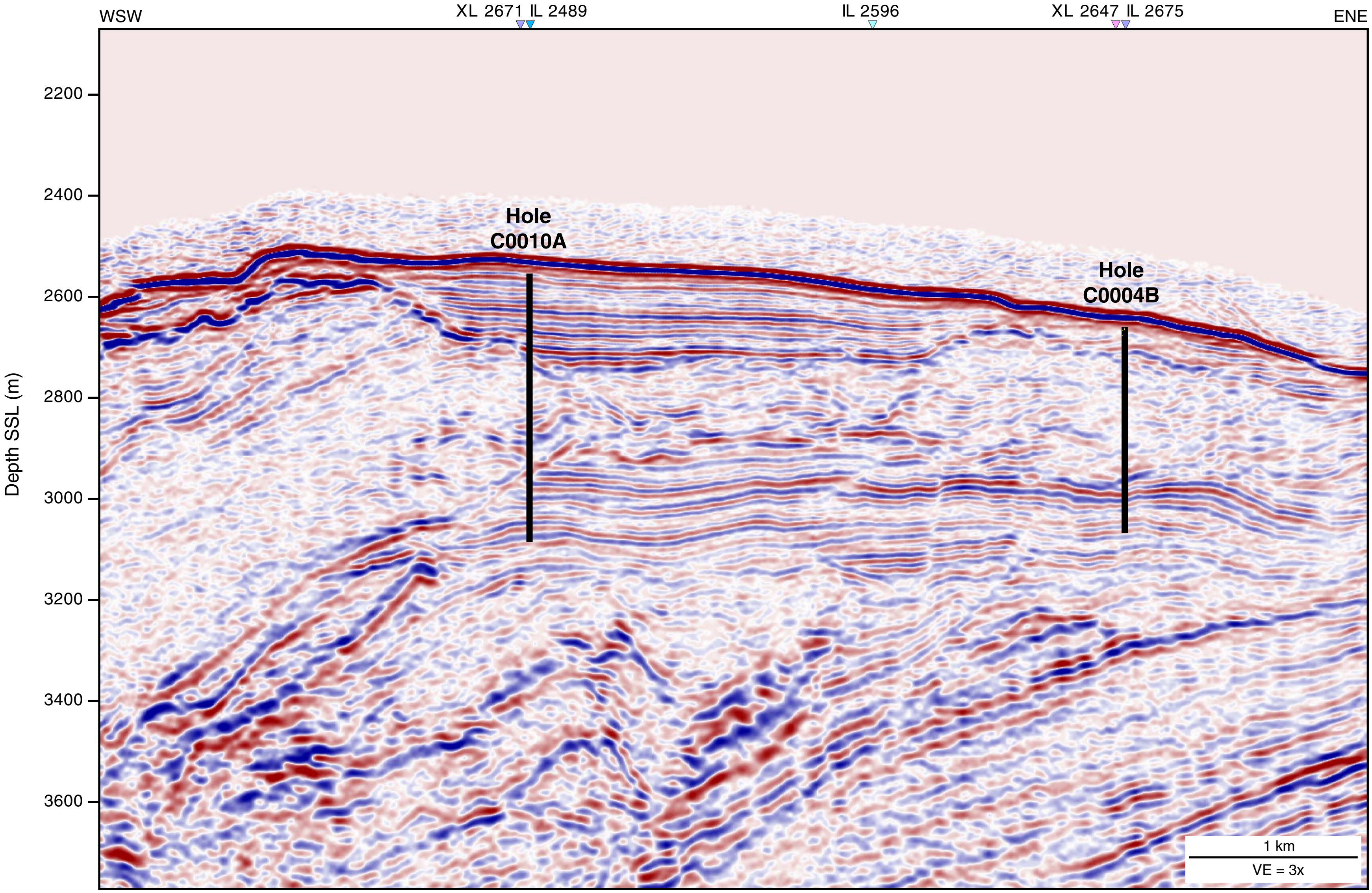

Figure F31. Dip seismic lines through (**A**) Site C0004, (**B**) Site C0003, and (**C**) Site C0010. Locations in Figure F24. XL = cross-line, IL = in-line of seismic tracks, VE = vertical exaggeration.

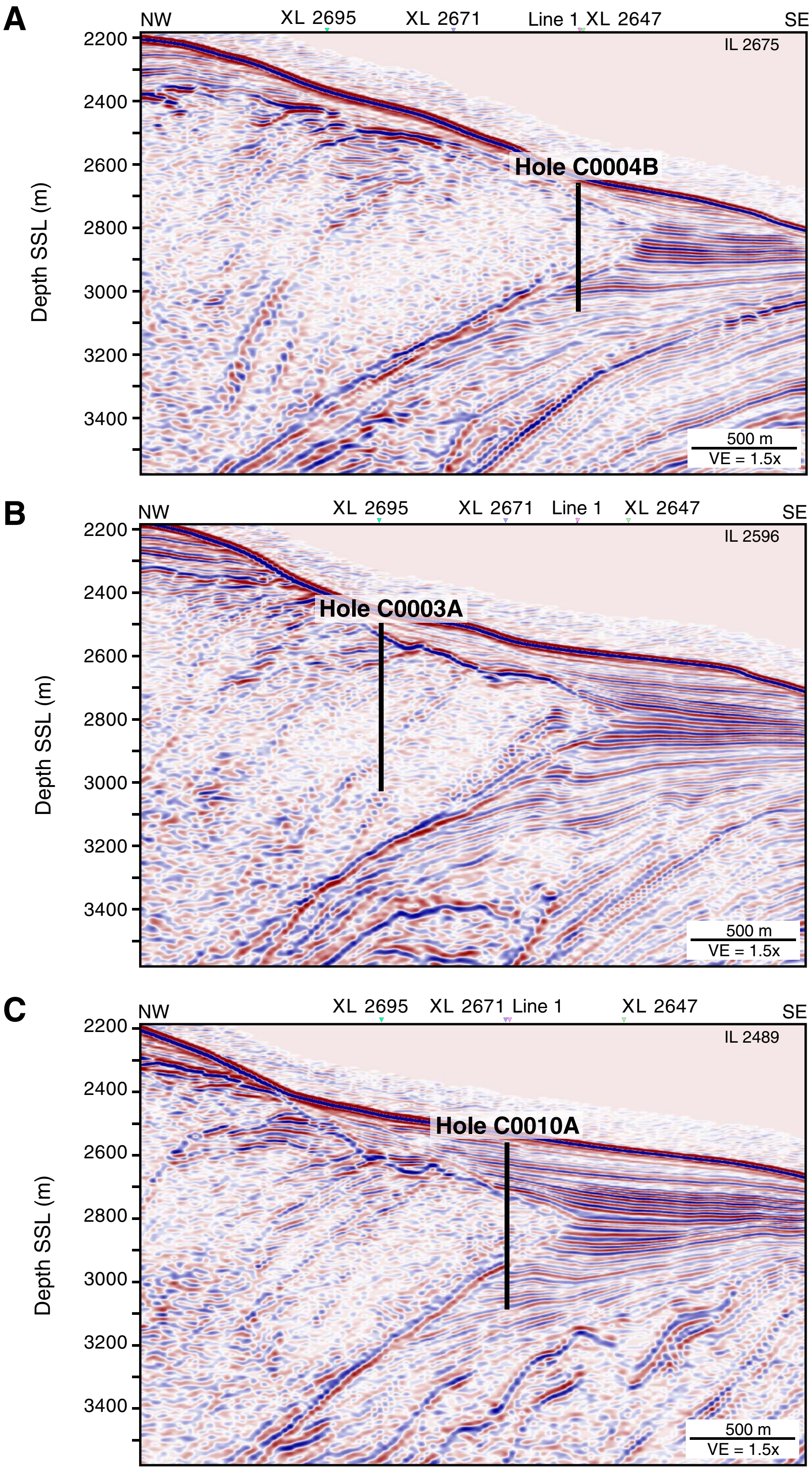

Figure F32. Strike lines through (**A**) Site C0004, (**B**) Site C0003, and (**C**) C0010. Locations in Figure **F24.** IL = in-line, XL = cross-line of seismic tracks, VE = vertical exaggeration.

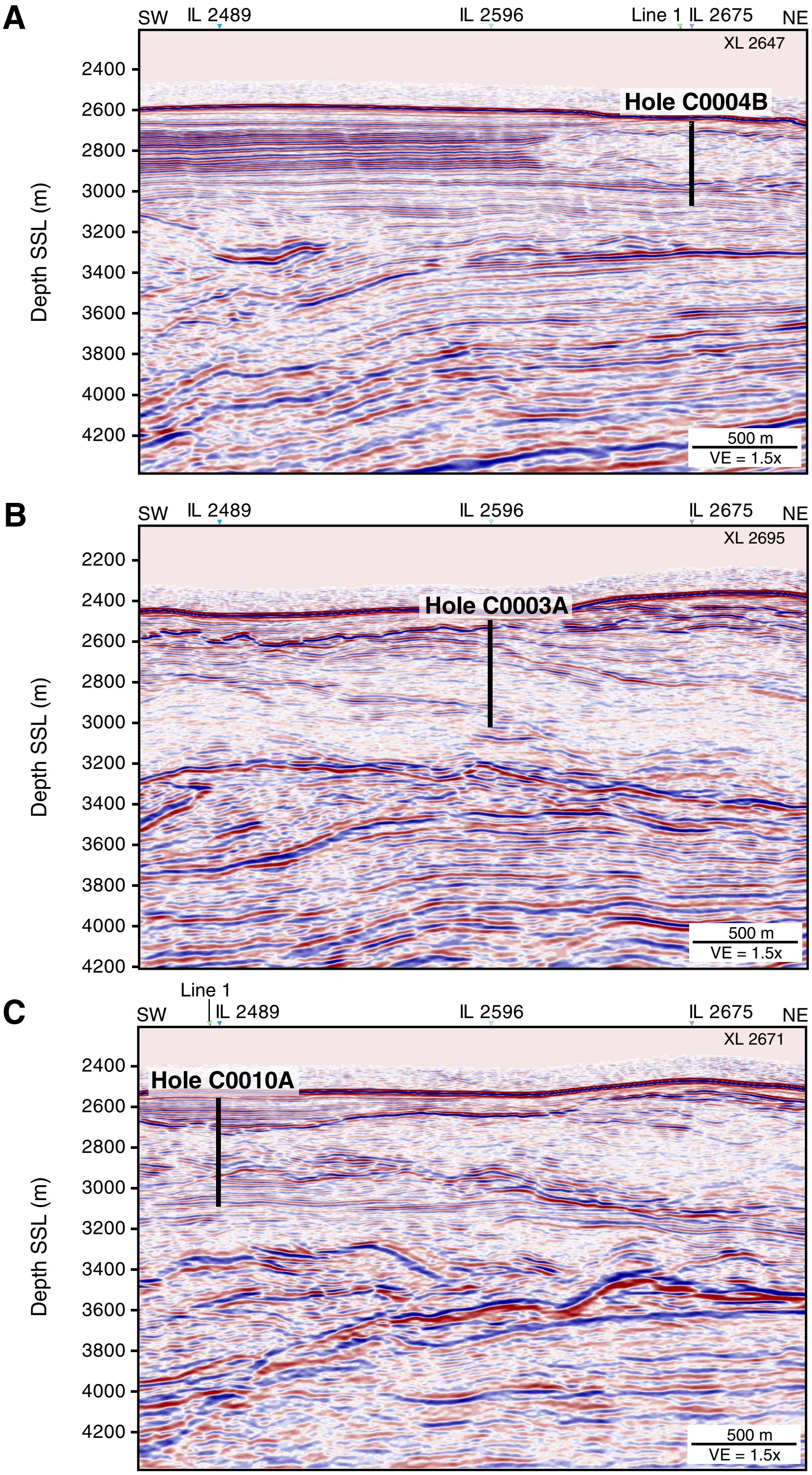

Figure F33. Strainmeter test result from 12 August 2009. Strainmeter electronics temperature and paroscientific sensor pressure and temperature are also plotted. Yellow column = period of pressurization test for each strain sensor as indicated by top of column.

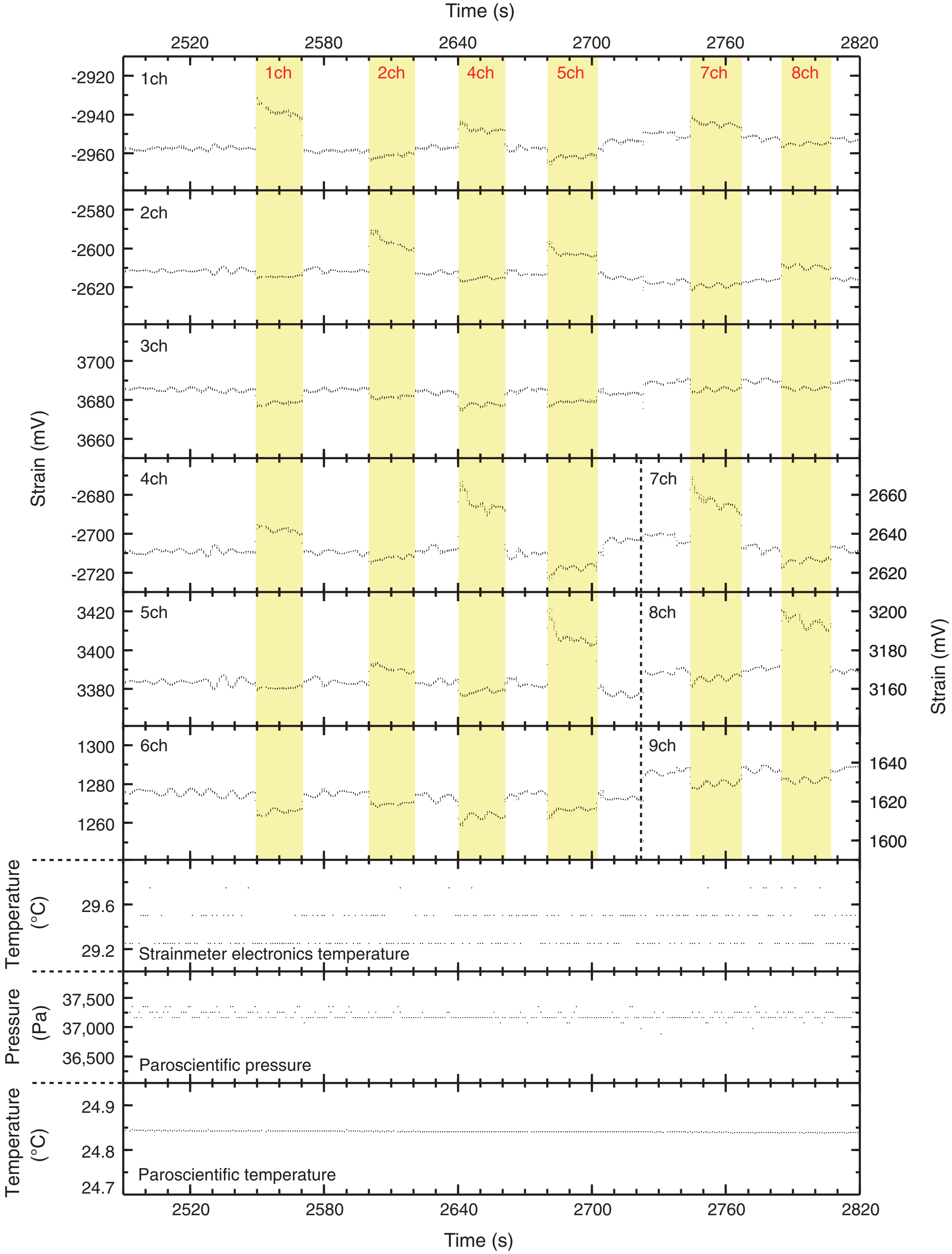

Figure F34. Accelerometer-tiltmeter test result from 13 August on deck. Acceleration data are dominated by sensor noise.

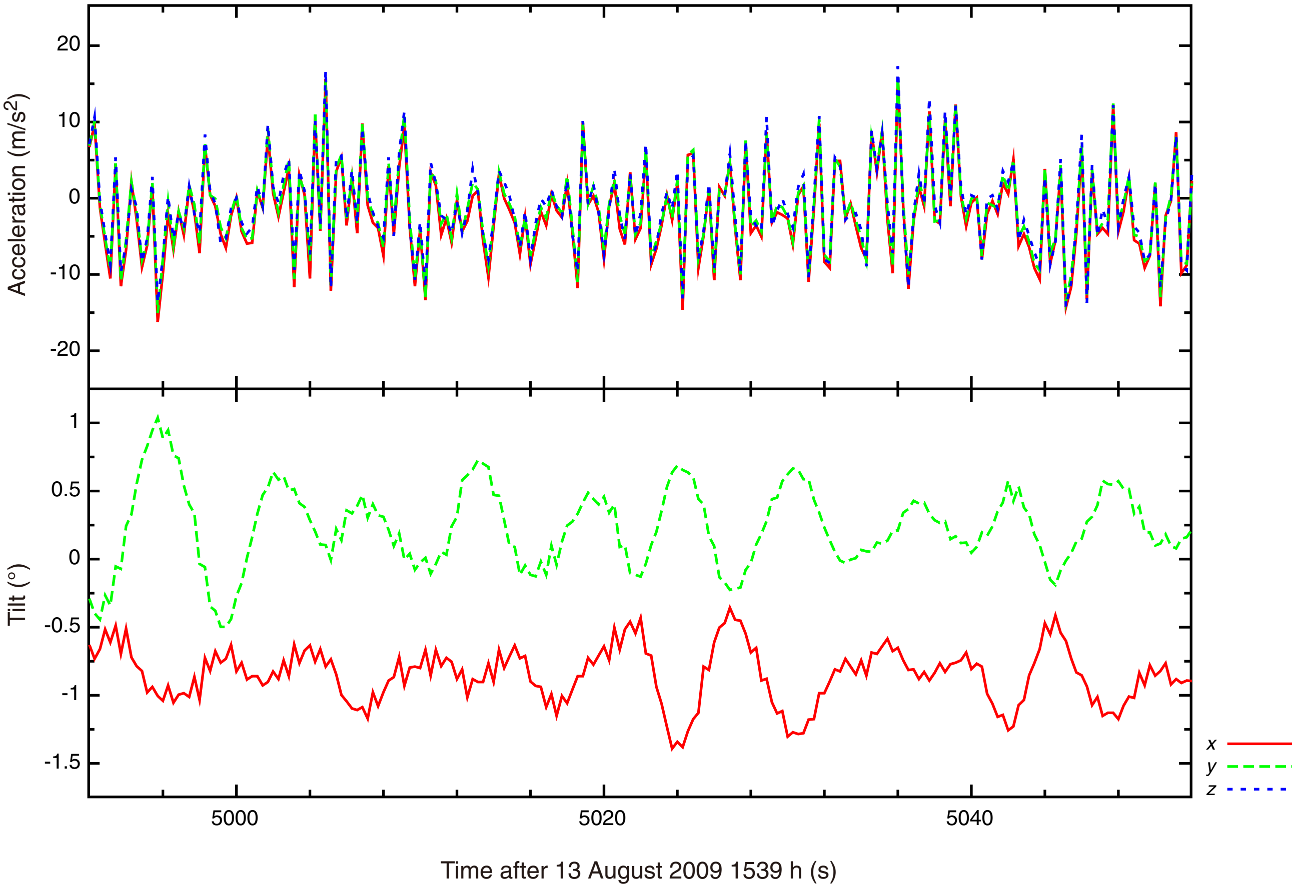

Figure F35. Photograph of instrument carrier fit test conducted on 12 August 2009.

Figure F36. Photograph of strainmeter, sensor carrier, and sensor placement. Two seismometers, accelerometer-tiltmeter, and eight miniature temperature loggers (MTLs) were attached to instrument carrier. Schematic drawing of strainmeter and instrument carrier shown in Figs. F25 and F26 in the "Methods" chapter.

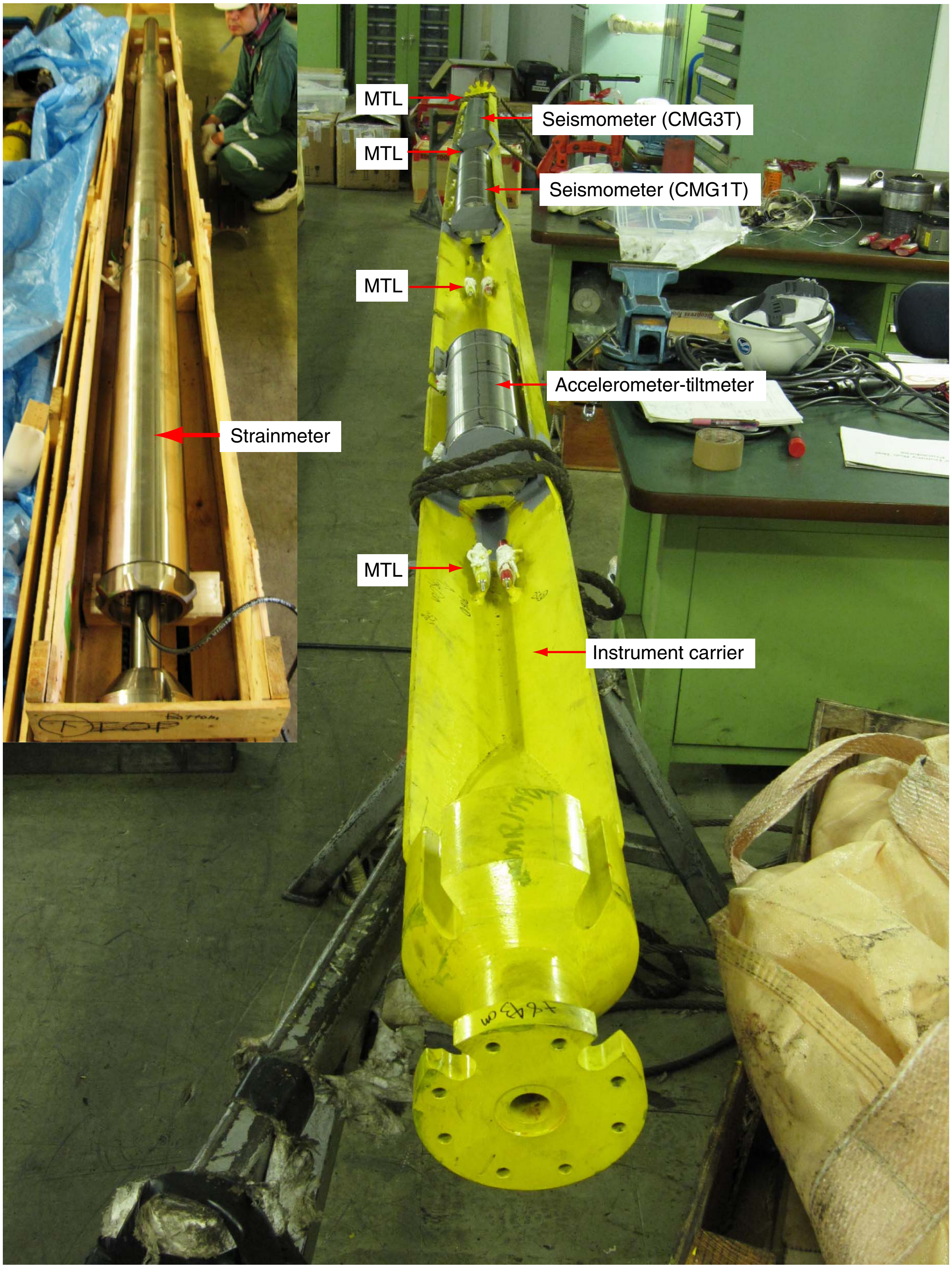

Figure F37. Photograph of sensor assembly after first dummy run test. Broken bands, broken and bent protector, and disconnected flange caused by vibration during deployment are also shown.

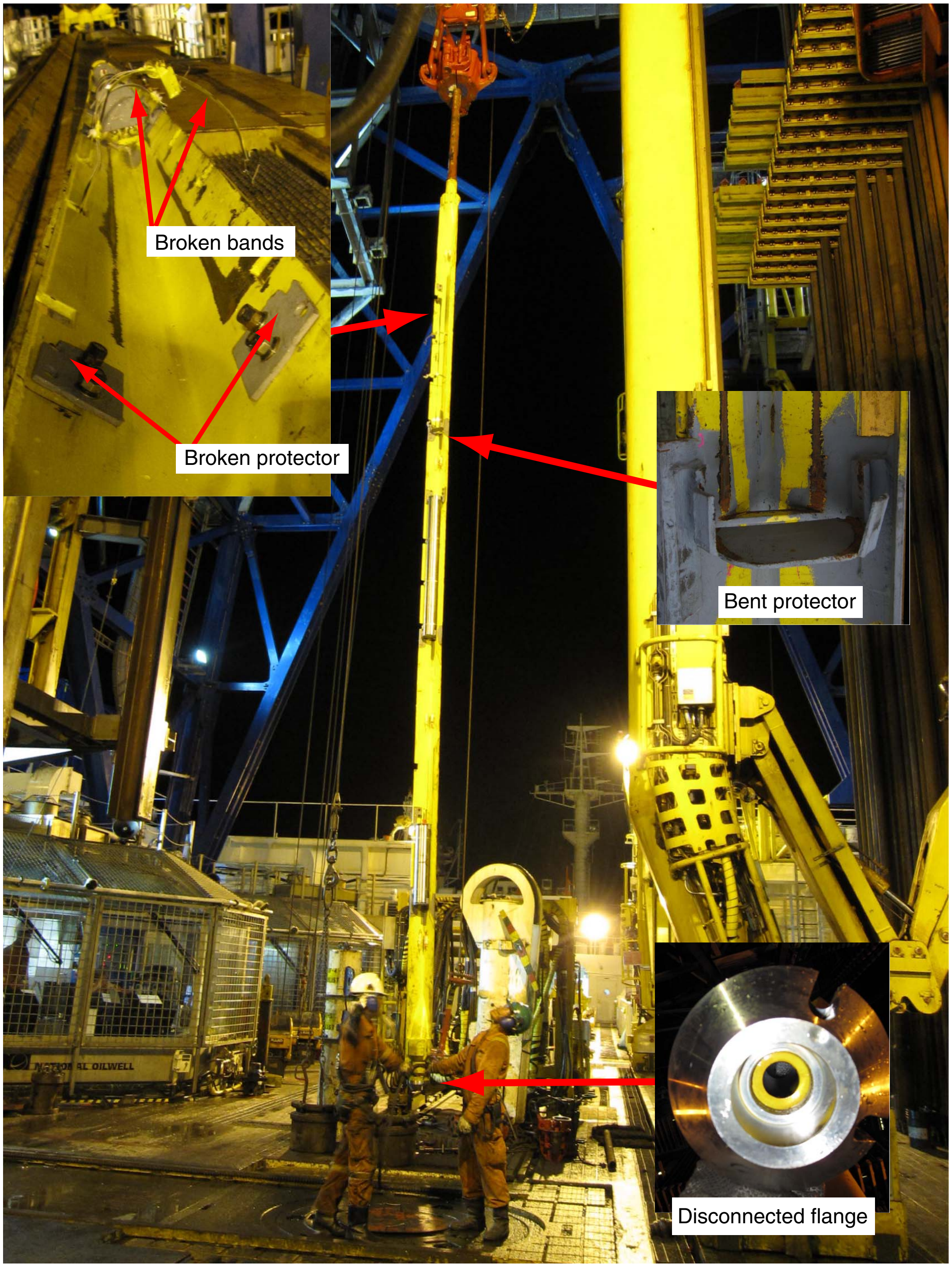

Figure F38. Sensor tree configuration for second dummy run test. Configuration is different from first dummy run test shown in Fig. F24 in the "Methods" chapter. EUE = external upset end, XO = crossover, VAM = Vallourec and Mannesmann.

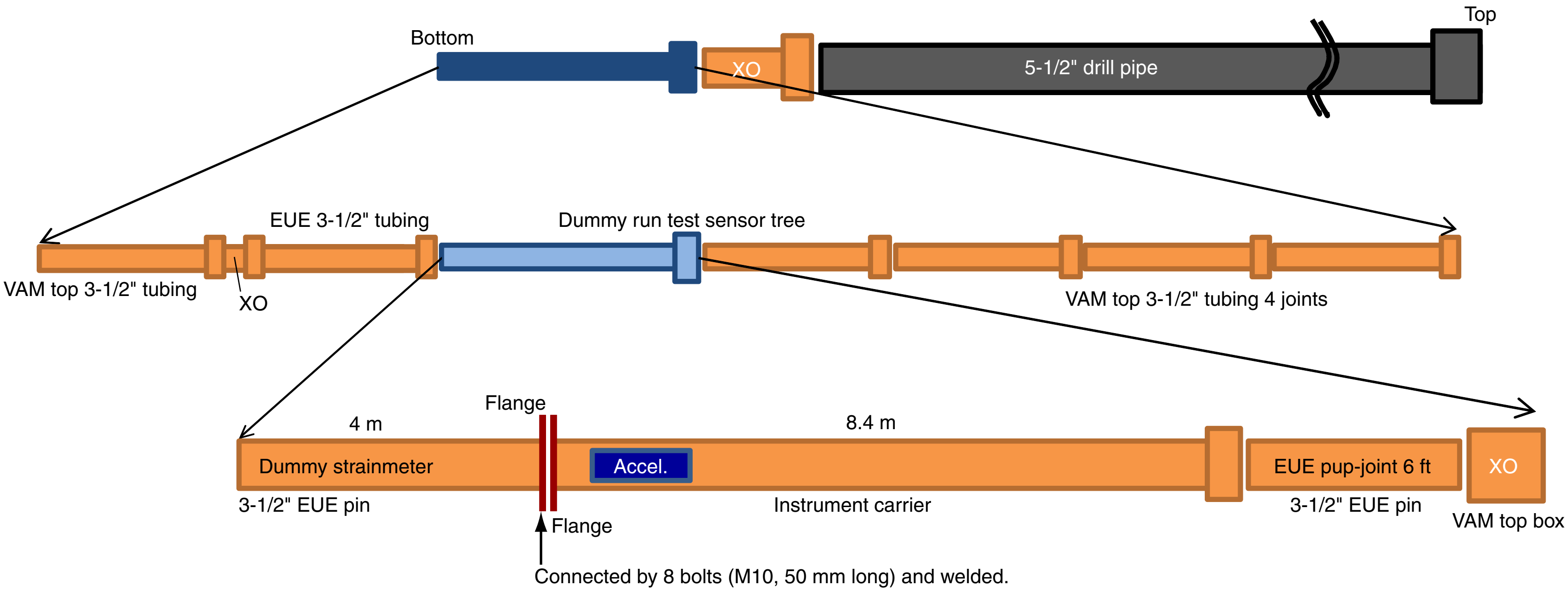

Figure F39. Photograph of sensor assembly for second dummy run test. Flanges are connected by 8 bolts and welded to strengthen connections.

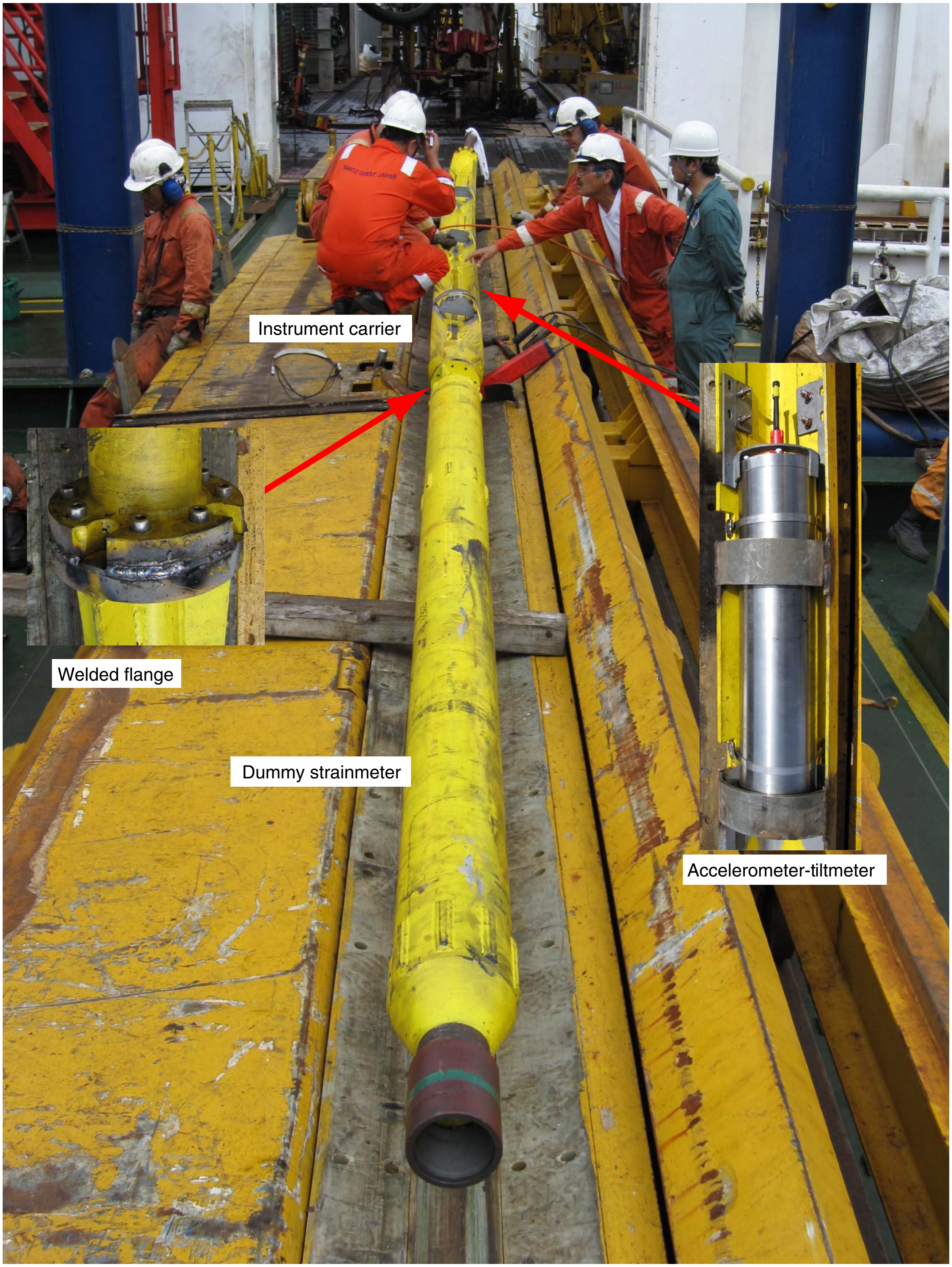

Figure F40. Remotely operated vehicle (ROV) image of second dummy run reentry into Hole C0010A. Reentry cone and bottom of sensor tree are shown.

Figure F41. Time series data from accelerometer. **A.** Data collected at 0500 h on 8 August. (**Continued on next page.**)

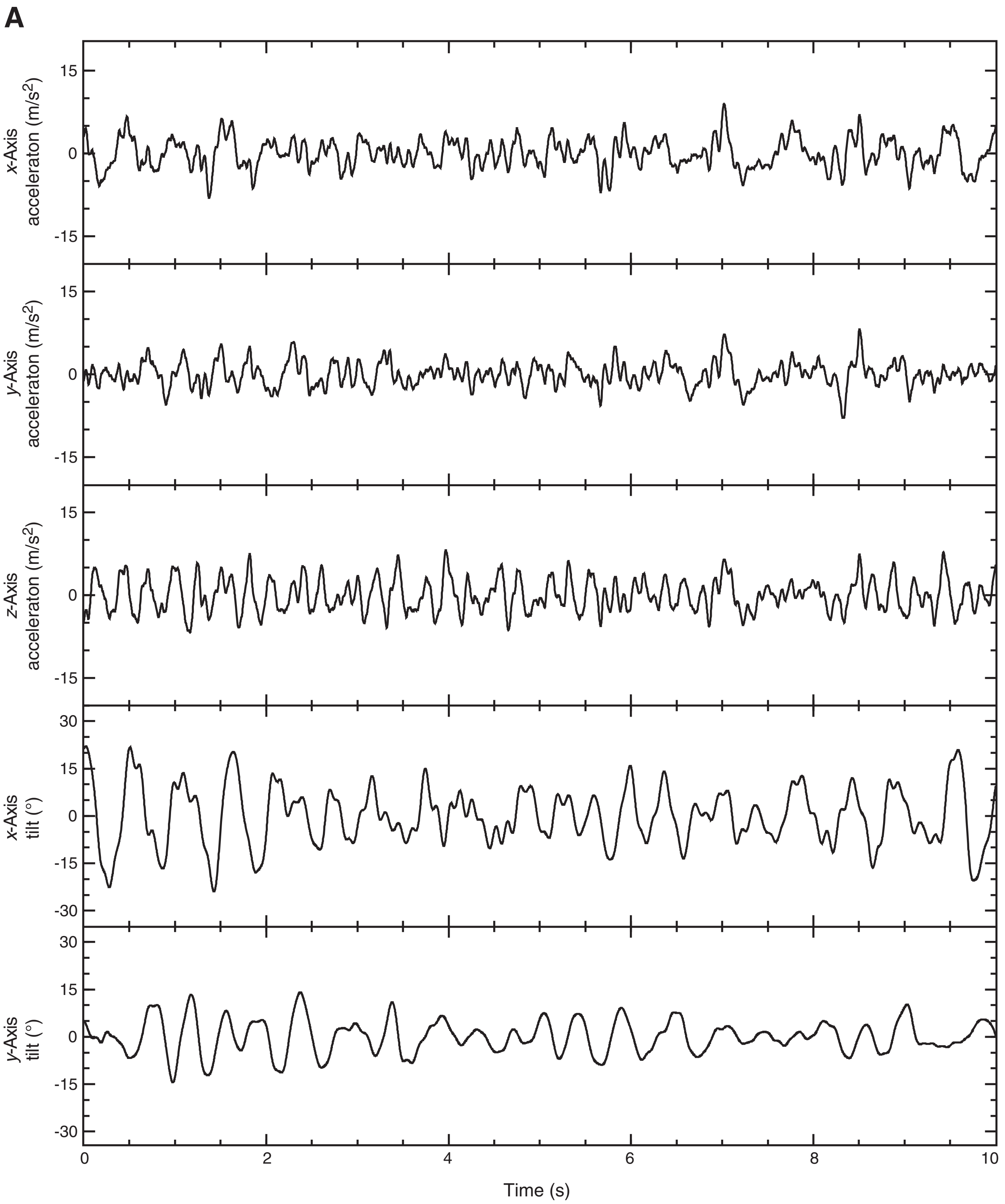

Figure F41 (continued). B. Data collected at 0815 h. A 0.1–1 Hz bandpass filter was applied to data.

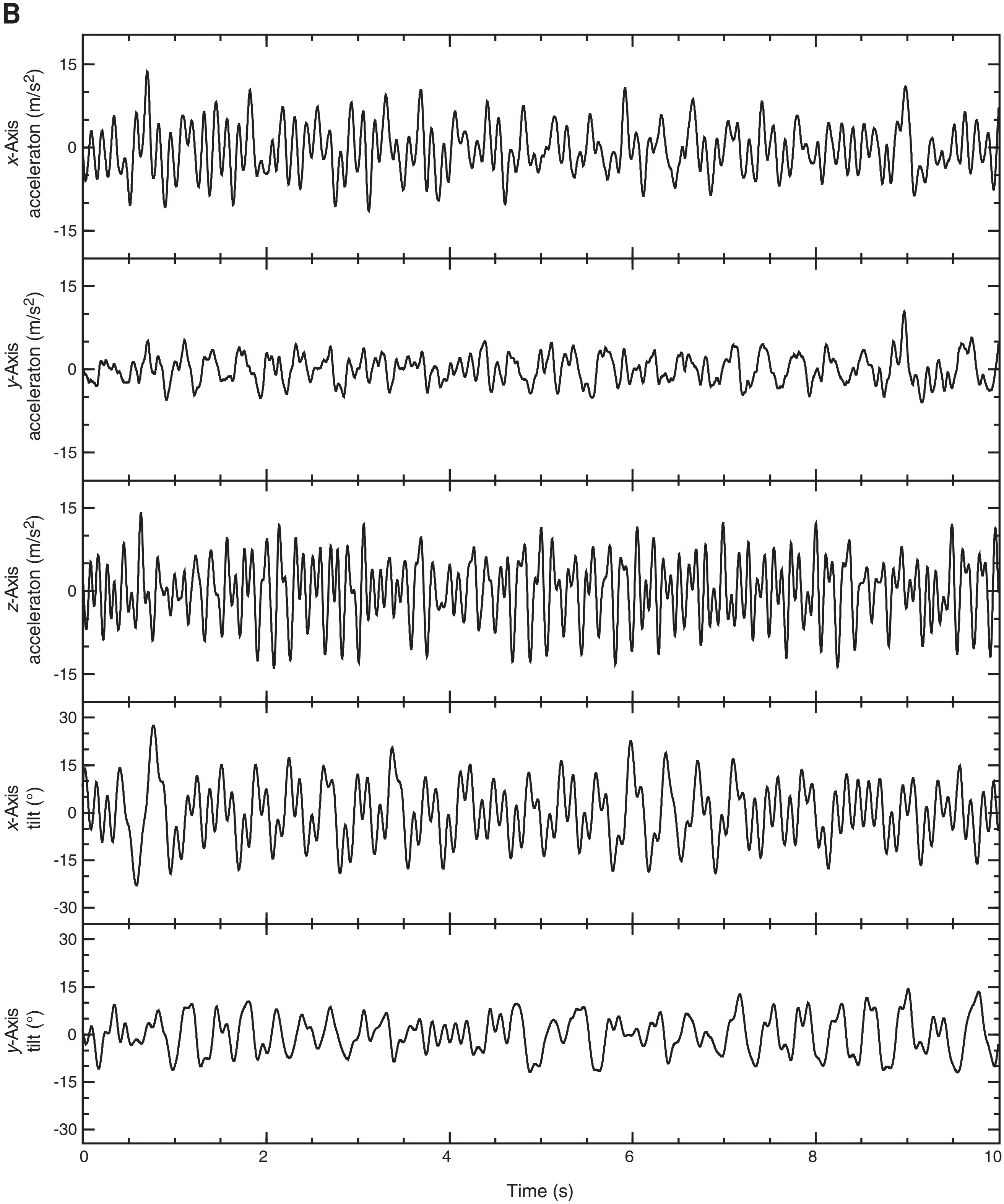

Figure F42. Power spectral density from the three components of acceleration data. **A.** First dummy run. (**Continued on next page.**)

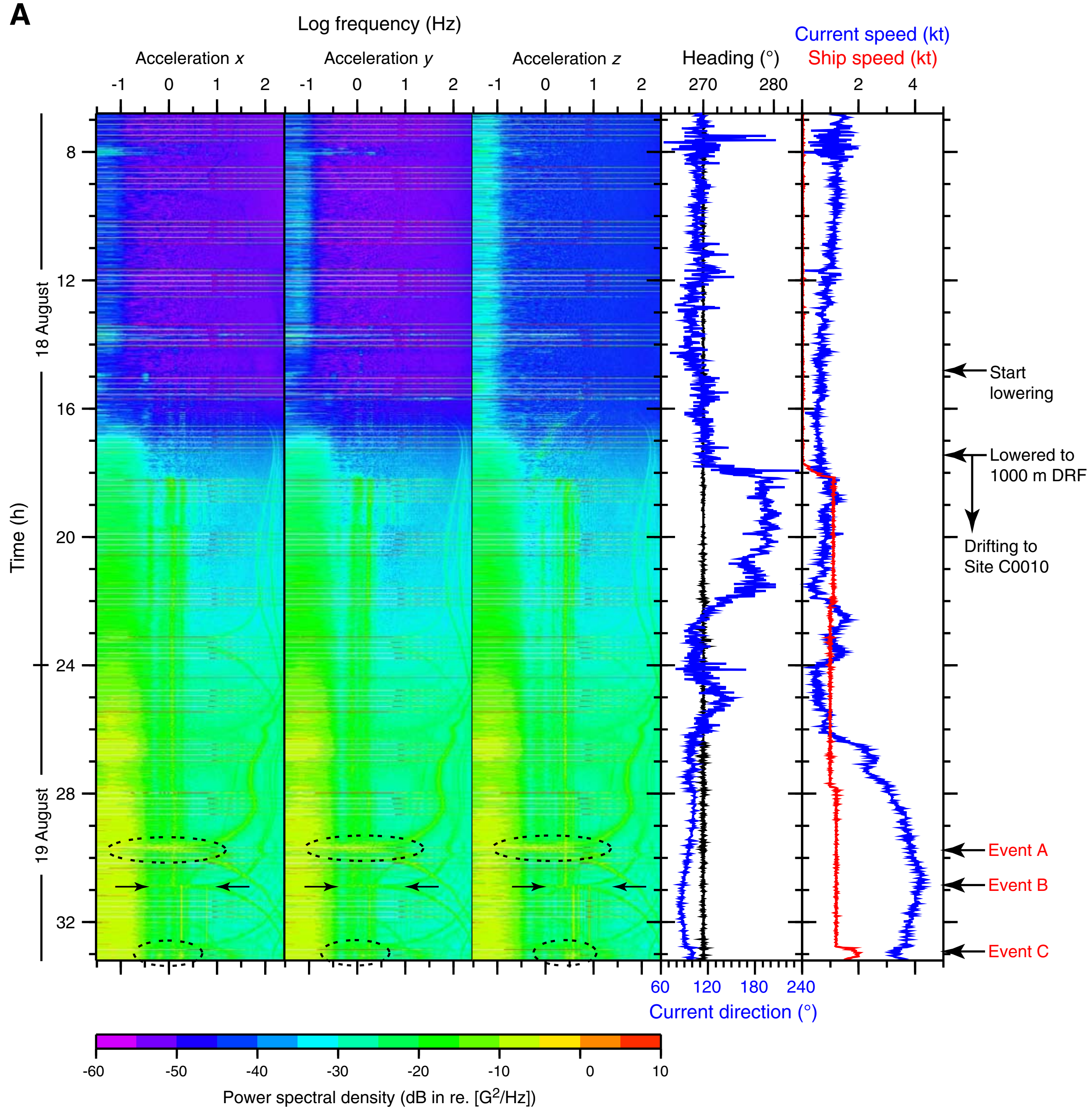

Figure F42 (continued). B. Second dummy run. Vertical and horizontal axes show time (hours) and logarithmic frequency (Hz). Power spectral density is shown in dB in relation to G²/Hz. Events A, B, and C are noted. Ship heading and current speed are shown on the right.

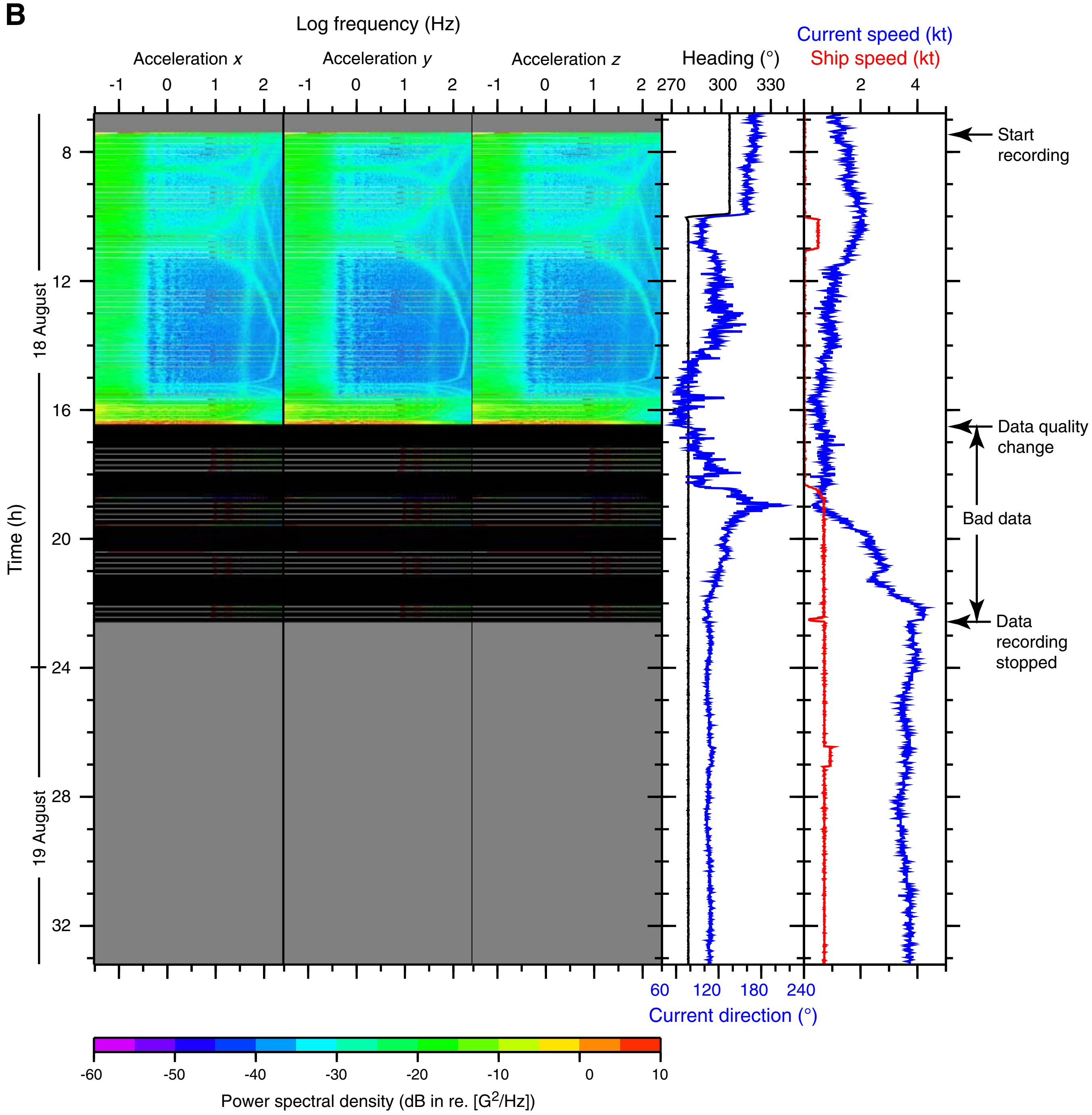

Figure F43. Ship tracks during dummy run test. Red = first dummy run track, blue = second dummy run track. Events A, B, and C from Figure F42A shown.

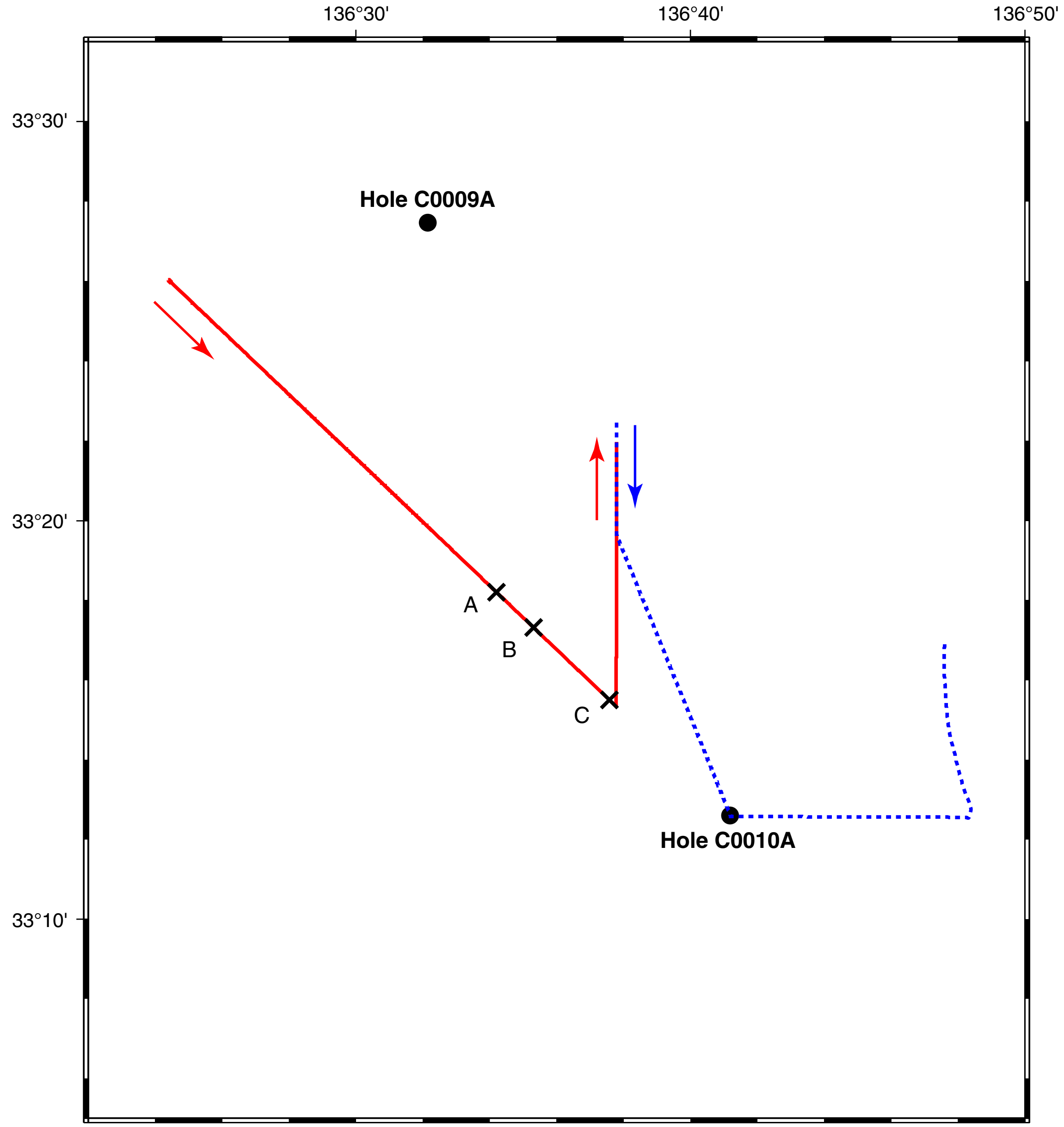

Figure F44. A. Temperature data from first dummy run. **B.** Detail of temperature data for 19 August 2009. Location of each miniature temperature logger (MTL) noted in A.

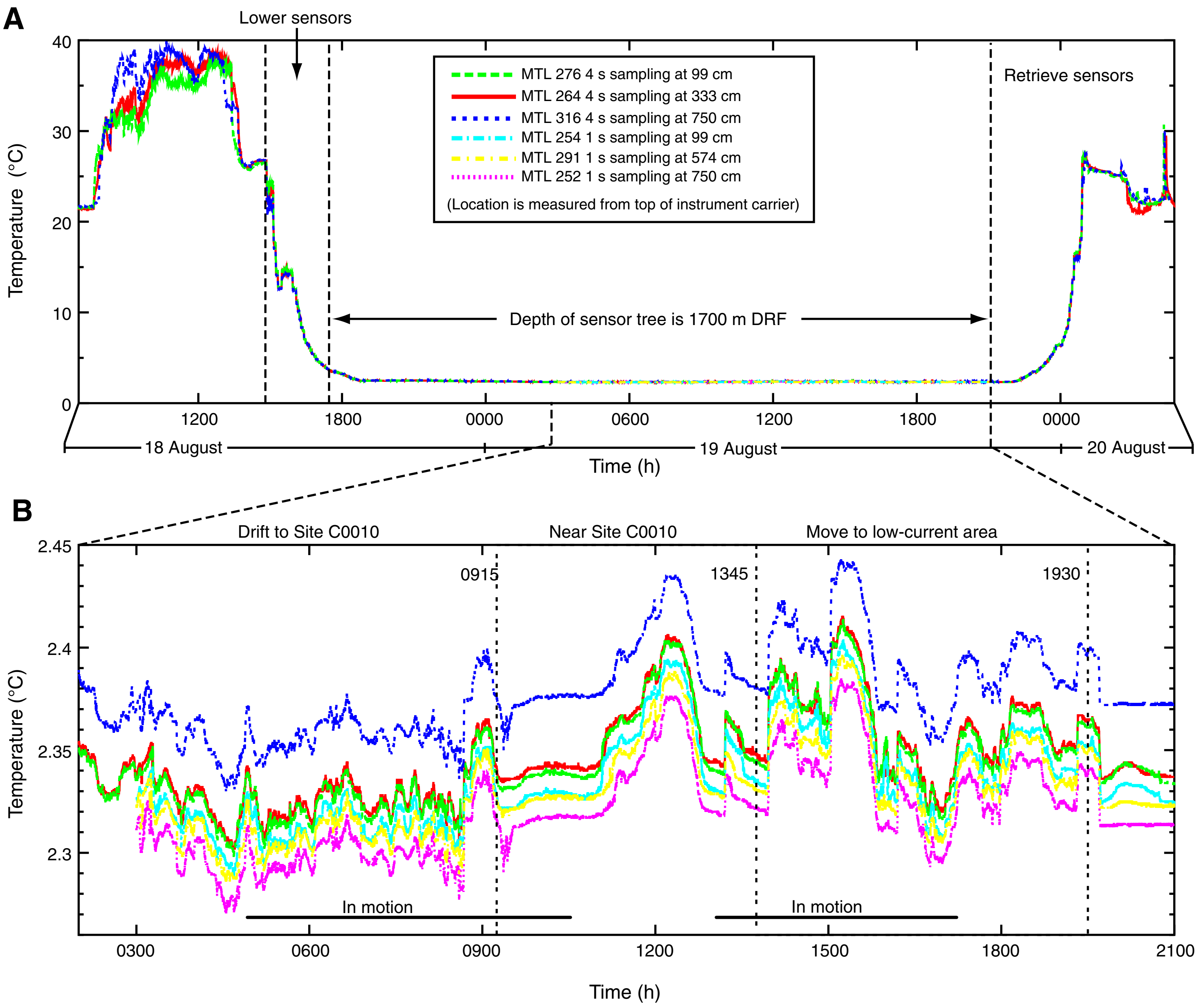

Figure F45. A. Photograph of bullnose (i.e., lower end cap of smart plug) showing termination of pore pressure tubing (center) for monitoring screened splay fault zone. **B.** Photograph of instrument on rig floor during final preparation using threadlock to secure bolts.

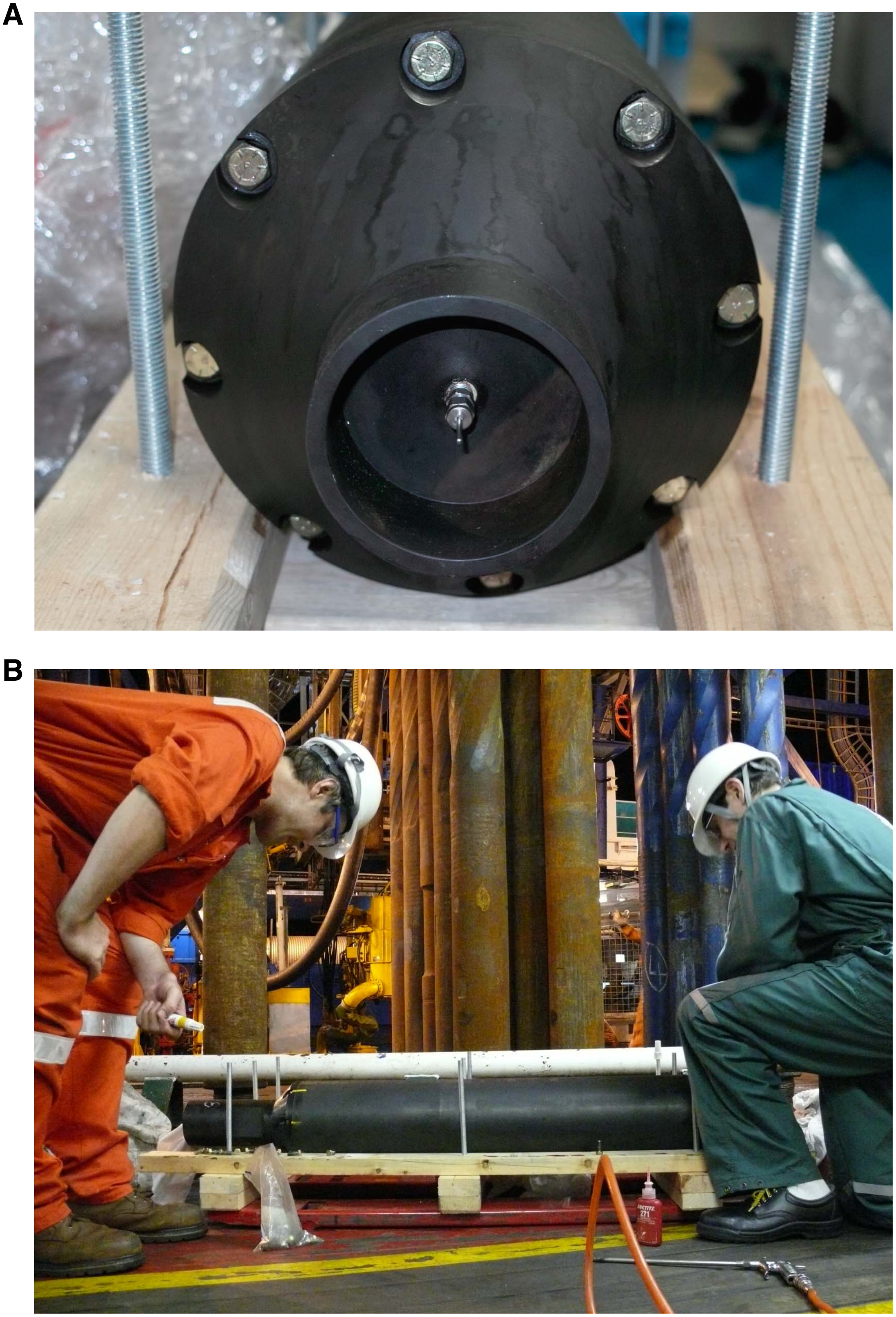

Figure F46. Schematic diagram of smart plug (instrumented bridge plug) installation at Site C0010, including geometry and depth of casing, screened interval, and bridge plug assembly. Drawing is not to scale.

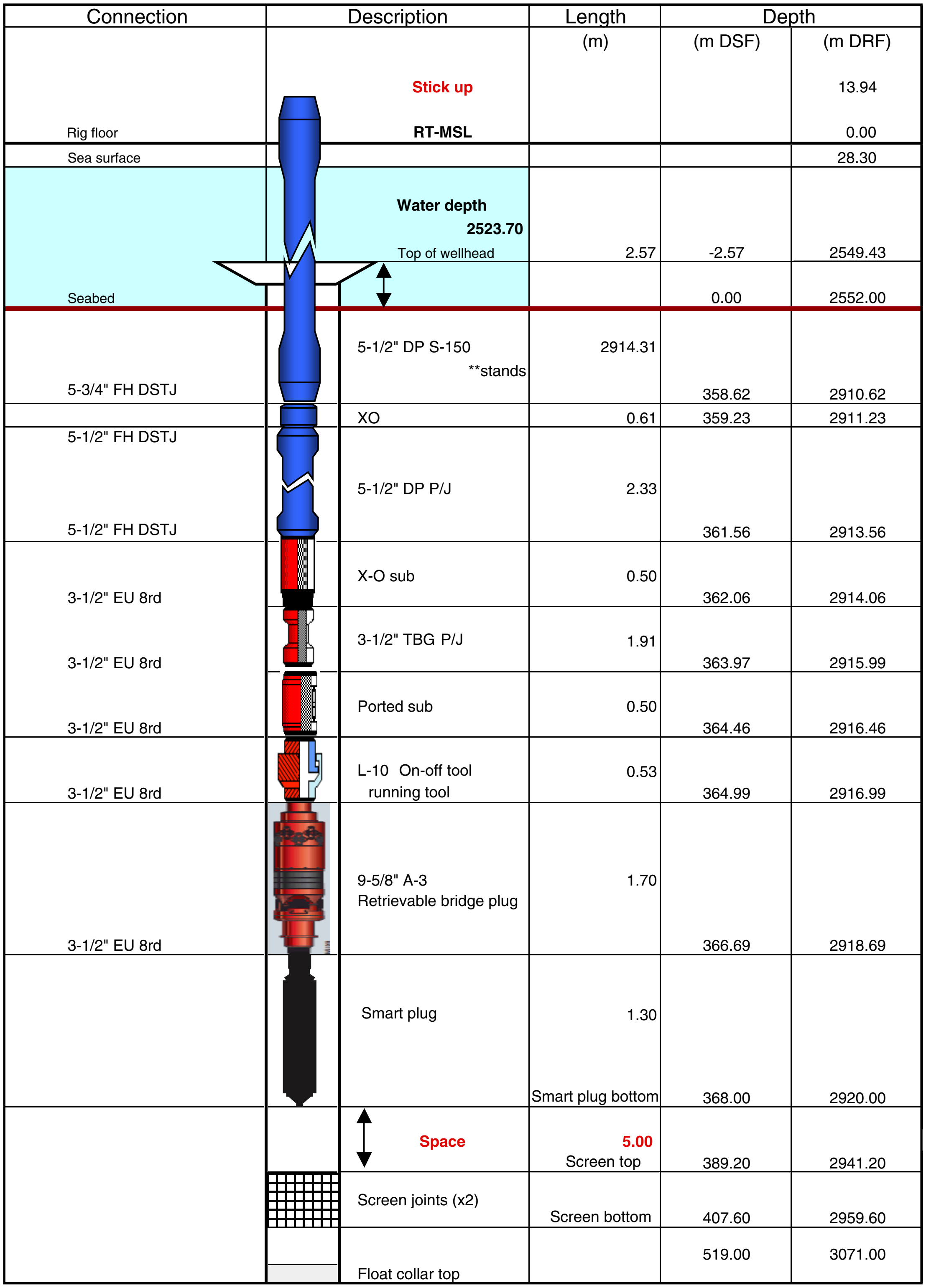

Connection	Description	Length	Depth	
		(m)	(m DSF)	(m DRF)
	Stick up			13.94
Rig floor	RT-MSL			0.00
Sea surface				28.30
	Water depth 2523.70 Top of wellhead	2.57	-2.57	2549.43
Seabed			0.00	2552.00
5-3/4" FH DSTJ	5-1/2" DP S-150 **stands	2914.31	358.62	2910.62
	XO	0.61	359.23	2911.23
5-1/2" FH DSTJ 5-1/2" FH DSTJ	5-1/2" DP P/J	2.33	361.56	2913.56
3-1/2" EU 8rd	X-O sub	0.50	362.06	2914.06
3-1/2" EU 8rd	3-1/2" TBG P/J	1.91	363.97	2915.99
3-1/2" EU 8rd	Ported sub	0.50	364.46	2916.46
3-1/2" EU 8rd	L-10 On-off tool running tool	0.53	364.99	2916.99
3-1/2" EU 8rd	9-5/8" A-3 Retrievable bridge plug	1.70	366.69	2918.69
	Smart plug	1.30 Smart plug bottom	368.00	2920.00
	Space	5.00 Screen top	389.20	2941.20
	Screen joints (x2)	Screen bottom	407.60	2959.60
	Float collar top		519.00	3071.00

Figure F47. Photograph of smart plug instrument connection (**A**) during and (**B**) after tack-welding it to bridge plug to prevent unscrewing during deployment in strong ocean current.

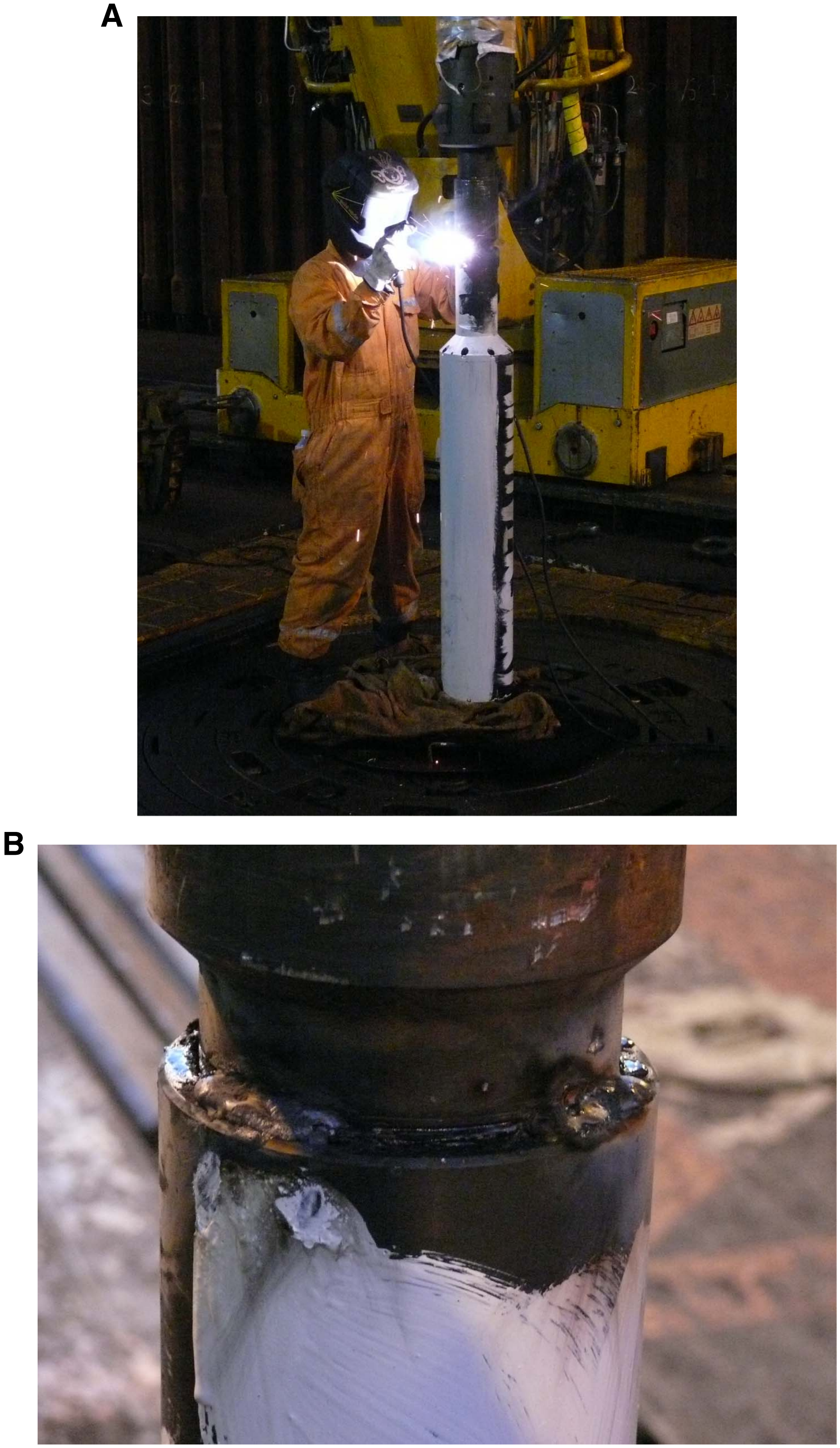

Figure F48. Photograph of assembled smart plug instrument (below, marked with white paint) and bridge plug (above) immediately before installation on 22 August 2009, 0518 h Japan Standard Time (JST).

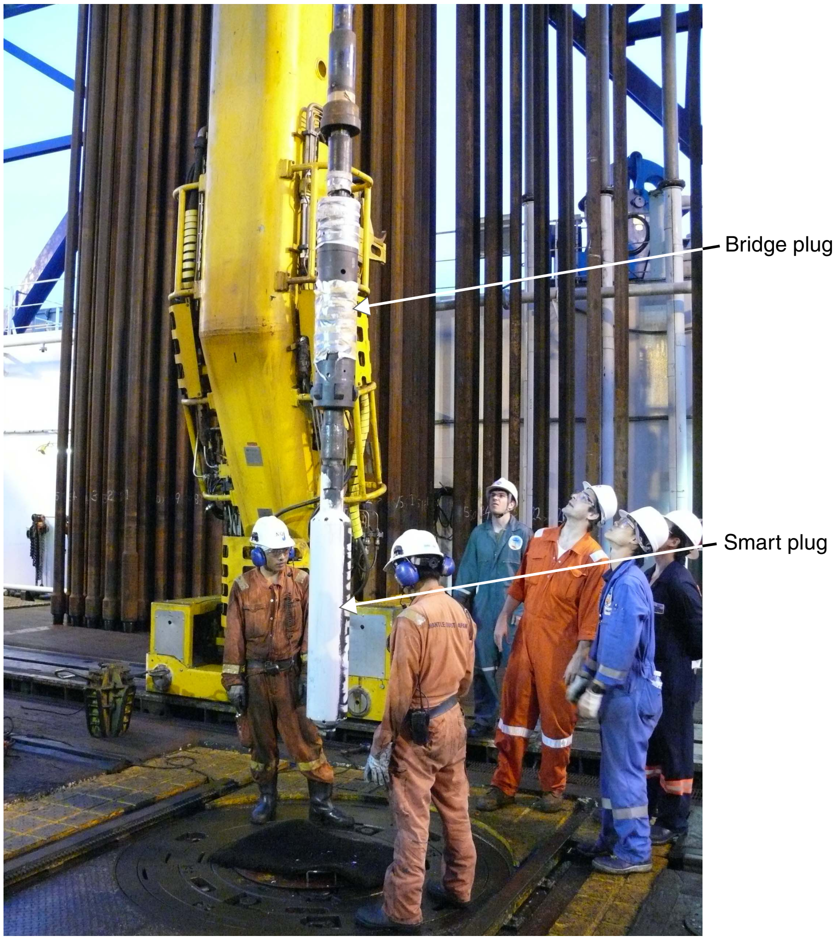

Table T1. Operations summary, Site C0010. (See table notes.)

Hole C0010A
Latitude: 33°12.5981′N
Longitude: 136°41.1924′E
Water depth (m): 2523.7
Seafloor (m): 2552 DRF/2523.7 MSL
20 inch conductor pipe shoe (m): 2593 DRF (41 DSF)
TD (m): 3107 LRF (555 LSF)
Run 1 (m): 2593–3034 DRF/LRF
Run 2 (m): 3034–3107 DRF/LRF (2900–2970 m repeat section)

	Start		Depth LSF (m)		
Operation	Date (Aug 2009)	Local time (h)	Top	Bottom	Comments
Hole C0010A			0	560	
Tool prep, rig up and RIH	3	2359			Set up and run 20 inch casing; jump ROV
ROV survey	5	0100			Arrive at Site C0010
Run into hole to seabed	5	0745			ROV recovered to surface for maintenance
Tag seafloor	5	0659			Install guidehorn
Jet-in casing	5	0745			Jet in 20 inch casing to 41 mbsf
Make up 12-1/4 inch BHA	6	0659			Run BHA and drift to Site C0010
BHA run into hole, drifting	6	2030			
ROV fixed on BHA, lower into well	7	1230			
Drilling LWD starts	7	1315			Start LWD drilling
Ream down and sweep with Hi-vis mud	9	0145			Sweep and displace mud
POOH in preparation to avoid weather	9	1215			Typhoon “Elum” approaching Site C0010
Move vessel to safe area	9	2230			
Wait on typhoon to pass	10	2359			
Sail back to Site C0010	11	2359			Make up casing hanger running tool, pup joint, and hanger joint
Program LWD tools on deck, RIH	11	0900			Run tools in hole while drifting to Site C0010
Stab BHA into wellhead	12	0200			Continue running into hole
Drill 12-1/4 inch hole to TD, wiper trip	12	1045			
POOH and prepare 9-5/8 inch casing	13	1945			
Drift and run 9-5/8 inch casing	14	0915			
RIH with 9-5/8 inch casing, cementing	15	0430			Mix and pump cement slurry
POOH and move to low current area	16	0745			ROV experiences broken strand on umbilical
RIH and scrape 9-5/8 inch casing	17	1445			After scraping, POOH and move to low current area
Prepare first dummy run carrier for RIH	18	1215			
RIH dummy carrier and drift	18	1745			
Suspend drifting due to high current	19	0915			
ROV inspection of dummy carrier	19	1930			Damage found to carrier from VIV from Kuroshio Current; strainmeter and tubing torn off bottom flange, and one seismometer missing from carrier
POOH and reconfigure dummy carrier	20	0115			Add dummy strainmeter, and remove seismometer; accelerometer reset and attached to carrier
Preparation for 2nd dummy run, RIH	20	0700			
Drift to Site C0010, stab in hole	21	1015			Stab 3 times into wellhead, and POOH
POOH and move to low current area	21	1600			
Make up A3 retrievable casing packer and smart plug	22	0430			
RIH smart plug and drift to Site C0010	22	0600			
Set casing packer and smart plug	22	0600			
POOH and perform ROV maintenance	23	0600			
Big head transducer calibration	23	0600			
Set corrosion cap and recover beacons	24	0600			

Notes: MSL = mud depth below sea level, DRF = drillers depth below rig floor, DSF = drillers depth below seafloor, LRF = logging-while-drilling (LWD) depth below rig floor, LSF = LWD depth below seafloor, mbsf = meters below seafloor. TD = total depth. RIH = run in hole, POOH = pull out of hole. ROV = remotely operated vehicle. BHA = bottom-hole assembly. VIV = vortex-induced vibration.

Table T2. Bottom-hole assembly, Hole C0010A. (**See table note.**)

BHA component	Length (m)	Cumulative length (m)
12-1/4 inch bit	0.28	0.28
RAB-8 (solid float/12-1/8 slv)	3.78	4.06
TeleScope 825 HF	8.50	12.56
12-1/4 inch stabilizer	2.34	14.90
8 inch nonmagnetic drill collar	9.13	24.03
8-1/2 inch drilling collar	9.30	33.33
8-1/2 inch drilling collar	9.30	42.63
8-1/2 inch drilling collar	9.30	51.93
8-1/2 inch drilling collar	9.30	61.23
8-1/2 inch drilling collar	9.30	70.53
8-1/2 inch drilling collar	9.30	79.83
Mechanical jar	10.70	90.53
8-1/2 inch drilling collar	9.30	99.83
8-1/2 inch drilling collar	9.30	109.13
8-1/2 inch drilling collar	9.30	118.43
8-1/2 inch drilling collar	9.30	127.73
8-1/2 inch drilling collar	9.30	137.03
Crossover sub	1.00	138.03
5-7/8 inch 26.40 drill pipe steel	10.00	148.03

Note: BHA = bottom-hole assembly.

Table T3. Calibrated check shot time-depth relationship, Sites C0004 and C0010 applying C0004 check shot data. (See table notes.)

Depth LSF (m)	Original first arrival time (ms)	Calibrated first arrival time (ms)	
		Site C0004	Site C0010
–0.01	1761.9	1766.2	1696.9
17.54	1773.9	1778.2	1708.9
32.24	1782.5	1786.8	1717.5
55.76	1798.4	1802.7	1733.4
70.36	1807.2	1811.5	1742.2
93.95	1820.9	1825.2	1755.9
108.58	1829.3	1833.6	1764.3
132.20	1842.8	1847.1	1777.8
146.77	1850.8	1855.1	1785.8
170.36	1864.7	1869.0	1799.7
184.96	1871.1	1875.4	1806.1
208.58	1885.2	1889.5	1820.2
223.31	1892.3	1896.6	1827.3
246.80	1905.5	1909.8	1840.5
261.44	1912.0	1916.3	1847.0
285.06	1924.7	1929.0	1859.7
299.69	1931.6	1935.9	1866.6
337.95	1951.5	1955.8	1886.5
361.57	1963.7	1968.0	1898.7
371.08	1969.0	1973.3	1904.0
376.46	1970.9	1975.2	1905.9

Notes: Original first arrival picks are associated with depth of observations (Site C0004). Calibrated first arrival times are calibrated at seafloor.

Table T4. Calibrated check shot time-depth relationship, Site C0003. (See table notes.)

Depth LSF (m)	Original first arrival time (ms)	Calibrated first arrival time (ms)
86.10	1694.5	1695.7
124.30	1716.5	1717.7
200.70	1756.5	1757.7
238.90	1774.5	1775.7
277.20	1792.5	1793.7
353.60	1830.5	1831.7
391.80	1848.5	1849.7
430.00	1864.5	1865.7
468.20	1882.5	1883.7
506.50	1900.5	1901.7

Notes: Original first arrival picks are associated with depth of observations. Calibrated first arrival times are calibrated at seafloor.